Supplementary Materials for

Separation of Hexane Isomers in a Metal-Organic Framework with Triangular Channels

Zoey R. Herm, Brian M. Wiers, Jarad A. Mason, Jasper M. van Baten, Matthew R. Hudson, Pawel Zajdel, Craig M. Brown, Norberto Masciocchi, Rajamani Krishna,* Jeffrey R. Long*

*Corresponding author. E-mail: r.krishna@uva.nl (R.K.); jrlong@berkeley.edu (J.R.L.)

Published 24 May 2013, *Science* **340**, 960 (2013)
DOI: 10.1126/science.1234071

This PDF file includes:

Other Supplementary Material for this manuscript includes the following:
available at www.sciencemag.org/cgi/content/full/340/6135/960/DC1

Movie S1

Supplementary Materials

Materials and Methods:

Supplementary Text:

Materials and Methods

Identification of commercial equipment in the text is not intended to imply any recommendation or endorsement by the National Institute of Standards and Technology.

1.1 Synthesis of $Fe_2(BDP)_3$

H_2BDP was synthesized according to the literature (*28*). A 100 ml Schlenk flask was charged with 6.04 g (17.1 mmol) of $Fe(acac)_3$, 1.20 g (5.71 mmol) of H_2BDP and a magnetic stir bar. 80 mL of dry, degassed N,N-dimethylformamide (DMF) was added to the Schlenk flask via cannula transfer. The reaction was refluxed under nitrogen for 18 hours. The black microcrystalline precipitate was collected on a Buchner funnel. This material was heated in dimethyl sulfoxide (DMSO) at 100 °C for 8 hours, and the DMSO was decanted. The material was then washed 5 more times with heated DMSO and similarly six more times with DMF heated to 100 °C and six more times with methylene chloride heated to 70 °C. This washing procedure removes unreacted ligands, metal sources, polymerization products of DMF and solvents from previous washes. The material is then heated under 10 mTorr vacuum to 180 °C for 24 hours to remove guest solvent molecules. FT-IR: (solid, ATR): $\nu_{C=C}$ 1576, $\nu_{C=N}$ 1384, 1342 cm^{-1}. An aliquot of the activated sample was then soaked in DMSO, filtered, dried in air and then examined by TGA and CHN analysis. The 16% weight-loss observed at 150 °C was consistent with a formulation of $Fe_2(BDP)_3$•1.75DMSO which was in agreement with CHN analysis. Anal. Calcd. for $Fe_8C_{158}H_{138}N_{48}S_7O_7$: C, 54.23; H, 4.18; N, 19.21. Found: C, 54.73; H, 3.82; N, 18.73.

1.2 Low pressure gas adsorption measurements

For all gas adsorption measurements 200-225 mg of $Fe_2(BDP)_3$•1.75 DMSO was transferred to a pre-weighed glass sample tube under an atmosphere of nitrogen and capped with a Transeal. Samples were then transferred to Micromeritics ASAP 2020 gas adsorption analyzer and heated at a rate of 1 °C /min from room temperature to a final temperature of 180 °C. Samples were considered activated when the outgas rate at 150 °C was less than 2 μbar/min, which occurred

near 48 hours after the start of evacuation. Evacuated tubes containing degassed samples were then transferred to a balance and weighed to determine the mass of sample, typically 150-175 mg. The tube was transferred to the analysis port of the instrument where the outgas rate was again determined to be less than 2 μbar/min at 180 °C. 99.999% purity gas was used for nitrogen adsorption (Figures S8 and S9). All non-cryogenic measurements were performed using sand bath connected to an automated temperature controller. Liquid hexane isomers were obtained from Sigma Aldrich and were added to the ASAP 2020 vapor adsorption apparatus. The liquids were frozen. The pressure was monitored until it reached a low of 0.001 mbar, and then the headspace was evacuated for 5 minutes. The solid was melted, and the freeze-pump thaw procedure was repeated two more times. The liquid was then distilled into a new sample tube three times, each time only collecting approximately 50 % of the original volume.

1.3 Breakthrough measurements

A column of 0.491 g of $Fe_2(BDP)_3$ was packed into a glass u-tube, with an internal diameter of 0.9525 cm. The height of the sample was 11.5 cm. Dry N_2 at a rate of 2.5 mL/min was bubbled through a mixture of hexane isomers according to the following volumes: 2.67 mL of 2,2-dimethylbutane, 3.50 mL of 2,3-dimethylbutane, 3.79 mL of 2-methylpentane, 4.22 mL of 3-methylpentane, and 5.82 mL of *n*-hexane. These volumes were determined through trial and error: The experiment was run without any sample and the vapor phase ratios were optimized to an equimolar final product. The effluent was passed through a VICI Valco 6-way sampling valve. Every minute, a 0.25 mL aliquot of gas was delivered to a Perkin Elmer Clarus 500 gas chromatograph fitted with a Supelco Equity-1 capillary GC column, 15 m long, with a 0.1 mm outside diameter and 0.10 μm poly(dimethyl sulfoxane) coating, submerged in an ice water bath. All five peaks were separated and easily integrated in the resulting GC trace.

1.4 Powder X-ray diffraction methodology

1.4.1 Powder X-ray diffraction structure solution of $Fe_2(BDP)_3$

Microcrystalline samples of solvated $Fe_2(BDP)_3$ were gently ground and deposited in an aluminum sample holder equipped with a zero-background plate. Diffraction data was collected by means of an overnight scan in the 2θ range of 5–105° with 0.02° steps using a Bruker AXS D8 Advance diffractometer equipped with Ni-filtered Cu- α radiation (λ = 1.5418 Å), a Lynxeye linear position-sensitive detector, and mounting the following optics: primary beam Soller slits (2.3°), fixed divergence slit (0.3°), receiving slit (8 mm). The nominal resolution for the set-up is 0.08° of 2θ (FWHM of the α_1 component) for the LaB_6 peak at about 2θ = 21.3°. The generator was set at 40 kV and 40 mA. In order to get higher resolution data, a powder pattern was also collected on a powder diffractometer of the Institute of Crystallography of the Italian CNR in Bari, that is equipped with a primary beam Ge(111) monochromator, Cu-Kα radiation in Debye-Scherrer geometry (glass capillary diameter: 0.5 mm), and an INEL CPS-120 position sensitive detector covering a 120° 2θ range. (The courtesy of Giuseppe Chita, IC-CNR, is acknowledged for technical assistance).

A standard peak search, followed by indexing through the Single Value Decomposition approach (*40*), as implemented in TOPAS-Academic (*41*), allowed the determination of approximate unit cell parameters. The space group was assigned as *Fddd* on the basis of systematic absences. The unit cell and space group were checked by a Le Bail refinement and confirmed by successful structure solution and Rietveld refinement. The structure solution of

$Fe_2(BDP)_3$ was performed using the simulated annealing technique, as implemented in TOPAS. Initially, a rigid, idealized model was employed for the crystallographically independent portions of the BDP^{2-} moiety (one full and one half ligands). To build the rigid model describing BDP^{2-}, the following bond distances and angles have been adopted: a) for the benzene ring: C–C = 1.39 Å; C–H = 0.95 Å; C–C–C, C–C–H = 120°; b) C–C, C–N, N–N = 1.36 Å; C–H = 0.95 Å; internal ring angles = 108°; C–C–H = 126°; $C_{benzene}$–$C_{pyrazole}$ = 1.45 Å. After the initial structure solution, the arene-pyrazole torsion angle was allowed to refine. Residual electron density in the channels was modeled as a disordered dimethylformamide (DMF) solvent molecule. The final refinement was performed using the Rietveld method, maintaining the rigid bodies introduced at the structure solution stage. The background was modeled by a polynomial function of the Chebyshev type. Peaks shapes were described by the Fundamental Parameters Approach (*42*). Anisotropic peak broadening was modeled using spherical harmonics to define the peak widths. A single refined isotropic thermal parameter was assigned to the Fe atom, and this was augmented by 2.0 $Å^2$ for the atoms of the BDP^{2-} ligand and by 4.0 $Å^2$ for the atoms of the DMF molecule. Note that in the final Rietveld refinements, both collected X-ray diffraction patterns were used as independent observations of different information content and were employed simultaneously during model refinement. The final Rietveld plots are shown in Figures S10 and S11.

Crystal data for $Fe_2(BDP)_3$ at 298 K: $Fe_2(C_{12}N_4H_8)_3(C_3H_7NO)_{0.5}$; orthorhombic, *Fddd*, a = 7.1046(2), b = 26.4943(5), c = 45.3489(9) Å, V = 8536.1(4) $Å^3$, R_{wp} = 0.026; R_p = 0.017; R_{Bragg} = 0.012. Metrical data for the solid-state structure of $Fe_2(BDP)_3$ is available free of charge from the Cambridge Crystallographic Data Centre under reference number CCDC 915106.

The solvent accessible area was calculated using Platon crystallographic software (*43*) with 0.2A grid spacing 1.2 Å probe size. The atomic van der Waals radii were C 1.70 Å, H 1.20 Å, Fe 2.14 Å, N 1.55 Å. The calculated packing index (Calc K.P.I) was 49.5% (*44*) and the total Potential Solvent Area 3275.2 $Å^3$ per 8535.3^3 Unit Cell Volume (38.4%).

1.4.2 Variable temperature powder X-ray diffraction of $Fe_2(BDP)_3$

Variable temperature powder X-ray diffraction experiments were performed on $Fe_2(BDP)_3$ using the D8 Advance diffractometer described above. The experiments were carried out in air using a custom-made sample heater, assembled by Officina Elettrotecnica di Tenno, Ponte Arche, Italy. Microcrystalline samples of solvated Fe_2BDP_3 were gently ground and deposited in an aluminum sample holder. Powder diffraction patterns were recorded in the 2θ range of 7–26°, heating *in situ* from 30 to 410 °C in 20 °C increments. Parametric treatment (using the Le Bail method) of the data acquired before loss of crystallinity gave the unit cell parameters as a function of temperature (Figures S12 and S13).

1.5 Fitting of pure component isotherms from experiments and IAST calculations

The pure component isotherm data for adsorption of *n*-hexane (nC6), 2-methylpentane (2MP), 3-methylpentane (3MP), 2,2-dimethylbutane (22DMB) and 2,3-dimethylbutane (23DMB) in $Fe_2(BDP)_3$ were experimentally determined for different temperatures. As illustration, Figure S14 presents the data on pure component isotherms for nC6, 2MP, 3MP, 22DMB, and 23DMB in $Fe_2(BDP)_3$ at a temperature of 433 K and their associated fitting curves.

The *absolute* loadings, were fitted with the dual-Langmuir-Freundlich isotherm model

$$q = q_{A,sat}\frac{b_A p^{\nu_A}}{1+b_A p^{\nu_A}} + q_{B,sat}\frac{b_B p^{\nu_B}}{1+b_B p^{\nu_B}} \quad (1)$$

with T-dependent parameters b_A, and b_B

$$b_A = b_{A0}\exp\left(\frac{E_A}{RT}\right); \quad b_B = b_{B0}\exp\left(\frac{E_B}{RT}\right) \quad (2)$$

The parameter sets are provided in Table S2.

The 5-component mixture adsorption equilibrium was determined using the Ideal Adsorbed Solution Theory (IAST) of Myers and Prausnitz (*45*). Figures S15A, B, and C show the IAST calculations for temperatures of 403 K, 433 K, and 473 K. At any specified pressure, the hierarchy of component loadings is nC6 > 2MP ≈ 3MP > 22DMB ≈ 23DMB, indicating the possibility of separation of the hexanes isomers into three fractions depending on the degree of branching.

In Figures S15D, E and F, we plot the "normalized" molar loadings: (nC6), (2MP+3MP)/2, and (22DMB+23DMB)/2 against the pressure for all three temperatures 403 K, 433 K, and 473 K. We note that $Fe_2(BDP)_3$ has the remarkable ability to separate the hexane isomer mixtures into three fractions for the entire temperature range 403 K to 473 K that is of relevance in industry. Furthermore, it is also evident that this ability to "fractionate" the feed mixture into three different fractions is valid over the entire range of pressures. This implies that the fractionation ability is independent of feed mixture composition. Below we use pulse chromatographic simulations, including diffusion, to confirm that diffusional effects do not erode the fractionation ability.

1.5 Isosteric heat of adsorption calculations

The isosteric heat of adsorption, Q_{st}, defined as

$$Q_{st} = RT^2\left(\frac{\partial \ln p}{\partial T}\right)_q \quad (3)$$

were determined using the pure component isotherm fits. The dual-site Langmuir-Freundlich isotherm fits were differentiated with the Clausius-Clapeyron equation.

1.7 Packed bed adsorber breakthrough simulation methodology

The breakthrough simulation methodologies, for step- and pulse- inputs, are described in detail in earlier works (*37,46*).

1.8 Neutron diffraction and corresponding computational efforts

1.8.1 Summary

Data was collected on 0.9986 g bare sample at 10 K on the neutron powder diffractometer BT1 using a Ge(311) monochromator with 60' collimation. The activated sample was then transferred to a He-glove box and dosed with approximately 50 μL/g (d14)-*n*-hexane, sealed in a vanadium sample can, and heated to around 90 °C for 12 hours. After collecting data on this sample, the sample was activated at approximately 180 °C for 24 hours and dosed with just over 100 μL/g

(d14)-*n*-hexane, heated again to around 90 °C for 12 hours, and the final (saturation) data set collected (Figure S16).

From the calculations and the comparison with the neutron diffraction data, we can determine that the adsorption of *n*-hexane is linear down the *a*-axis of the unit cell in the triangular pore, requiring a cell of 2x1x1 to account for the full *n*-hexane molecule, and the *n*-hexane is disordered, centered between the three ligands making the *a*-axis channels (Figure S17). Attempts to refine and model this disorder were thoroughly exhausted using several different refinement programs and parameters. However, within the confines of the available data, no exact positions could be determined. The fact that there are no superlattice reflections indicated that there is unlikely any correlation between the positions of hexanes adsorbed in each pore, and then there is no registration along the pore itself, making every atom position as likely to contain a CD_2 as a terminal CD_3 (but weighted 4:2 for the *n*-hexane molecule) and at least 3-fold disordered.

1.8.2 Grid-based projector-augmented wave method (GPAW) calculations of energies of possible *n*-hexane sites

Calculations were carried out using GPAW code version 0.9.0.8965 (*47*). The initial setup was based on the empty framework (Figure S18A) provided in cif file fe2bdp3-minusb.cif. The structure in orthorhombic spacegroup *Fddd* with lattice parameters a = 7.1043Å, b = 26.4906Å, c = 45.3533Å contained 20 unique atomic positions.

For the calculations the symmetry would have to be lowered to P1, which would result in 592 framework atoms. Additionally, in order to fully insert *n*-hexane into a pore with enough free space at the ends (without self-overlap), the cell would have to be at least doubled along a, which made the calculations impossible in the orthorhombic cell. Tripling of the cell was excluded as it reached over 50GB RAM limit. Therefore, an equivalent Niggli triclinic cell was chosen for further study (Figure S18B) with lattice parameters a = 7.1043 Å, b = 13.7133 Å, c = 22.9532 Å, α = 87.703 °, β = 81.097 °, γ=74.988 °, space group *P*-1 and 25% of the original volume. Although it contained 74 unique atoms in *P*-1 but only 148 in *P*1, much less compared to 592 in the orthorhombic cell.

1.8.2.1 Not relaxed Niggli cell LDA vs. vdW-DF

At first the energy of the system was calculated with Local Density Approximation (LDA) as the exchange-correlation potential, using 1 k-point (0,0,0) and at T=0 K. There were two arguments behind the choice of only 1 k-point: a) it was impossible to add more points in the final calculations with inserted *n*-hexane and the reference energy had to be obtained using the same setup, b) highly molecular character of the system results in almost no dispersion, hence Γ-point is a good approximation of the whole band structure.

The GPAW run GPAW(h=0.2, xc='LDA', mixer=Mixer(0.02, 3, 10) converged after 74 iterations with 38 seconds per iteration and free energy of –1117.38 eV. Next a van der Waals potential (xc='vdW-DF') was tested (*48*) using the same calculator parameters. The free energy after 66 iterations was -1581.82 eV.

1.8.2.2 Relaxation of the Niggli cell

The calculations revealed large forces >8eV/Å present on the atoms requiring relaxation of the structure, which was performed using QuasiNewton optimizer built-in GPAW. The first 7 cycles

decreased the free energy down to -1607.90 eV and then they started to oscillate.

The reason for bad convergence was parameter WFS (Wannier Functions), which was hovering around −0.3. To remedy this, the number of bands was increased from the default value of 468 to 500. The further relaxation was stopped after 39 cycles, when forces dropped below 0.5 eV/Å. The energy decreased from -1607.90 to -1609.77 eV. More exact relaxation was not necessary because the insertion of *n*-hexane would change the force balance anyhow.

1.8.2.3 Energy and structure of *n*-hexane

The starting *n*-hexane model was built from atoms in roughly correct positions, which were later on minimized with QuasiNewton minimizer until the forces were smaller than 0.05 eV/Å. The first run with LDA approximation ended with free energy -111.78 eV (Figure S19A).

Next, the xc potential was changed to vdW-DF (free energy 136.05 eV), which raised forced present on the atoms, so the structure was relaxed again (136.14 eV). The structure is presented in Figure S19B.

The main differences between the structures are in the carbon-carbon distances which increased from 1.504 to 1.536 Å. The model from Figure S19B was used for insertion into the framework. As the last step, the energy of the *n*-hexane alone was recalculated using the same convergence criteria as for the final calculations. The obtained free energy was −136.68 eV, which was used as a reference value.

1.8.2.4 Parameters for the insertion of *n*-hexane

The *n*-hexane optimized earlier was 6.5 Å long end to end, so it would not fit into the single unit cell of the framework. That is why the Niggli cell was extended to 2x1x1 superstructure with 296 atoms. It roughly leaves 2 Å on each side of *n*-hexane with periodic boundary conditions. The initial run of the empty doubled framework did not converge due to oscillations. The memory usage was around 7GB with 3.5 minutes per iterations in dual computer (8 cores) setup. At first, to remedy the oscillations, the default number of bands was increased from 936 to 1100 in order keep the same setup after inserting hexane (+38 bands). It is equivalent to the Niggli case (2*500bands) plus some additional freedom due to larger cell.

It has to be stressed that despite the small oscillations in residual density $<10^{-3}$ the energy and Wannier Functions of the system were stable (Figure S20). But in order to compensate for the large volume of the system convergence criteria were relaxed and introduced to the calculator as *convergence = { 'energy': 0.0005, 'density': 1.0e-3, 'eigenstates': 1.0e-6}*. Also different Mixer parameters were tested and, except the mixing parameter 0.02, found to have negligible influence. The final one selected for calculations were *Mixer(0.02, 3, 5)*.

A faster Gauss-Seidel solver was chosen with precision decreased from 10^{-10} to 10^{-8}, which is still above the required minimum 10^{-6} *poissonsolver=PoissonSolver (relax='GS', eps=1e-8)*. Finally, the real space grid was modified to be divisible by 8 in each direction to 68x68x112, which gave spacings between grid points smaller than 0.21Å. With these settings a complete calculation took roughly 7h and 90 iterations. The calculation of empty 2x1x1 framework converged after 72. The energy was −3219.61 eV, which is consistent with doubled energy of single relaxed cell 2 * -1609.77 = −3219.54 eV. The addition of the *n*-hexane without taking in to account the framework interaction was then−3219.61 − 136.68 = −3356.28 eV, which was used as a reference energy.

For reference and numerical uncertainty estimation purposes, results of calculations using

default grid and Poisson solver are also given below. The calculated energy was –3221.19 eV, which is 1.6 eV lower than the value obtained using relaxed solver settings. The reference energy (framework + hexane) using the more conservative settings was –3221.19 – 136.14 = –3357.33 eV. The 1 eV difference in total energy might be taken as estimate of uncertainty of calculation due to grid and solver settings.

1.8.2.5 Selection of points for *n*-hexane insertion

The *n*-hexane was inserted with the long axis roughly aligned with *a*-axis. The Niggli cell is built of 4 symmetrically independent pores from which the one with the larger area enclosed within the unit cell was chosen for insertion. The sites for the center of the mass on *n*-hexane were selected on a triangular layer build of the iron atoms (Figure S21A) and then propagated along *a*. The number of points per layer was chosen to be 10 with roughly 2.2 Å inter-site distance within a plane perpendicular to a-axis and 1.4 Å between the planes.

1.8.2.6 Results

The analysis of the insertion energy grid was done on 44 out of 90 points, which covered only the upper half of the pore. The final grid was created using radial interpolation from known points. The reference energy –3356.28 eV was subtracted from all sites, 0 eV meant no interaction. On this scale the lowest value was around 0.3 eV, the highest 150 eV. The outside of the probed volume was assigned a high value of 1000 eV in order to plot isosurfaces of the insertion energy using VESTA (Figure S22) (*49*). Additionally, each triangle was separately interpolated using PawConvert utility of DAVE package (Figure S23) (*50*).

The calculations point out several key factors:

a) *n*-hexane can be inserted into a pore almost without any energy penalty (at least within the uncertainty of the method at 0 K), which would be even easier at elevated temperatures,
b) there is no large energy barrier to slide along the pore,
c) despite the 3-fold symmetry of the pore and rather flat carbon backbone of the *n*-hexane, the energy iso-surface is convex, indicating that the *n*-hexane has enough space to rotationally reorient (Figures S17 and S22),
d) however, the projection of the iso-surface on the plane perpendicular to the pore axis (Figure S23) reveals a weak 3-fold preference to align the carbon backbone along the bisectors of the pore angles, which in mathematical terms naturally puts it in the middle of a circle inscribed in the pore. This last point can be understood within the van der Waals energy framework, due to optimal contact area between the inserted molecule and pore walls.

Supplementary Text

2.1 Understanding the adsorption hierarchy with molecular simulations

In order to investigate the fundamental reasons for the hierarchy of adsorption strengths observed in the experiments, we undertook Configurational-Bias Monte Carlo (CBMC) simulations of adsorption. The CBMC simulation methodology used is the same as that described in detail in the published literature (*37*). For linear and branched alkanes, the beads in the chain are connected by harmonic bonding potentials. A harmonic cosine bending potential models the bond bending between three neighboring beads, a Ryckaert-Bellemans potential controls the torsion angle. The force field information provided by Dubbeldam *et al*. (*51*) was used for the variety of potentials. The Lennard-Jones parameters for the framework atoms of $Fe_2(BDP)_3$ are specified in Table S1.

Firstly, the pure component isotherms were determined for nC5, 2MB, neoP, nC6, 2MP, 3MP, 22DMB, 23DMB, nC7, 2MH, 3MH, 22DMP, and 23DMP in $Fe_2(BDP)_3$ at 433 K for a wide range of pressures ranging to 0.1 Pa to 10 MPa. The results for the hexane isomers are plotted in Table S3. These pure component isotherms were fitted with the dual-site Langmuir-Freundlich model to yield the parameters in Table S4.

Figure S24 compares these calculated pure component isotherms with the dual-site Langmuir-Freundlich fits. The fits are excellent in all cases. For the hexane isomers, the hierarchy of loadings nC6 > 2MP ≈ 3MP > 22DMB ≈ 23DMB is precisely that obtained in the experiments (Figure 3). For pentane isomers, Figure S24A indicates the hierarchy nC5 > 2MB > neoP. For heptanes the observed hierarchy nC7 > 2MH ≈ 3MH > 22DMP ≈ 23DMP; see Figure S24C. These hierarchies are best rationalized by examining the location and conformation of each isomer within the triangular channels.

Figure S25 presents snapshots showing the location and conformations of pentane isomers adsorbed within the triangular channels of $Fe_2(BDP)_3$, as a complement to Figure 2. The backbone of nC5 aligns along the gutters, as was the case with nC6. The compact neo-P molecule exerts the least amount of van der Waals interactions with the pore walls, and consequently has the lowest adsorption strength.

2.2 Establishing the validity of IAST calculations

The applicability of the IAST is restricted to cases in which there is a homogenous distribution of adsorbed species throughout the microporous framework. The IAST predictions will fail under a variety of special situations as discussed by Wu *et al.* (*52*).

Since IAST calculations lie at the heart of the breakthrough calculations presented in our paper, we consider it essential to establish the validity of IAST estimations of adsorption of alkane isomer mixtures in $Fe_2(BDP)_3$.

For this purpose CBMC simulations were carried out for adsorption of four different equimolar mixtures in $Fe_2(BDP)_3$ at 433 K: 3-component pentanes: (nC5/2MB/neoP), 5-component hexanes (nC6/2MP/3MP/22DMB/23DMB) 8-component pentanes/hexanes: (nC5/2MB/neoP/nC6/2MP/3MP/22DMB/23DMB), and 13-component pentanes/hexanes/heptanes (nC5/2MB/neoP/nC6/2MP/3MP/22DMB/23DMB/nC7/2MH/3MH/22DMP/23DMP).

The CBMC mixture simulation data, indicated by symbols, are presented in Figure S6. The continuous solid lines are IAST calculations of the mixture equilibrium using the dual-site Langmuir- parameters in Table S4. For all four mixtures there is excellent agreement between CBMC simulated component loadings and IAST calculations.

Having established the accuracy of IAST calcualtions, we proceed with breakthrough calculations.

2.3 Separation potential of $Fe_2(BDP)_3$ for producing high-octane gasoline

For further evaluation of the ability of $Fe_2(BDP)_3$ to produce a 92 RON product, we undertake breakthrough simulations. For hexane isomer separations we use the experimentally determined isotherm fits (parameter values from Table S2).

Firstly, let us consider simulations assuming thermodynamic equilibrium, and no diffusional limitations. Figure S26 presents the simulations of breakthrough characteristics of a fixed bed adsorber packed with $Fe_2(BDP)_3$ operating at a total pressure of 100 kPa and 433 K. The sequence of breakthroughs is the same as in the breakthrough experiments, as is to be expected. In the initial phase of the adsorption cycle, the exit gas stream is richer in the di-branched isomers. As a consequence the RON of the product gas stream has the highest RON values, approaching 100, near the start of the cycle. In all the calculations presented here, the RON of the hydrocarbon mixture is calculated from the pure component RON values in Table S5 averaged over the exit gas composition; no non-linear mixing rules are applied. When the breakthroughs of the mono-branched isomers, 2MP and 3MP, commences the RON of the product gas drops significantly. For the chosen set of operating conditions, a material balance on the adsorber yields information on the amount of 92 RON product that can be recovered. Note that this value of 92 is obtained by averaging over all isomers in the gas phase for the appropriate time interval. The 92 RON productivity, calculated on the basis of the amount of crystalline adsorbent $Fe_2(BDP)_3$ in the packed adsorber, is 0.67 mol kg^{-1} ≡ 0.77 mol L^{-1}. The volumetric productivity is obtained by multiplying the gravimetric productivity by the framework density ρ = 1.145 kg L^{-1}.

The assumption of thermodynamic equilibrium tends to produce sharp breakthroughs as witnessed in Figure S26. The experimental breakthroughs as seen in Figure 4 are more “diffuse”, and the most likely reason is that intra-crystalline diffusion limitations are in play. In order to obtain a more realistic estimate of 92 RON productivity, we performed breakthrough calculations with the inclusion of diffusional influences. For hexane isomers in $Fe_2(BDP)_3$, the values of the Fick diffusivities D_i were taken to be those obtained from MD simulations of self-diffusivities in ZIF-77 at 433 K as reported in Table S9 of the Supporting Material accompanying the paper of Dubbeldam *et al*. (*37*). The channels of ZIF-77 are 4.5 Å in size, similar to that of $Fe_2(BDP)_3$, and the diffusivities in these two materials are expected to be similar in magnitude. The values of D_i used in the breakthrough simulations are

nC6: 5×10^{-10} m^2 s^{-1}
2MP: 1×10^{-10} m^2 s^{-1}
3MP: 1×10^{-10} m^2 s^{-1}
22DMB: 5×10^{-11} m^2 s^{-1}
23DMB: 5×10^{-11} m^2 s^{-1}

The value of the crystallite radius, r_c, used in the breakthrough simulation is 500 μm, that is typical of PSA operations. Consequently, D_{nC6}/r_c^2 = 0.002 s^{-1}; D_{nC6}/D_{2MP} =5; D_{nC6}/D_{3MP} =5; D_{nC6}/D_{22DMB} =10; D_{nC6}/D_{23DMB} =10.

Figure S27 presents the results of the breakthrough simulations including diffusion influences. The breakthrough fronts are less sharp, and more in line with those observed in Figure 4. More diffuse breakthroughs have the effect of lowering the RON productivity in relation to the equilibrium simulations. The 92 RON productivity, obtained from a material balance, is 0.47 mol kg^{-1} ≡ 0.54 mol L^{-1}.

The breakthrough simulations confirm that $Fe_2(BDP)_3$ is capable of incorporation as the adsorbent in the separation step in Figure 1. There are additional features of the separation characteristics of $Fe_2(BDP)_3$ that deserve amplification. The manuscript text discusses the pulsed chromatographic calculations, wherein we are able to "fractionate" the hexanes mixture into three separate fractions, consisting of linear nC6, mono-branched 2MP and 3MP, and di-branched 22DMB and 23DMB. This fractionation ability is more than that demanded by the processing scheme in Figure 1 that requires only separation between mono- and di-branched isomers. To tap this unique ability of $Fe_2(BDP)_3$ we suggest a further process improvement, as depicted in Figure S3, in which we employ staged recycle to the reaction stage of the process. The linear nC6 is mixed with the incoming feed mixture to the isomerization reactor. The mono-branched isomers 2MP and 3MP are recycled to an intermediate location in the reactor. With staged recycle, we have the possibility of improving the conversion of the reaction step with potential increase in conversion and yields for a given reactor volume.

The ability of $Fe_2(BDP)_3$ to fractionate a mixture of 5-component hexane isomer mixtures is also confirmed by breakthrough calculations in which we use CBMC simulations of pure component isotherms in place of the experimentally determined ones; see Figure S28. In view of this agreement, albeit qualitative, between CBMC simulations and our experimental data in $Fe_2(BDP)_3$ we used molecular simulations to further investigate the feasibility of separating other alkane isomer mixtures:

Figure S29 shows the pulse chromatographic simulation results for separation of pentane isomers. This separation of pentane isomers is of importance to the petrochemical industry because 2MB is used as a solvent and as feedstock for production of isoprene by oxidative dehydrogenation. The ability of $Fe_2(BDP)_3$ to separate the mixture into individual fractions offers the possibility of supplanting conventionally used energy-intensive distillation (called de-*iso*pentanizers) with more efficient adsorptive separations.

In industrial practice, the feed to the isomerization reactor also contains the C5 and C7 alkane isomers. So we also investigated the potential of $Fe_2(BDP)_3$ for separating C5/C6 and C5/C6/C7 mixtures. Figure S30 shows the pulse chromatographic simulations for separation of 8-component pentanes/hexanes mixture: nC5/2MB/neoP/nC6/2MP/3MP/22DMB/23DMB using $Fe_2(BDP)_3$. The separation into three fractions based on degree of branching, rather than on C number, is evident. The implications of this fractionation ability is that it is possible to utilize $Fe_2(BDP)_3$ in the separation step of a C5/C6 alkane isomerization process.

Figure S7 presents the pulse chromatographic simulation results for separation of 13-component pentanes/hexanes/heptanes mixture:

nC5/2MB/neoP/nC6/2MP/3MP/22DMB/23DMB/nC7/2MH/3MH/22DMP/23DMP

The separation into three fractions based on degree of branching, rather than on C number, is again evident. The implications of this fractionation ability is that it is possible to utilize $Fe_2(BDP)_3$ in the separation step of a C5/C6/C7 alkane isomerization process scheme.

2.4 Comparison with separation performance of other adsorbents

A search of the published and patent literature reveals that a few other micro-porous adsorbents such as zeolites (MFI (*53,54*), CFI (*55*), ATS (*56*), BETA (*21*), MWW (*57*)), metal-organic frameworks (MOFs) (UiO-66 (*24*), Zn(bdc)dabco (*58*), ZnHBDC (*59*), IM-22 (*18*)), and zeolite imidazolate frameworks (ZIFs) (ZIF-8 and ZIF-76 (*18*)) have been suggested for separation of hexane isomers. These materials cover a wide range of pore sizes, pore topologies and connectivities. However, experimental data on pure component isotherms for all five isomers is not available for any of these materials. For the purposes of making comparisons with the performance of $Fe_2(BDP)_3$ we use the data obtained from CBMC simulations of pure component and mixture isotherms from the recent published literature (*37, 60*).

2.4.1 Comparison of adsorbents using the a previously published methodology

For the evaluation of different adsorbents for a given separation task, the two commonly used metrics are: *adsorption selectivity* and *uptake capacity*.

For a binary mixture the adsorption selectivity is defined as follows

$$S_{ads} = \frac{q_1/q_2}{f_1/f_2} \tag{4}$$

For comparative evaluation of the different adsorbents the extension of this definition for separation of 5-component mixture of nC6 (component 1), 2MP (component 2), 3MP (component 3), 22DMB (component 4), and 23DMB (component 5), each with partial fugacities, f_i, is not straightforward because the hierarchy of adsorption strengths is not the same for all materials. For some materials, such as MFI, and $Fe_2(BDP)_3$ we have the "normal" hierarchy, wherein the linear nC6 has the highest adsorption strength and the di-branched isomers the weakest adsorption strength. For other materials such as UiO-66, MWW, and CFI we have the "reverse" hierarchy, wherein the di-branched isomers have the highest adsorption strength, and the linear nC6 have the weakest adsorption strength. As illustration, Figure S31 shows CBMC data for mixture adsorption in UiO-66 and CFI.

The approach taken by Dubbeldam *et al*. (*37*) is to adopt two different definitions for "normal" and "reverse" hierarchies. For materials with normal hierarchies, they define S_{ads} as

$$S_{ads} = \frac{(q_1+q_2+q_3)/(q_4+q_5)}{(f_1+f_2+f_3)/(f_4+f_5)} \tag{5}$$

For materials with "reverse" hierarchy, they use the definition

$$S_{ads} = \frac{(q_4+q_5)/(q_1+q_2+q_3)}{(f_4+f_5)/(f_1+f_2+f_3)} \tag{6}$$

The corresponding definition of the *uptake capacities* for normal and reverse hierarchies also needs adaptation. Dubbeldam *et al*. (*37*) use the following definition

$$\text{Capacity} = \frac{(q_1 + q_2 + q_3)}{3} \tag{7}$$

for materials with normal hierarchy. For materials with reverse hierarchy the following formula is used

$$\text{Capacity} = \frac{(q_4 + q_5)}{2} \tag{8}$$

The division by 3, and 2, respectively in the two scenarios ensures that the values of the capacities are normalized in the proper manner and that the comparisons are done fairly.

Figure S32 presents a plot of the two capacity metrics, defined in the two foregoing equations, for different host materials. The division into the two broad classes is evident. Table S6 reports these data for numerical clarification.

Figure S33 presents the comparison of adsorption selectivity versus capacity for separation of 5-component nC6/2MP/3MP/22DMB/23DMB mixtures at 433 K. Table S6 reports these data for numerical clarification. With the exception of $Fe_2(BDP)_3$, all the data plotted here are based on CBMC simulations as reported in the paper by Dubbeldam *et al*. (*37*). For a consistent comparison, we plot the CBMC simulation results for $Fe_2(BDP)_3$ (as presented in Figure S6 and S24); these CBMC simulations use the same methodology as Dubbeldam *et al*., (*37*) and therefore provide a fairer comparison. We note that $Fe_2(BDP)_3$ exhibits higher selectivity *and* capacity than ZIF-77 that emerges as the best material for alkane isomer separation task in the study of Dubbeldam *et al*. (*37*), with the fractionating ability similar to that of $Fe_2(BDP)_3$. ZIF-77 was chosen by Dubbeldam on the basis of a large scale *in silico* screening of more than 100 zeolites, MOFs, COFs, ZIFs. An important point to underscore is that there is no experimental data on isotherms or breakthroughs to confirm the separation performance of ZIF-77. Furthermore, the nitro-imidazole ligand in ZIF-77 is extremely expensive, and consequently this material is unlikely to have potential for use in practice.

While it is encouraging to note that $Fe_2(BDP)_3$ emerges as the best adsorbent in the selectivity vs. capacity screening, such an approach for screening adsorbents is fraught with problems when applied to the processing scheme in Figure 1. For materials such as ZIF-8 the separation principle is largely based on "kinetic" considerations, and screening methodology based purely on the basis of adsorption selectivities and capacities is not valid. For several materials, the adsorption hierarchy does not correspond precisely with either "normal" or "reverse" categories. To illustrate this, Figure S34 presents CBMC simulations of 5-component hexanes adsorption in (a) Zn(bdc)dabco, (b) ATS, (c) ZnHBDC, and (d) MIL-53(Cr). For Zn(bdc)dabco and ZnHBDC we have the hierarchies 23DMB > 3MP > 2MP > nC6 > 22DMB, i.e. with the two di-branched isomers at either extremities of the adsorption hierarchies.

For materials with "mixed" hierarchies, the definitions of selectivity and capacity in equations (5), (6), (7), and (8) do not appear to be reasonable because these require two groupings: (nC6, 2MP, 3MP), (22DMB, 23DMB) that cannot be justified for mixed hierarchies; such groupings are meaningful only if the component loadings of the components in each group are contiguous.

Insights into factors determining the hierarchies is provided in the CBMC simulation data of Dubbeldam *et al*. (*37*) for graphite channels of square cross-section, and graphite slits. The isosteric heats of adsorption of each of the hexane isomers, relative to that of nC6 are plotted as a function of the effective channel spacing in Figure S35. The hierarchy of $-Q_{st}$ values is a reflection of the adsorption hierarchy. The "normal" hierarchy of adsorption strengths is found

to prevail for channels (a) smaller than 5.5 Å, and (b) larger than about 8.5 Å; this is evident in the plot in Figure S36 of uptake capacity vs. characteristic pore dimensions for different host materials, which is also reported in Table S6. This explains why we find ZIF-77 (4.5 Å square channels), $Fe_2(BDP)_3$ (4.9 Å triangular channels), Co(BDP) (9.9 Å square channels), and MgMOF-74 (10.7 Å hexagonal channels) exhibit normal hierarchy. For channel distances in the 6 Å to 8 Å range, the hierarchy can be either "reverse" or "mixed". This rationalizes the data for the MOFs and zeolites in Figures S32 and S33. It is remarkable to note the dramatic changes in the relative adsorption strengths, and hierarchies, as the channel spacing is increased from 5 Å to 6 Å; we will obtain confirmatory evidence of this that examines separations with MIL-140 (Section 2.4.14).

Without a detailed analysis of the breakthrough characteristics of adsorbents with reverse or mixed hierarchies, it is not possible to decide about the suitability for producing 92 RON product gas.

2.4.2 Comparison methodology used in this work

In view of the arguments presented above, we proceed with the comparisons of various materials with $Fe_2(BDP)_3$ by determining the 92 RON productivities in fixed bed adsorbers using breakthrough simulations. For each material, we choose identical set of conditions for comparison: total pressure, p_t = 100 kPa, equimolar feed of 5-component hexane isomer mixture ($p_1 = p_2 = p_3 = p_4 = p_5$ = 20 kPa); temperature, T = 433 K. The adsorbents chosen for comparison are those for which there is experimental data confirming the separation potential. For consistency in the comparisons, we use CBMC simulations of pure component and mixture isotherms, to evaluate the separation characteristics after verification that the data are in reasonable accord with the experimental information. For materials such as ZIF-8, for which the diffusional effects are of primary importance, we also introduce diffusional influences in the analysis. Materials such as Co(BDP), MgMOF-74, ZnMOF-74, and ZIF-77 which emerge as promising candidates in *in silico* screening studies (*37, 60*), are not included in the comparisons in view of the lack of experimental data to confirm their potential. Table S7 displays a summary of the results for each material.

The evaluations of materials with "normal", "reverse", and "mixed" hierarchies are considered separately.

2.4.3 Materials with "normal" adsorption hierarchies: general remarks

For this class of materials, implementation into the processing scheme in Figure 1 is straightforward. During the initial phase of the adsorption cycle, the product gas is rich in the less-strongly adsorbed di-branched isomers. The product gas mixture with the desired RON value of 92 (chosen in this study on the basis of its relevance to industrial practice) can be removed for incorporation into the gasoline pool. For calculating the productivity we stipulate that the RON value of the entire gas mixture, thus extracted, has an average RON value of 92. Once the desired RON product is recovered, the adsorption cycle is terminated. The more strongly adsorbed components need to be desorbed to obtain a gas phase that is recycled to the isomerization. A desirable property of the desorbent is that it should have a stronger adsorption strength than nC6, and be suitable for recycle to the reactor. For example, nC7 would be a

suitable desorbent material for this task. nC7 has a RON value of 0, and would benefit from further branching in the isomerization reactor.

2.4.4 Materials with "reverse" and "mixed" adsorption hierarchies: general remarks

The adsorbents UiO-66, MWW, CFI, ZIF-76 belong to a different category of materials for which the "reverse" adsorption hierarchy prevails for hexane isomers with di-branched > mono-branched > linear nC6. The reasons for this "reverse" adsorption hierarchy is not the same in every case. For UiO-66 and MWW, the di-branched isomers are preferentially lodged in the tetrahedral cages which provide "snug" fits and high adsorption strengths for the di-branched isomers (*24, 37)*. In the papers by Denayer e*t al*. (*59*) and Bárcia *et al*. (*13*), the stronger adsorption of the di-branched isomers in the octahedral cages is attributed to *rotational entropy* considerations. CFI and ATS zeolites, patented by Chevron for application in the alkane isomerization process (*55,56*), have one-dimensional channels similar to that of AFI zeolite. This hierarchy can be rationalized by examining the snapshot in Figure S37, showing the molecular conformations. The linear nC6 has a longer "footprint" and occupies a larger segment of the channel. 22DMB and 23DMB are the most compact molecules and have the smallest footprint; consequently, more di-branched isomers can be located within a given length of the channels when compared to nC6. 2MP and 3MP have footprints that have an intermediate character. Molecular length entropy effects dictates the sorption hierarchy in CFI, and ATS; a similar situation holds for MOR that has 0.65 nm × 0.7 nm sized 1D channels (*20, 59, 63*). The reverse hierarchy for ZIF-76 observed in the experiments of Peralta *et al*. (18) is more difficult to rationalize because the framework has a considerable degree of disorder. Molecular simulations for unraveling the adsorption mechanisms are not feasible unless the structure is properly resolved.

For materials with "reverse" or "mixed" adsorption hierarchy, the sequence of breakthroughs obtained in simulations shown in Figure S38; the linear nC6 is the earliest to exit the adsorber, and the di-branched 23DMB is the last to exit the adsorber. In practice, the adsorption cycle will be terminated when the linear and mono-branched isomers exit the adsorber; the product gases will be routed to the isomerization reactor. The contents of the bed will need to be desorbed in order to recover the di-branched isomers with high RON values. Therefore, the 92 RON product can be recovered only in the desorption cycle. The 92 RON productivity is crucially dependent on the "purge" or desorption gas used, and its RON value. The choice of the purge gas is of crucial importance because, depending on its adsorption strength and diffusivity, it will appear in the exit gaseous stream along with the di-branched isomers. Unless the RON value of the desorbent is higher than 92, the presence of desorbents in the exit gas will have the effect of reducing the productivity. This implies that the desorbent gas should have a high RON value, not significantly below 92; it should also be suitable for incorporation into the gasoline pool. These requirements are stringent, and it is not immediately obvious which desorbent or purge gas is suitable for this task. For every material the best desorbent will be different. In view of the practical technological problems, Peralta *et al*. (18) remarked that ZIF-76 is unsuitable for application in the scheme of Figure 1, because of its "reverse" hierarchy.

For purposes of comparisons with $Fe_2(BDP)_3$ we choose a pragmatic approach by using a "hypothetical" desorbent, with significantly high adsorption strength,*and* high diffusivity; such a desorbent is unlikely to be found. This choice ensures that the RON of the product gas is not diluted with desorbent gas. For RON productivity calculations, we just ignore the presence of

any traces of desorbents in the gas phase. This method of analysis provides an "upper bound" of the RON productivity values.

2.4.5 MFI zeolite

MFI has a pore topology consisting of a set of intersecting channels of 5.5 Å size. The linear nC6 can locate along either the straight or zig-zag channels, whereas the mono-branched, and di-branched isomers are preferentially located at the channel intersections that offers additional "leg room" (*20, 53-67*). There are four intersections per unit cell, and this limits the loadings of the branched isomers to 4 molecules per unit cell at 100 kPa. The linear nC6 has a molecular length that is commensurate with the distance between two intersections, and has a saturation capacity of 8 molecules per unit cell (*53*). Entropy effects are the reasons for the separation power of MFI zeolite, and several publications in the literature explain how these effects can be exploited in the alkane isomerization process (*50, 68, 69*). MFI is included in the list of zeolites patented by UOP for separation of alkane isomers (*61,62*).

Experimental data and MD simulations have established that the diffusivities of the mono- and di-branched isomers are significantly lower than those of the linear nC6 (*54, 70*). For a realistic evaluation of the separation power of MFI, it is important to include diffusional effects. We choose the set of diffusivity values that are based on the available data in the literature (*50, 68, 69*); the breakthrough simulations are shown in Figure S39. The results clearly demonstrate the ability of MFI zeolite to produce a product of 92 RON; the 92 RON productivity is determined to be 0.51 mol L^{-1}, slightly lower than the corresponding value obtained with $Fe_2(BDP)_3$. The important advantage of $Fe_2(BDP)_3$ is the ability to separate C5/C6/C7 mixtures but such separation capability has not been established for MFI zeolite.

2.4.6 BETA zeolite

Bárcia *et al*. (*21*) report pure component isotherm data and breakthrough experiments with nC6/3MP/22DMB/23DMB mixtures to demonstrate the feasibility for separation of hexane isomers using BETA zeolite, also known as BEA zeolite. Using their experimental isotherms, we performed breakthrough simulations to obtain information on the diffusivities. On this basis, the following set of values ensures good agreement with the breakthrough data in Figure 12 of their paper: $D_{nC6}/r_c^2 = 0.0004$ s^{-1}; $D_{nC6}/D_{3MP} = 1$; $D_{nC6}/D_{22DMB} = 1$; $D_{nC6}/D_{23DMB} = 1$. With this information, and with the additional assumption that the adsorption and diffusion characteristics of 2MP and 3MP are identical, we obtain the breakthrough curves shown in Figure S40 for our chosen standard set of conditions for comparison. The 92 RON productivity value is determined to be 0.36 mol L^{-1}, significantly lower than the corresponding value obtained with $Fe_2(BDP)_3$.

2.4.7 Zn(bdc)dabco

The breakthrough experiments of Bárcia *et al*. (*58*) for nC6/3MP/22DMB mixtures with Zn(bdc)dabco provides evidence of its potential for separation of alkane isomers, and we proceed to examine it potential for separation of 5-component hexane mixtures. Figure S41A presents the simulations of breakthrough characteristics of Zn(bdc)dabco for a 5-component hexanes mixture, including diffusional influences The choice of diffusivities is guided by the sequence of breakthroughs in the experiments of Bárcia *et al*. (*58*). It is interesting to note that after introduction of diffusivities, the sequence of breakthroughs is "normal", whereas the sequence of component loadings from CBMC mixture simulations (Figure S34A) indicates a "mixed"

hierarchy. Indeed, Dubbeldam *et al*. (*37*) have discarded Zn(bdc)dabco as a potential candidate for use in the processing scheme of Figure 1 because of its "mixed" hierarchy.

The 92 RON productivity, calculated on the basis of the amount of crystalline adsorbent Zn(bdc)daboc in the packed adsorber, is 0.48 mol L^{-1}, lower than that obtained with $Fe_2(BDP)_3$.

2.4.8 ZnHBDC

The pure component isotherm experiments for 298 K of Ling *et al*. (*59*) show the adsorption hierarchy nC6 > 3MP > 22DMB in ZnHBDC. At a temperature of 433 K, relevant to industrial processing, however, CBMC simulations indicate the adsorption hierarchy 23DMB > 2MP ≈ 3MP > nC6 > 22DMB; see Figure S34C. Figure S41B presents the simulations of breakthrough characteristics of ZnHBDC for a 5-component hexanes mixture, including diffusional influences. The data on diffusivities is the same as that for Zn(bdc)dabco, and is guided by the sequence of breakthroughs in the experiments of Bárcia *et al*. (*58*). It is interesting to note that after introduction of diffusivities, the sequence of breakthroughs is "normal", whereas the sequence of component loadings from CBMC mixture simulations (Figure S34C) indicates a "mixed" hierarchy. Indeed, Dubbeldam *et* al. (*37*) have discarded ZnHBDC as a potential candidate for use in the processing scheme of Figure 1 because of its "mixed" hierarchy. The 92 RON productivity, calculated on the basis of the amount of crystalline adsorbent ZnHBDC in the packed bed adsorber, is 0.20 mol L^{-1}, significantly lower than that obtained with $Fe_2(BDP)_3$.

2.4.9 ZIF-8

The adsorption hierarchy for ZIF-8 is "mixed" (see CBMC simulation data of Dubbeldam *et al*. (*37*)) but in the recent paper by Peralta *et al*. (*18*), ZIF-8 emerged as the best adsorbent for hexanes isomer separation. Clearly, the separation performance cannot be judged solely on the basis of the mixture adsorption characteristics; diffusional aspects are in play and the separation characteristics of ZIF-8 needs a detailed analysis of this aspect. For this purpose, we first attempt to obtain a match with the breakthrough experiments of Peralta *et al*. (*18*) for nC6/3MP, nC6/22DMB, and 3MP/22DMB mixtures as reported in their Figures 6, 8 and 9, respectively. In each case, two types of simulations were performed: (a) assuming thermodynamic equilibrium, and (b) introducing intra-crystalline diffusion resistances in order to match their breakthrough experiments.

Figure S42 presents the breakthrough simulations for nC6/3MP mixture. The equilibrium simulations (Figure S42A) show that nC6 breaks through earlier than 3MP, whereas the experiments show the reverse trend. The experimental breakthroughs can be reproduced nearly quantitatively by introducing diffusional influences, and by choosing the ratio of diffusivities of nC6 to 3MP to be 100; see. Figure S42B. This ratio of 100 is reasonable for inter-cage hopping across flexible windows with a size of 3.26 Å.

Figure S43 shows the breakthrough simulations for nC6/22DMB mixture. In this case, equilibrium simulations (Figure S43A) predict the correct hierarchies of breakthrough as in the experiments. A near quantitative agreement in the breakthrough characteristics is obtained by accounting for intra-crystalline diffusion with the ratio of diffusivities of nC6 to 22DMB as 300; see Figure S43B.

Figure S44 shows the breakthrough simulations for 3MP/22DMB mixtures. The experimental breakthroughs are reproduced nearly quantitatively by introducing diffusional limitations and taking, for consistency, the ratio of diffusivities of 3MP to 22DMB to be equal to 3.

Having established the diffusion characteristics of nC6, 3MP, and 22DMB in ZIF-8 we proceed with breakthrough simulations in a 5-component mixture, assuming: (a) 2MP and 3MP have equal diffusivities, (b) 22DMB and 23DMB also have equal diffusivities; the breakthrough simulation results are presented in Figure S45. The 92 RON productivity is calculated to be 0.46 mol L^{-1}, lower than that obtained with $Fe_2(BDP)_3$.

2.4.10 UiO-66

Figure S46 shows the adsorption/desorption cycles for UiO-66, operating at a total pressure of 100 kPa and 433 K. At $\tau = 120$, the "hypothetical" desorbent is introduced, and the hexanes feed is stopped. The time at which the desorbent is introduced was obtained after a careful optimization procedure which ensures that the maximum productivity is realized. The simulations in Figure S46 are performed assuming thermodynamic equilibrium. We note that 92 RON product can be recovered towards the end of the cycles. Due to the fact that the desorbent has been chosen to have a high adsorption strength, its breakthrough occurs nears the end of the cycle. As a result, it does not dilute the product gas containing di-branched isomers. The 92 RON productivity value is calculated to be 0.87 mol L^{-1}, higher than the equilibrium productivity value of 0.77 mol L^{-1}, obtained with $Fe_2(BDP)_3$. The equilibrium RON productivity of UiO-66 is too optimistic because the breakthroughs of the di-branched isomers 22DMB and 23DMB will occur significantly earlier if diffusional effects are included. Earlier breakthroughs of 22DMB and 23DMB will result in the product gas being "diluted" with mono-branched and linear isomers, with lower RON values. Clearly, for a proper comparison with $Fe_2(BDP)_3$, we need to introduce diffusivity influences in the calculations.

In order to get insights into the diffusion influences, we examine the breakthrough experiments of Bárcia *et al*. (*24*) for nC6/3MP/22DMB/23DMB mixture separation at 433 K using UiO-66. A reasonable match of the hierarchy of breakthroughs can be obtained by the introduction of diffusion influences taking the values $D_{nC6}/r_c^2 = 0.0004$ s^{-1}; $D_{nC6}/D_{2MP} = 2$; $D_{nC6}/D_{22DMB} = 2$; $D_{nC6}/D_{23DMB} = 2$; see Figure S47.

With this information we performed breakthrough simulations of the adsorption/desorption cycles with desorbent injection at $\tau = 120$; see results in Figure S48. A visual comparison of the breakthroughs for the equilibrium case (Figure S44), with those including diffusional effects (Figure S48), indicates that the diffusion has the effect of producing less-sharp breakthroughs of the di-branched isomers. The net result is that the 92 RON productivity is reduced from 0.77 mol L^{-1} to 0.36 mol L^{-1}, which is more than a 50% reduction. The obtained productivity of 0.36 mol L^{-1} is significantly lower than the corresponding value of 0.54 mol L^{-1} for $Fe_2(BDP)_3$.

The Bárcia *et al*. (*24*) breakthrough experiments consider only the adsorption cycle and does not address the important issue of the choice of the desorbent, and its influence on the RON of product gas.

2.4.11 MWW

The adsorption/desorption cycles for MWW (also known as MCM-22 or ITQ-1) are shown in Figure S49 for a fixed bed adsorber operating at thermodynamic equilibrium. The 92 RON productivity is determined to be 0.52 mol L^{-1}, slightly lower than the corresponding value of 0.54 mol L^{-1} for $Fe_2(BDP)_3$.

To explore the influence of diffusivities we examine the pulse chromatographic simulations for separation of a 5-component hexane mixtures in an equilibrium adsorber; see Figure S50. The

sequence of breakthroughs is nC6, 2MP, 3MP, 22DMB, and 23DMB, reflecting the hierarchy of adsorption strengths. The pulse chromatographic experiments of Denayer *et al.* (*57*) for a nC6/3MP/22DMB mixture shows that the sequence is 22DMB, nC6, and 3MP. Such a sequence implies that the diffusivity of 22DMB is significantly lower than that of the other isomers. The hopping of di-branched isomers into- and out- of the octahedral cages is the limiting factor. Low diffusivities of the di-branched isomers will have the effect of reducing 92 RON productivity of MWW to values significantly lower than 0.52 mol L^{-1}. Our conclusion is that MWW is unlikely to be a candidate adsorbent for alkane isomers separation.

2.4.12 CFI

Figure S51 shows the adsorption/desorption cycles for CFI using a hypothetical desorbent, injected at $\tau = 70$. The best-case scenario of equilibrium adsorber (Figure S51A) yields a 92 RON productivity value of 0.5 mol L^{-1}. Introduction of diffusional influences (Figure S51B), results in a drastic reduction in the productivity to 0.175 mol L^{-1}, clearly inferior to that obtained with $Fe_2(BDP)_3$.

2.4.13 ATS

Figure S52 shows the adsorption/desorption cycles for ATS using an hypothetical desorbent, injected at $\tau = 70$. The best-case scenario of equilibrium adsorber (Figure S52A) yields a 92 RON productivity value of 0.26 mol L^{-1}. Introduction of diffusional influences (Figure S52B), results in a reduction in the productivity to 0.17 mol L^{-1}, which is lower than that obtained with $Fe_2(BDP)_3$.

2.4.14 MIL-140A-D

Based on the comparisons presented above, $Fe_2(BDP)_3$ emerges as the adsorbent with the best 92 RON productivity. The normal hierarchy of adsorption strengths, along with its propensity to fractionate C5/C6/C7 mixtures into three fractions based on the degree of branching, are important advantages for practical implementation. We now examine whether improvements in the separation performance can be obtained by using triangular channels with either a small decrease, or increase, in the pore sizes. The recent publication of Guillerm *et al.* (*39*) reports the synthesis of four different structures with triangular channels. MIL-140A, MIL-140B, MIL-140C, MIL-140D.

The effective pore sizes, determined from molecular simulations as reported in the paper by Dubbeldam *et al.* (*37*), are

MIL-140A: 3.2 Å
MIL-140B: 4.1 Å
MIL-140C: 5.8 Å
MIL-140D: 6.3 Å

MIL-140A, and MIL-140B have smaller pores compared to $Fe_2(BDP)_3$, whereas the channels of MIL-140C, and MIL-140D are larger in size.

CBMC simulations confirm that the channels of MIL-140A are too small to accommodate any of the hexane isomers; see isotherm data in Dubbeldam *et al.* (*37*). MIL-140B operates as a sieve and can accommodate only nC6, and almost none of the branched isomers; see isotherm data in Dubbeldam *et al.* *(37)* consequently, this cannot be applied for the processing scheme of Figure 1.

Figure S53 shows the CBMC simulations of pure component and mixture isotherms in MIL-140C. At low pressures, the hierarchy of loadings can be termed as "mixed": 23DMB ≈ 3MP ≈ 2MP ≈ nC6 > 22DMB. This hierarchy corresponds to that dictated by the relative $-Q_{st}$ values in Figure S35 for an effective spacing of 5.8 Å. At higher pressures, the linear nC6 has the lowest adsorption strength; this characteristic is similar to that found with ATS zeolite as seen in Figure S34B. The reason for the lower nC6 loading at high pressures is traceable to its longer footprint (Figure S37) which allows fewer nC6 molecules to be packed within a given channel length.

For a fixed bed adsorber operating at a pressure of 100 kPa, the 92 RON product can be recovered with MIL-140C only at the end of the desorption cycle (Figure S54A). For an optimistic scenario in which thermodynamic equilibrium is assumed, the 92 RON productivity is determined to be 0.25 mol L^{-1}, which value is significantly lower than that obtained with $Fe_2(BDP)_3$.

The adsorption characteristics of MIL-140D are very similar to that of MIL-140C; the corresponding breakthrough simulations of the adsorption/desorption cycles are shown in Figure S54B. The 92 RON productivity of an equilibrium adsorber is determined to be 0.20 mol L^{-1}.

If diffusional influences were to be included in the adsorption/desorption simulations, the 92 RON productivities would be further reduced for the reasons explained in the foregoing section.

The significantly inferior performance of both MIL-140C and MIL-140D, as compared to $Fe_2(BDP)_3$, is mainly due to the shift in the adsorption hierarchy from "normal" to "mixed" or "reverse" that results from increasing the size of the triangular channels from 4.9 Å to 5.8 Å, or higher. The $-Q_{st}$ values in Figure S35 also indicate that attempts to improve on the separation performance of $Fe_2(BDP)_3$ by constructing a MOF with slightly larger channel dimensions may not be successful.

2.5 Notation

b_A	dual-Langmuir-Freundlich constant for species *i* at adsorption site A, $Pa^{-\nu_i}$
b_B	dual-Langmuir-Freundlich constant for species *i* at adsorption site B, $Pa^{-\nu_i}$
D_i	Fick diffusivity of species *i*, $m^2\ s^{-1}$
E_A	Energy parameter for site A in DLF isotherm, J mol^{-1}
E_B	Energy parameter for site B in DLF isotherm, J mol^{-1}
f_i	fugacity of species *i*, Pa
f_t	total fugacity of mixture, Pa
L	length of packed bed adsorber, m
n	number of components in mixture, dimensionless
N_i	molar flux of species *i*, mol $m^{-2}\ s^{-1}$
p_i	partial pressure of species *i*, Pa
p_t	total system pressure, Pa
q_i	component molar loading of species *i*, mol kg^{-1}
q_t	total molar loading in mixture, mol kg^{-1}
$q_{sat,A}$	saturation loading of site A, mol kg^{-1}
$q_{sat,B}$	saturation loading of site B, mol kg^{-1}
Q_{st}	isosteric heat of adsorption, J mol^{-1}
r	radial coordinate, m
r_c	radius of crystallite, m
R	gas constant, 8.314 J $mol^{-1}\ K^{-1}$
S_{ads}	adsorption selectivity, dimensionless
t	time, s
T	absolute temperature, K
u	superficial gas velocity in packed bed, m s^{-1}
v	interstitial gas velocity in packed bed, m s^{-1}
z	distance along the adsorber, m

Greek letters

ε	voidage of packed bed, dimensionless
ν	exponent in dual-Langmuir-Freundlich isotherm, dimensionless
ρ	framework density, kg m^{-3}
τ	time, dimensionless
τ_{break}	breakthrough time, dimensionless

Subscripts

i	referring to component *i*
A	referring to site A
B	referring to site B

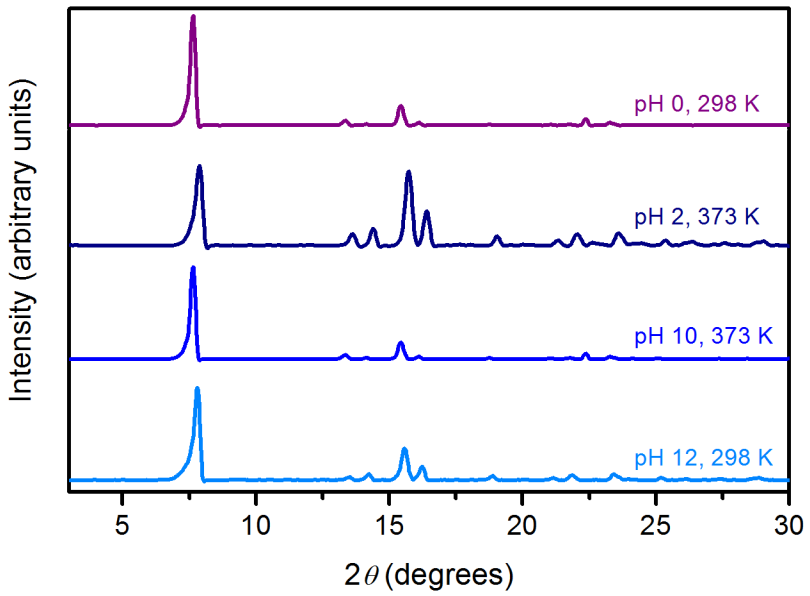

Figure S1. X-ray powder diffraction patterns of 20 mgs of $Fe_2(BDP)_3$ after 14 day soaking in 10 mL of pH 0 and pH 14 water at 298 K and pH 2 and pH 10 water at 398 K.

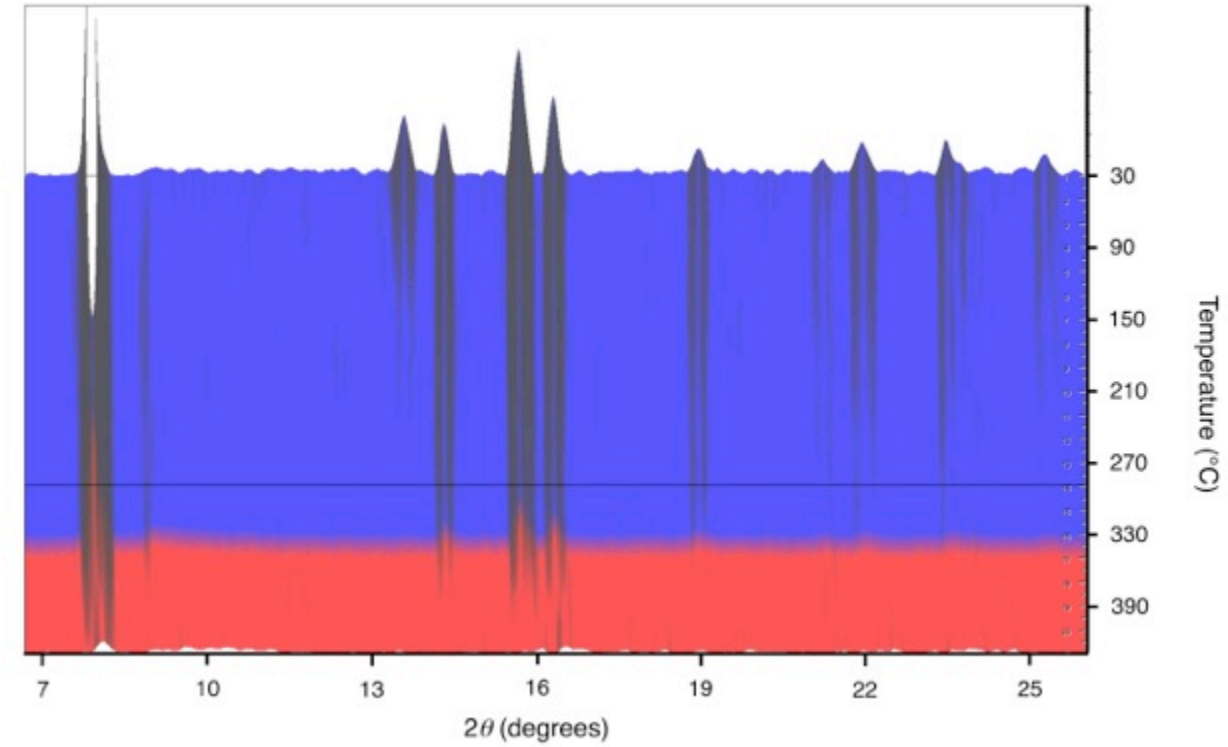

Figure S2. X-ray powder diffraction patterns of $Fe_2(BDP)_3$ heated in air between 298 K and 498 K recorded in the 2θ range of 7–26°. The heating was carried out *in situ* in 20 K increments.

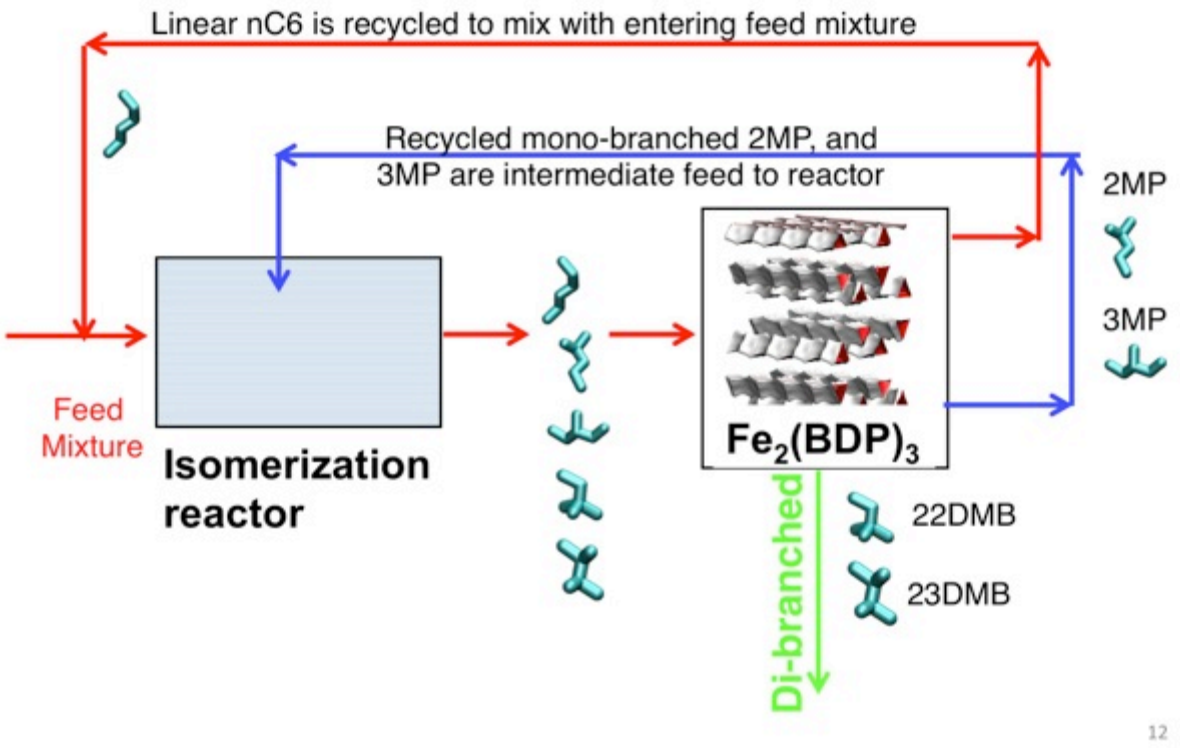

Figure S3. Alkane isomerization process incorporating $Fe_2(BDP)_3$ in the separation step and with staged recycle of linear nC6 and mono-branched 2MP and 3MP to the isomerization reactor.

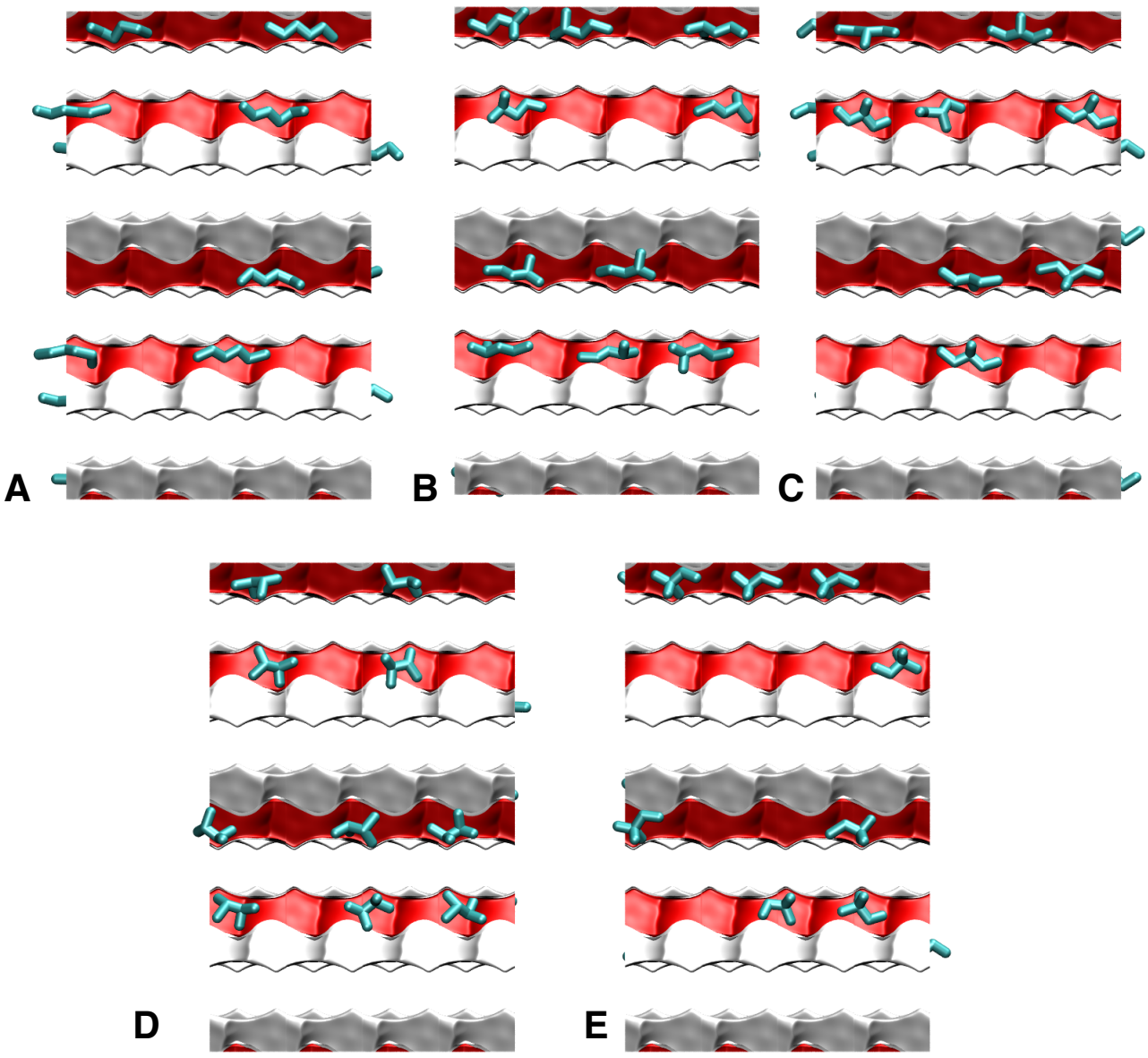

Figure S4. Side-on snapshots of (**A**) *n*-hexane, (**B**) 2-methylpentane, (**C**) 3-methylpentane, (**D**) 2,3-dimethylbutane, and (**E**) 2,2-dimethylbutane within the channels of $Fe_2(BDP)_3$ for a loading of four molecules per unit cell at 160 °C, as observed in configurational-bias Monte Carlo simulations.

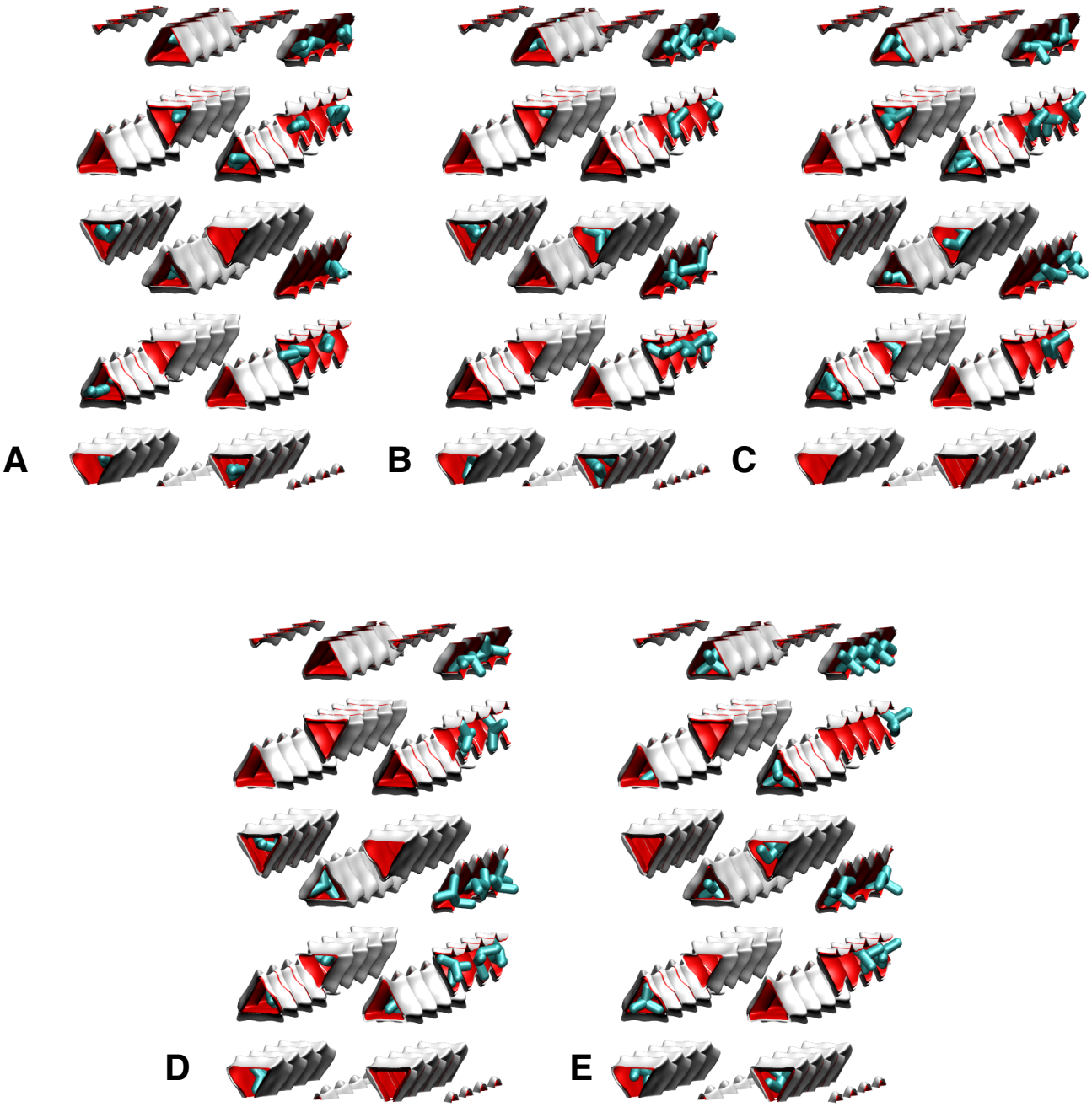

Figure S5. End-on snapshots of (**A**) *n*-hexane, (**B**) 2-methylpentane, (**C**) 3-methylpentane, (**D**) 2,3-dimethylbutane, and (**E**) 2,2-dimethylbutane within the channels of $Fe_2(BDP)_3$ for a loading of four molecules per unit cell at 160 °C, as observed in configurational-bias Monte Carlo simulations.

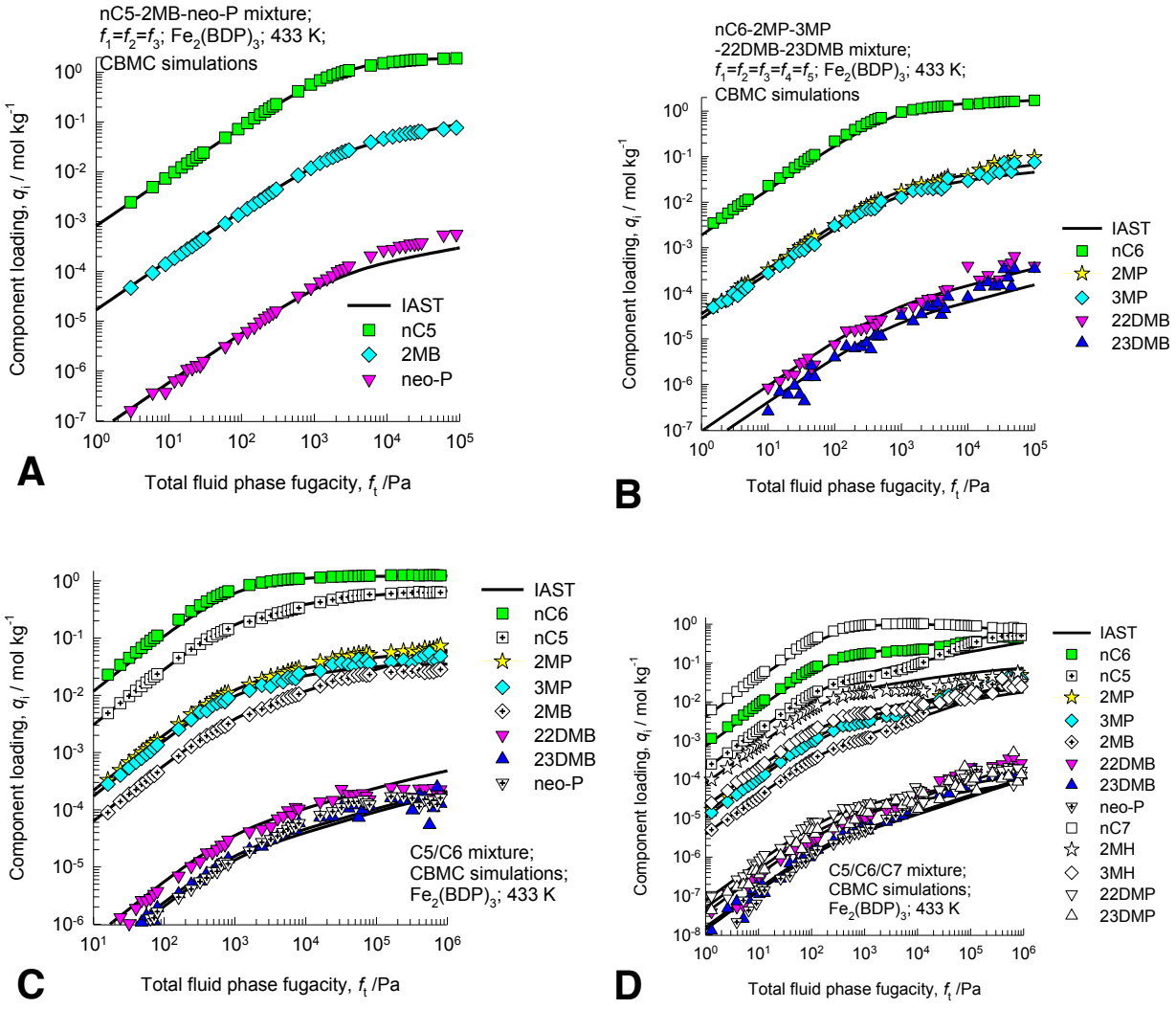

Figure S6. CBMC simulations of four different mixtures: 3-component pentanes: nC5/2MB/neoP (**A),** 5-component hexanes: nC6/2MP/3MP/22DMB/23DMB (**B**), 8-component pentanes/hexanes: nC5/2MB/neoP/nC6/2MP/3MP/22DMB/23DMB (**C**), and 13-component pentanes/hexanes/heptanes nC5/2MB/neoP/nC6/2MP/3MP/22DMB/23DMB/nC7/2MH/3MH/22DMP/23DMP (**D**) in $Fe_2(BDP)_3$ at 433 K. Note that the *x*-axes indicate the total fugacity, f_t, of the mixture in the gas phase. For all four mixtures the partial fugacities of each component in the mixture is taken to be the same, i.e. $f_1 = f_2 = f_3 = f_4 = f_5 = \ldots f_{13}$. The continuous solid lines are the calculations of component loadings using the Ideal Adsorbed Solution Theory.

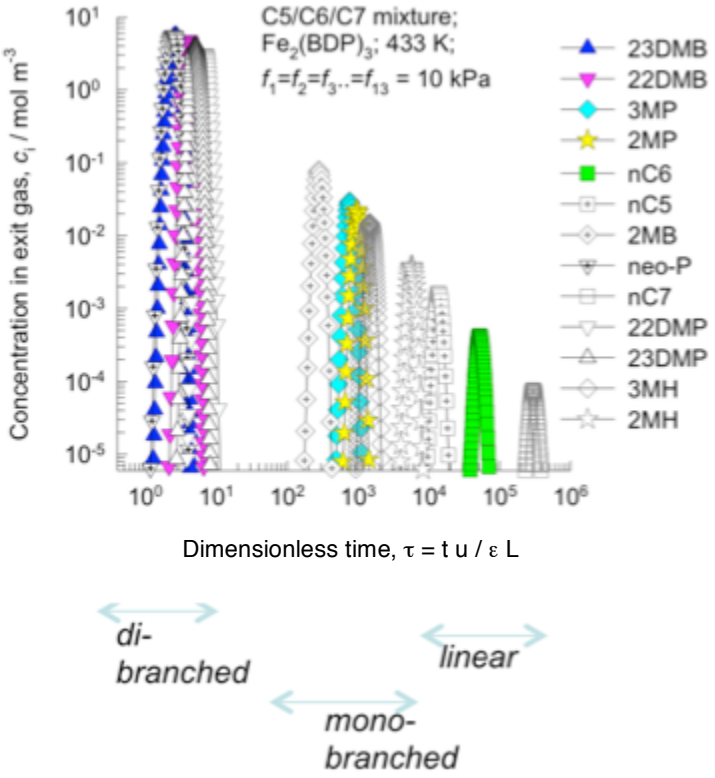

Figure S7. Pulse chromatographic simulation of 13-component pentanes/hexanes/heptanes nC5/2MB/neoP/nC6/2MP/3MP/22DMB/23DMB/nC7/2MH/3MH/22DMP/23DMP using $Fe_2(BDP)_3$. These simulations are carried out using pure component isotherm fits of CBMC simulations. No diffusional influences are accounted for in this case.

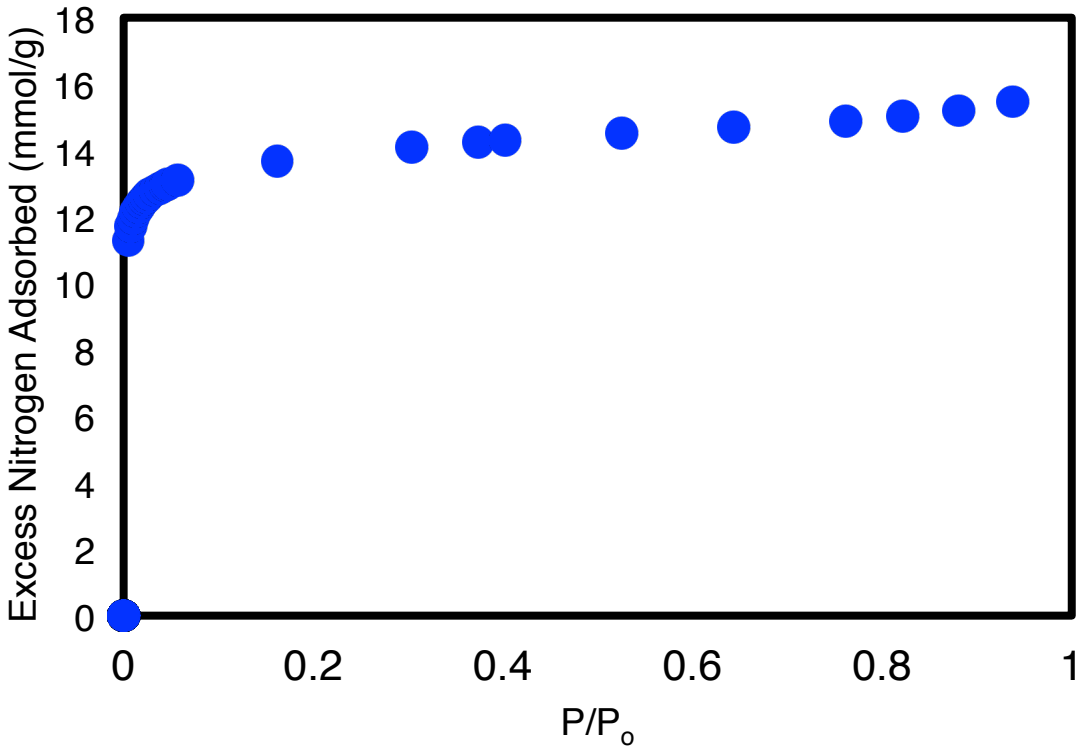

Figure S8. 77 K N_2 adsorption isotherm on $Fe_2(BDP)_3$.

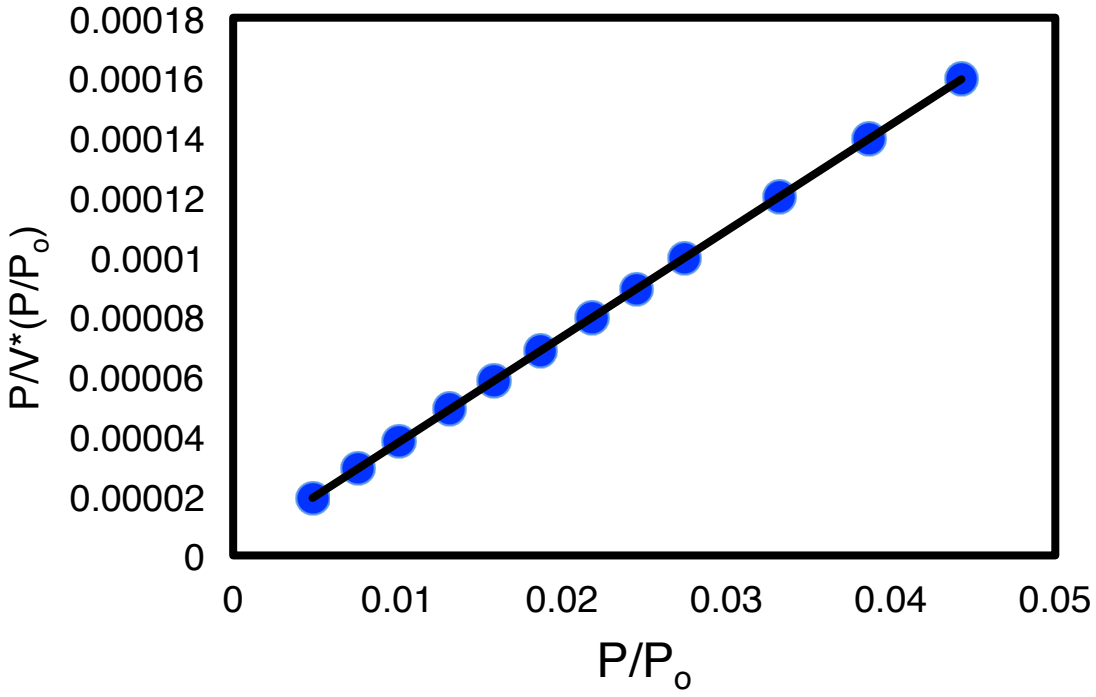

Figure S9. Points used to determine BET surface area of $Fe_2(BDP)_3$, fit with a linear trendline.

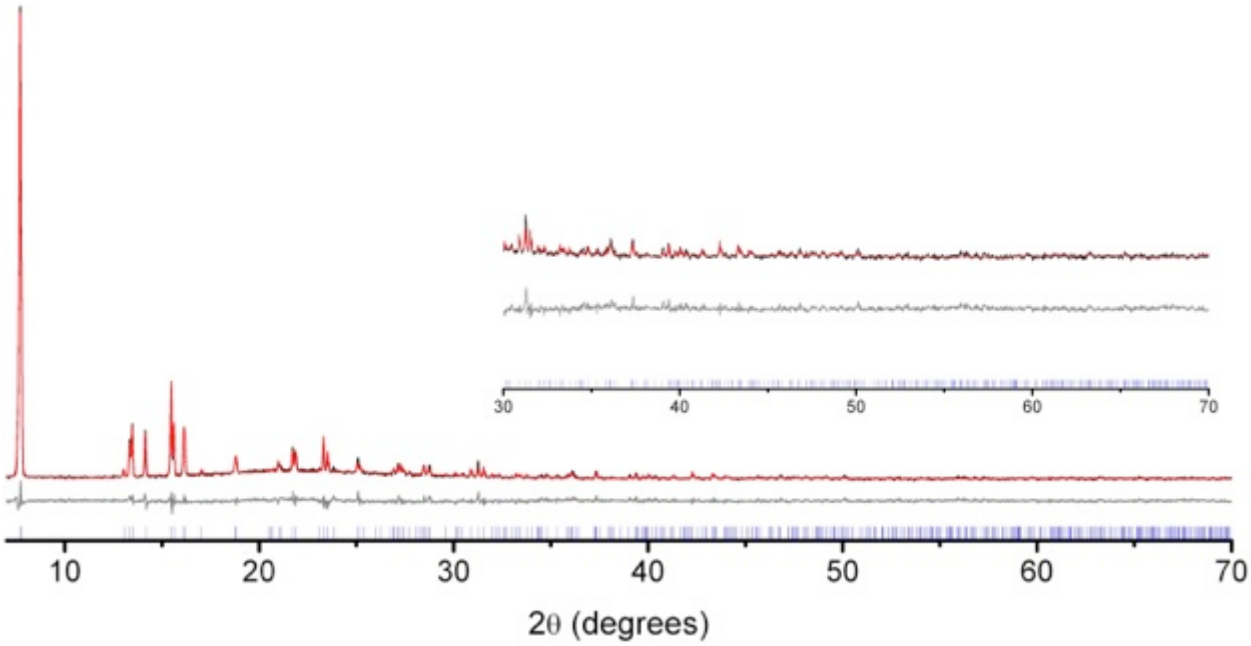

Figure S10. X-ray powder diffraction data for as-synthesized Fe_2BDP_3 collected in Debye-Scherrer (capillary) mode. Black and red lines represent the experimental and calculated diffraction patterns, respectively. The gray line represents the difference between experimental and calculated patterns, and the blue lines designate the Bragg peak positions. The insert represents the high angle region at a magnified scale.

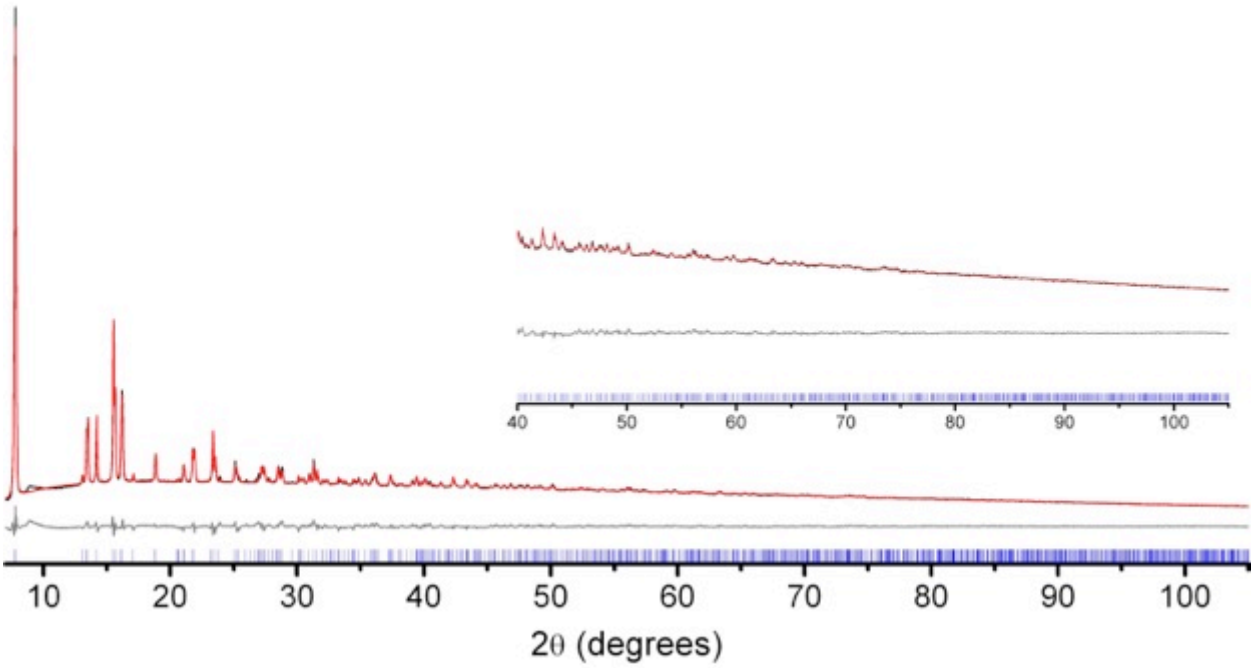

Figure S11. X-ray powder diffraction data for as-synthesized Fe_2BDP_3 collected in Bragg-Brentano (flat-plate) geometry. Black and red lines represent the experimental and calculated diffraction patterns, respectively. The gray line represents the difference between experimental and calculated patterns, and the blue lines designate the Bragg peak positions. The insert represents the high angle region at a magnified scale.

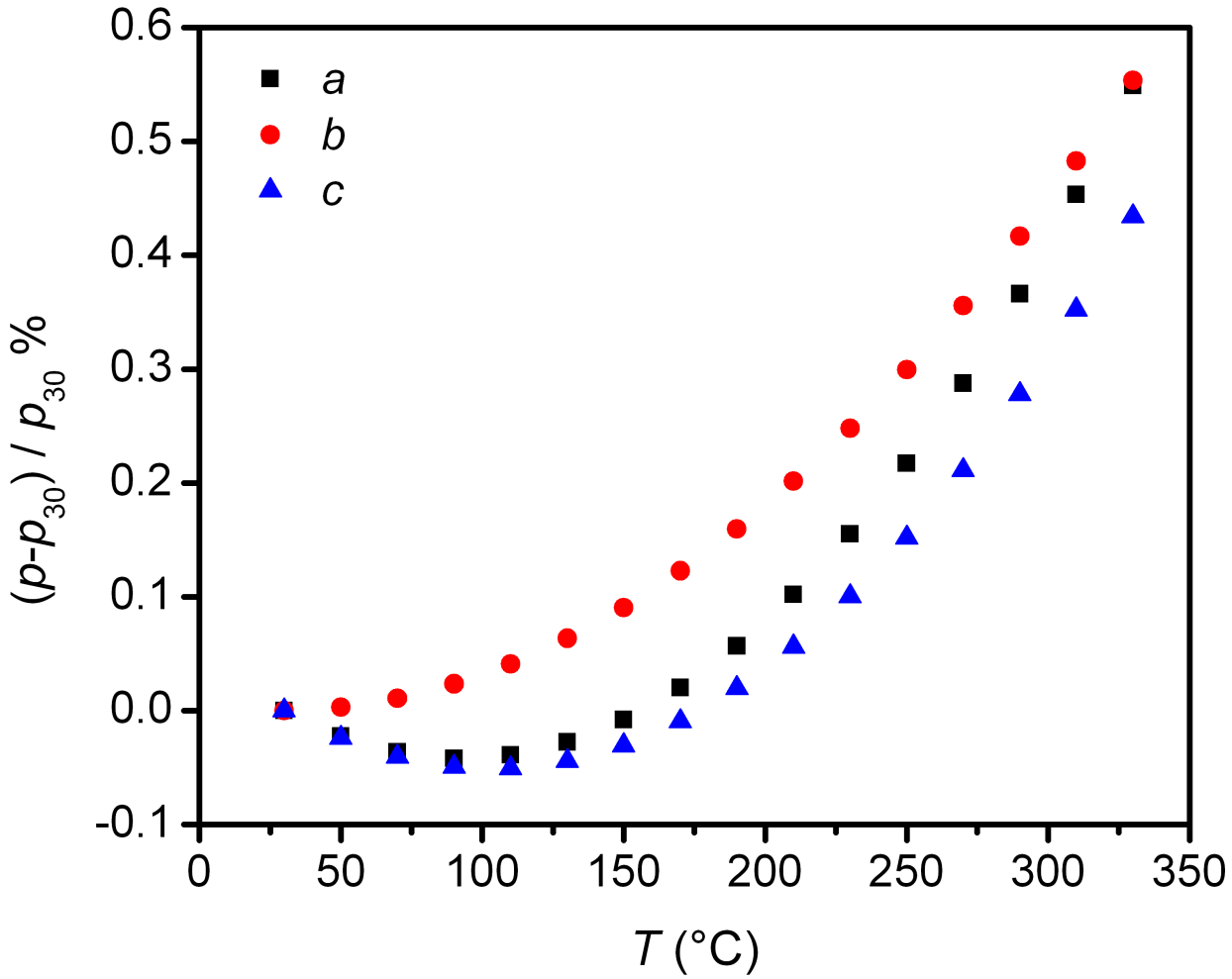

Figure S12. Variation in the unit cell parameters of $Fe_2(BDP)_3$ (p) normalized to the 30 °C values (p_{30}) as a function of temperature.

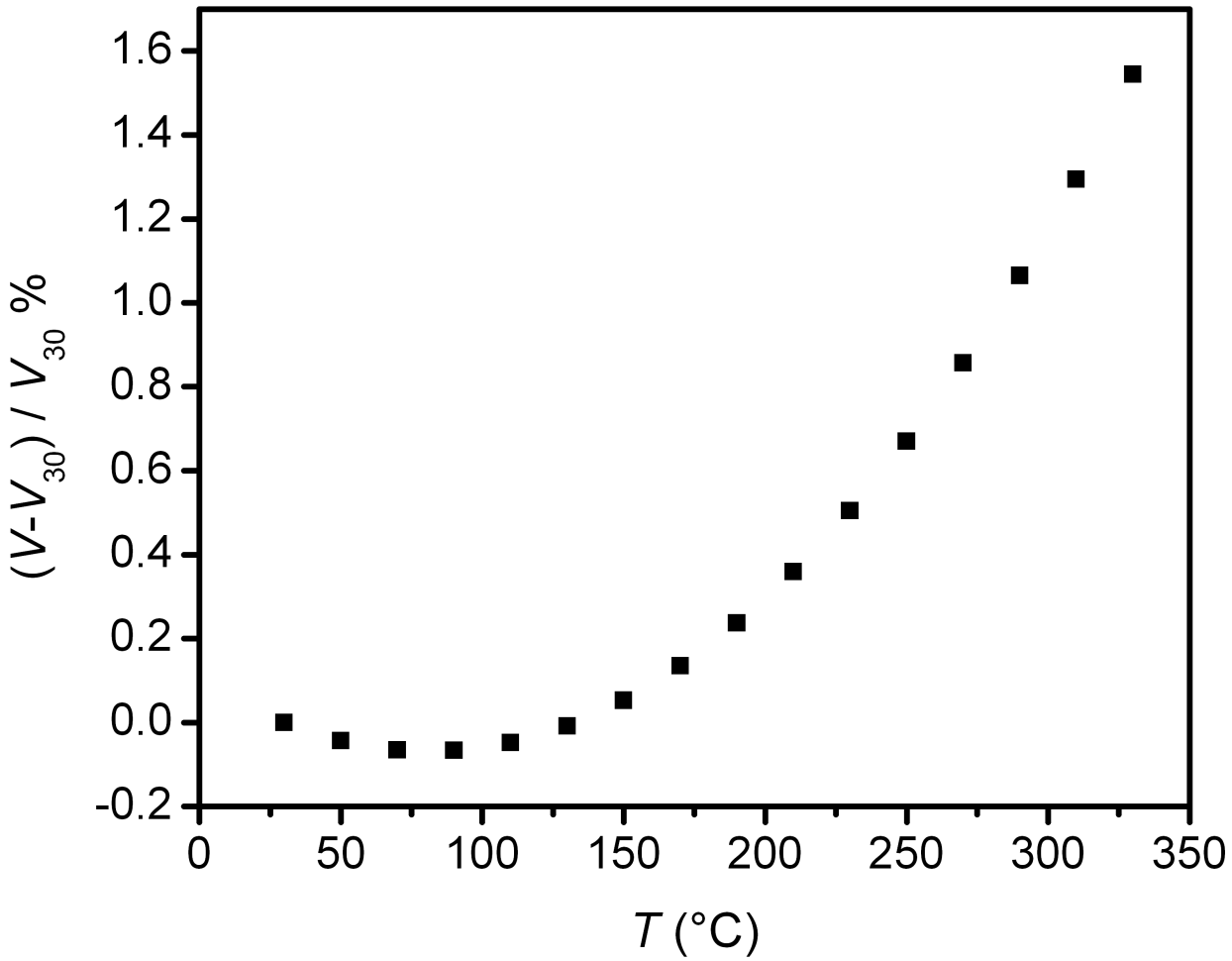

Figure S13. Variation in the unit cell volume of Fe_2BDP_3 (V) normalized to the 30 °C values (V_{30}) as a function of temperature.

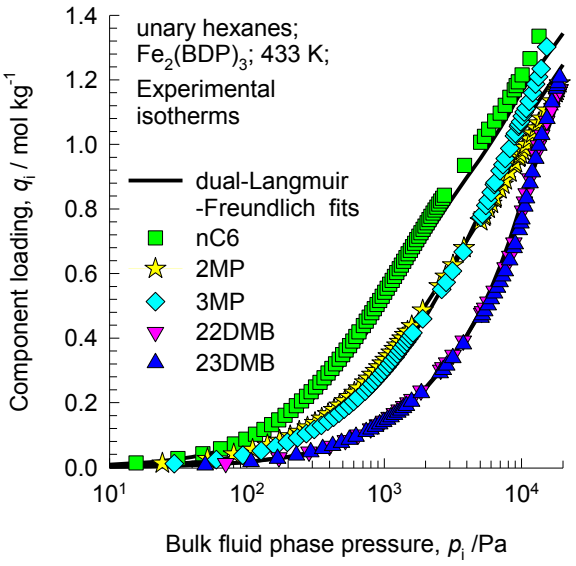

Figure S14. Pure component isotherms for nC6, 2MP, 3MP, 22DMB, and 23DMB in $Fe_2(BDP)_3$ at a temperature of 433 K. The continuous solid lines are the fits using the dual-site Langmuir-Freundlich isotherms.

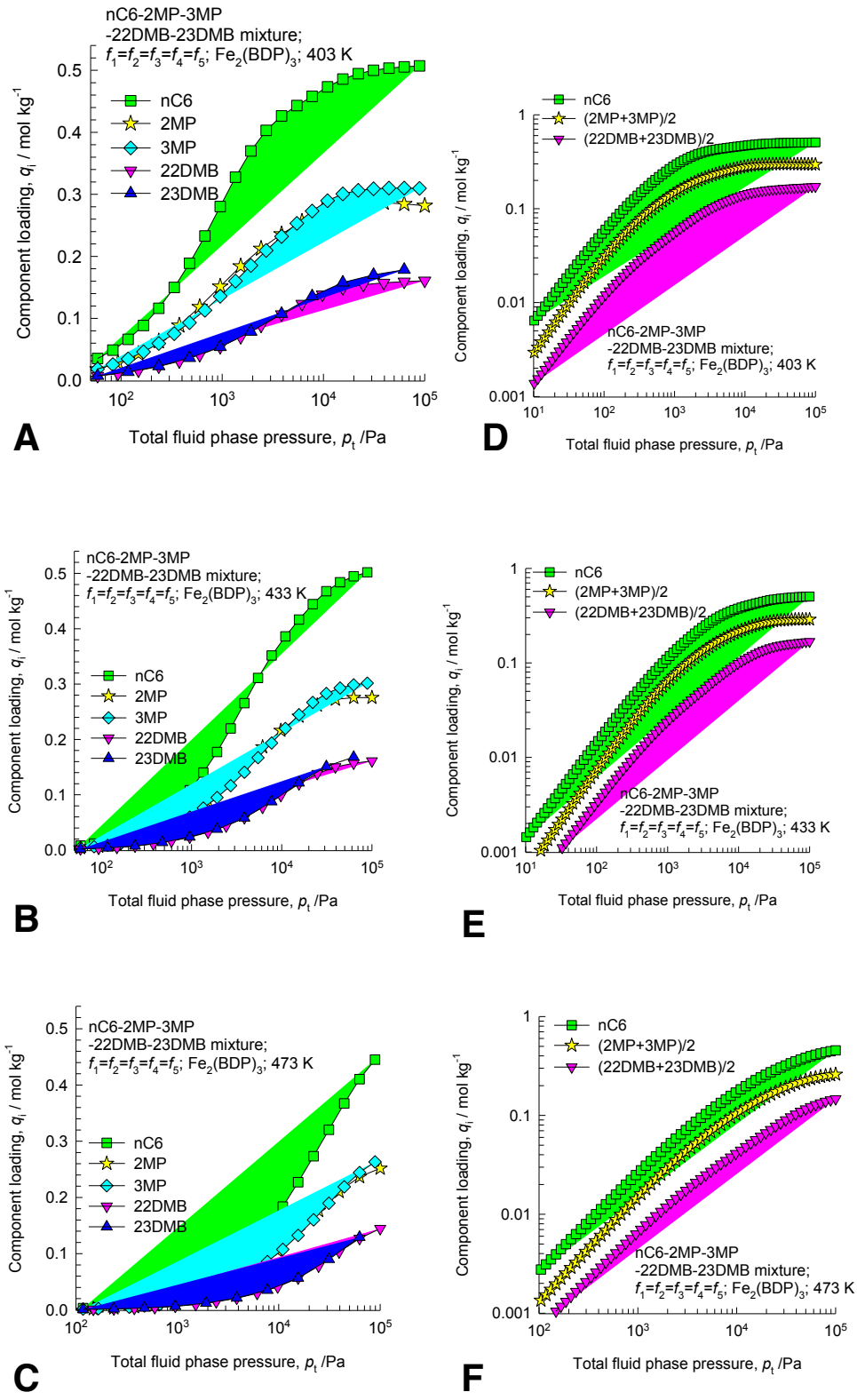

Figure S15. Calculations of component loadings for adsorption of 5-component nC6/2MP/3MP/22DMB/ 23DMB mixtures at 403 K, 433 K, and 473 K using Ideal Adsorbed Solution Theory. In these calculations, the partial pressures of the components in the bulk gas phase are $p_1 = p_2 = p_3 = p_4 = p_5$.

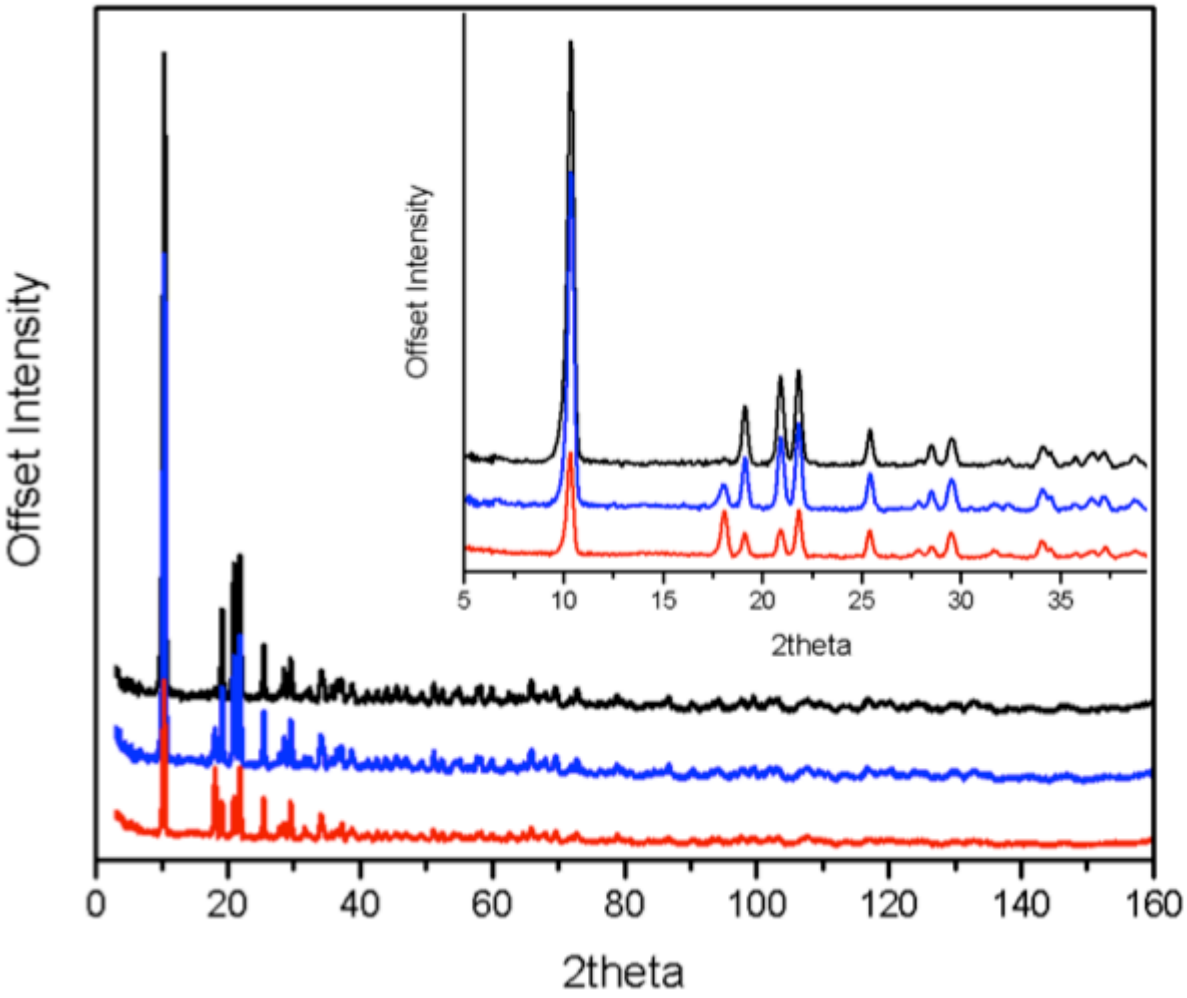

Figure S16. Neutron diffraction patterns collected at 10 K for the bare/activated $Fe_2(BDP)_3$ (black trace), hexane dosed/partially saturated $Fe_2(BDP)_3$ (blue trace), and the hexane dosed/saturated Fe (BD3P) (red trace).

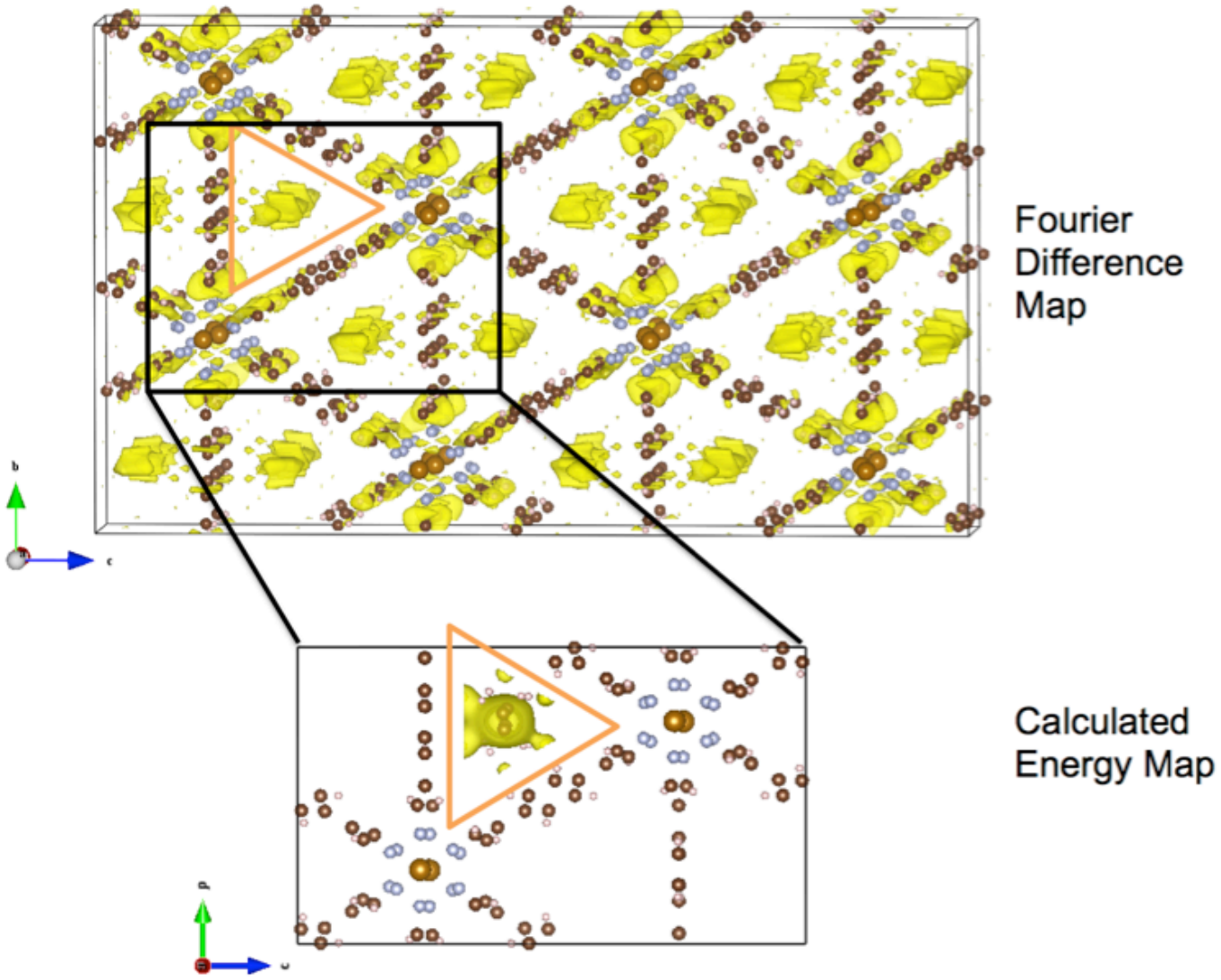

Figure S17. Upper: Fourier difference map for the partially solvated $Fe_2(BDP)_3$ sample showing the difference in scattering density (yellow) after accounting for the framework structure in the neutron powder refinement. Lower: Calculated energy minima from DFT calculations (yellow) on top of the lowest energy simulated *n*-hexane position in the center of the triangular pores. In each case, the *n*-hexane spans over a 2x1x1 cell since the hexane is too long to model in a 1x1x1 cell (a=7.1043Å).

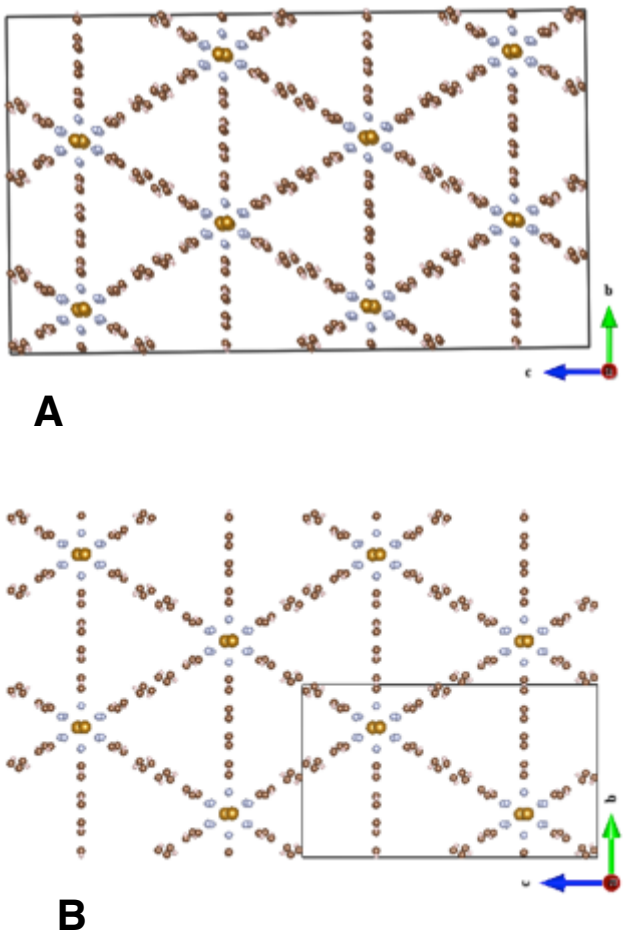

Figure S18. Crystal structure of high symmetry orthorhombic cell (**A**) and the Niggli reduced equivalent triclinic unit (**B**). In both cases the axis of pores is aligned with a-axis.

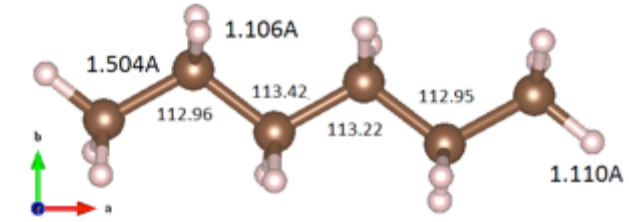

A

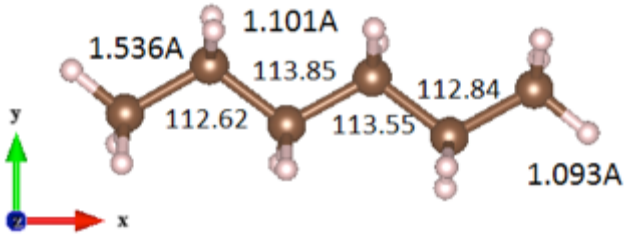

B

Figure S19. Structures of *n*-hexane obtained from relaxation using LDA (**A**) and van der Waals (**B**) potentials.

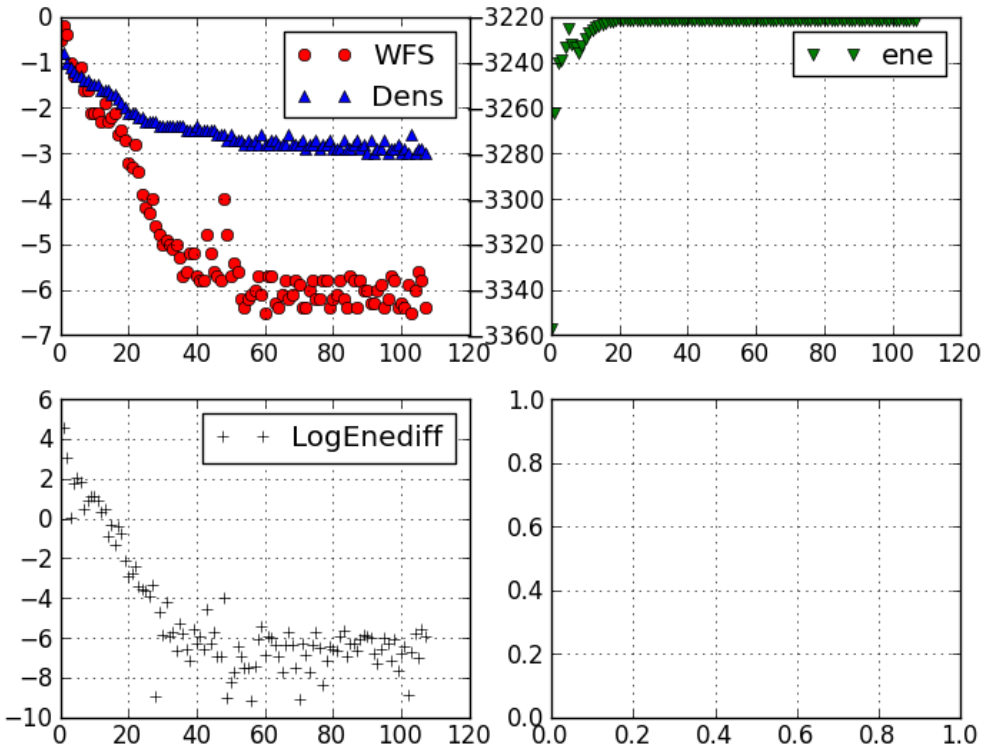

Figure S20. Parameters of the calculations vs. the iterations number from the first runs of doubled cell. The lack of convergence was caused by the variation of the residual density (Dens), which was high due to large volume of the system. The changes in other parameters like logarithm of the energy changes (LogEnediff) , Wannier functions (WFS) and the energy (ene) were converging quickly.

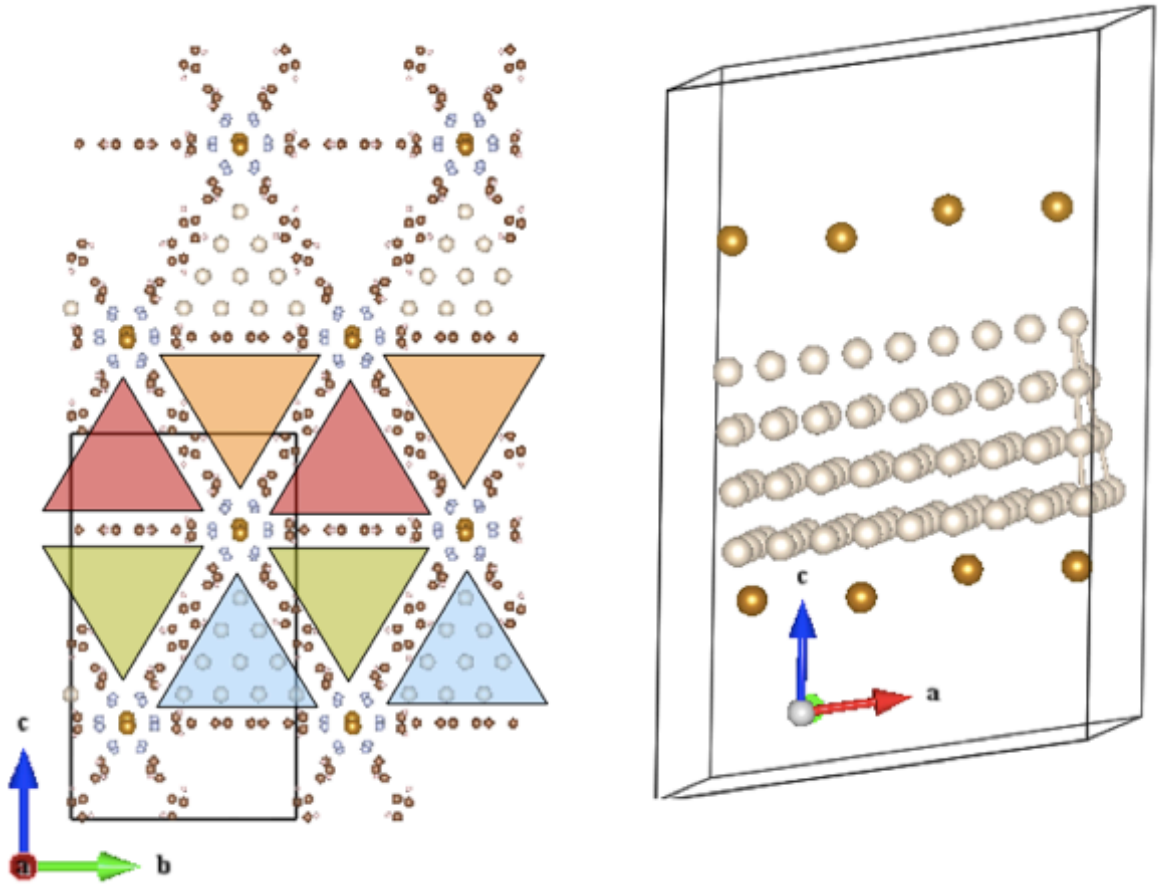

Figure S21. *N*-hexane insertion sites (marked with white atoms) in MOF were selected in one of the 4 possible pores (**A**) and the triangular platelets were distributed along the channel (**B**).

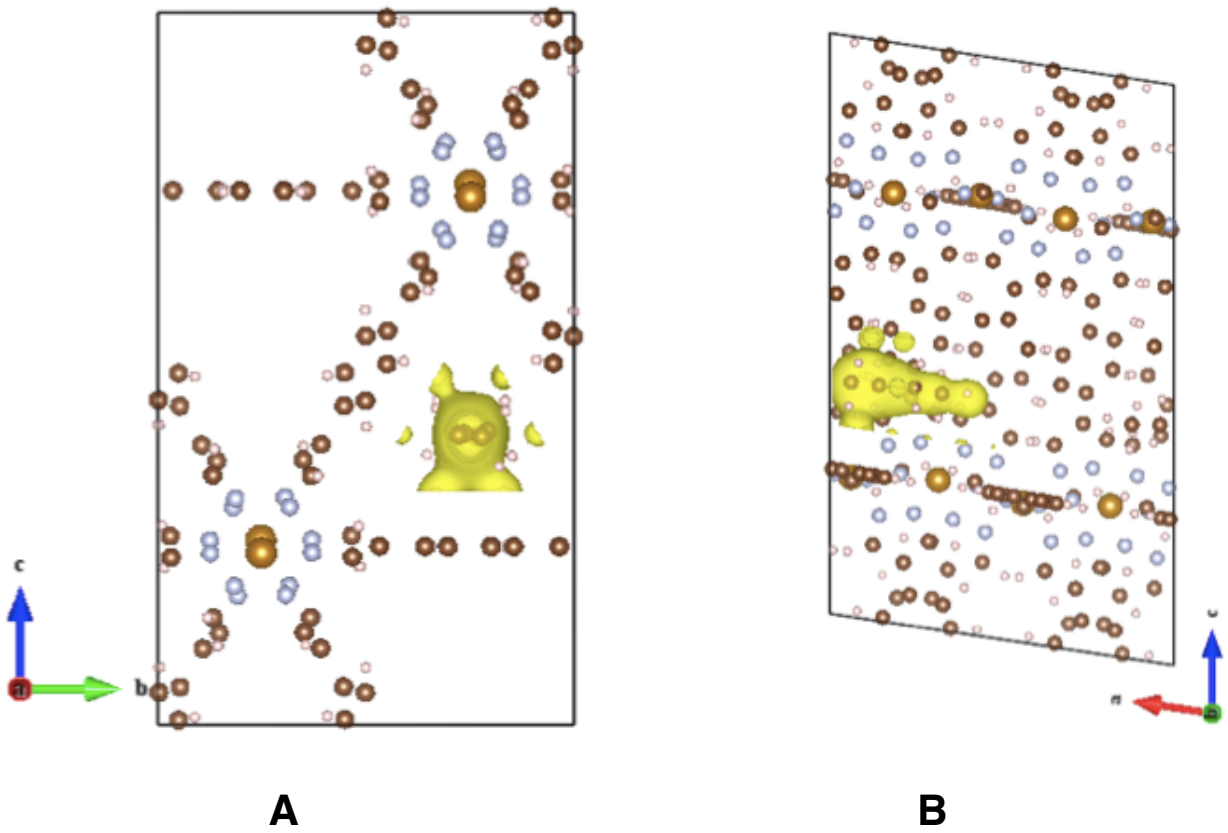

Figure S22. Isosurface of the insertion energy plotted at 35eV level together with hexane located in the lowest found position along a-axis (**A**) and b-axis (**B**).

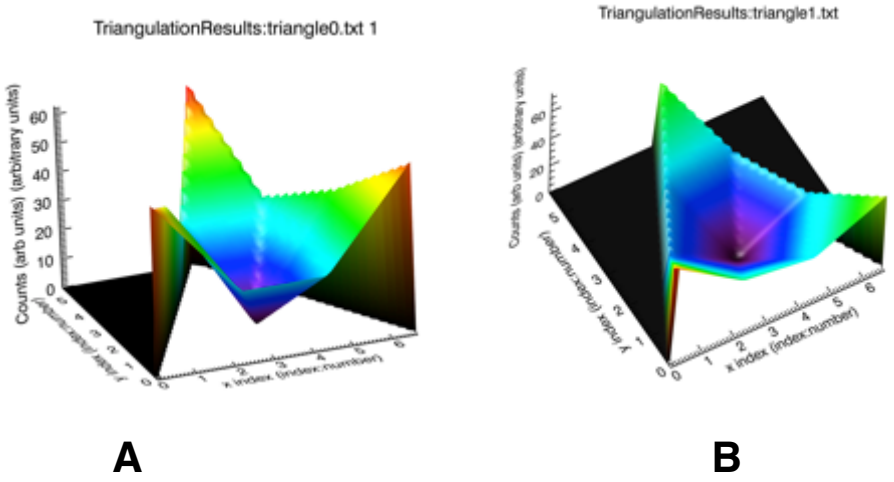

A B

Figure S23. Example of the energy profile of the two upper triangles. A clear minimum is visible in the center of the pore with lowest gradients toward pore walls and steep slopes pointing to the acute angles of the triangle.

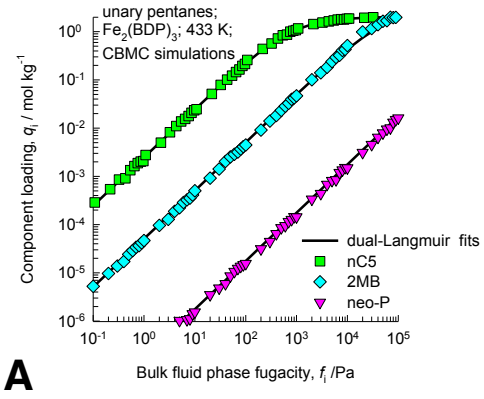

A

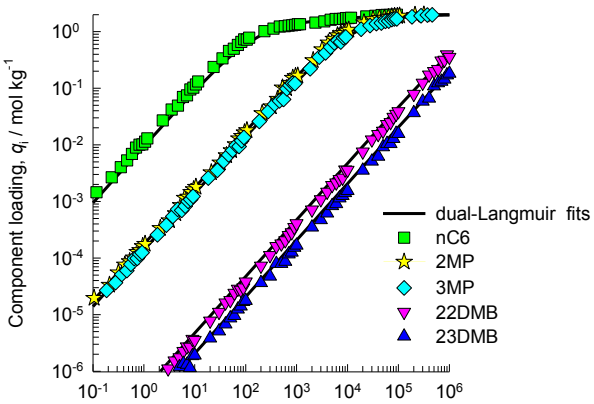

B

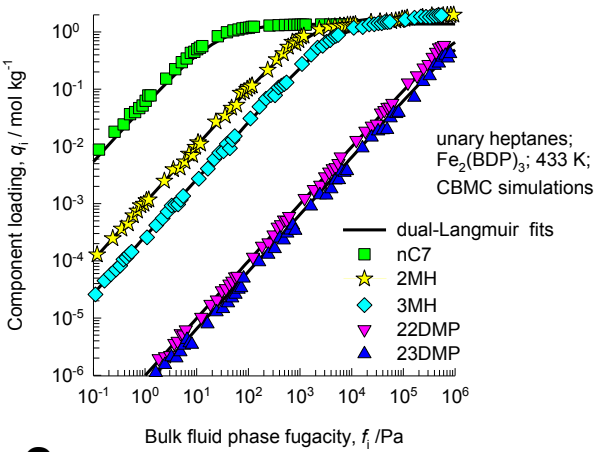

C

Figure S24. CBMC simulations of pure component isotherms for nC5, 2MB, neoP, nC6, 2MP, 3MP, 22DMB, 23DMB, nC7, 2MH, 3MH, 22DMP, and 23DMP in $Fe_2(BDP)_3$ at 433 K. Note that the x-axes indicate the fugacity, f_i, of the components in the gas phase.

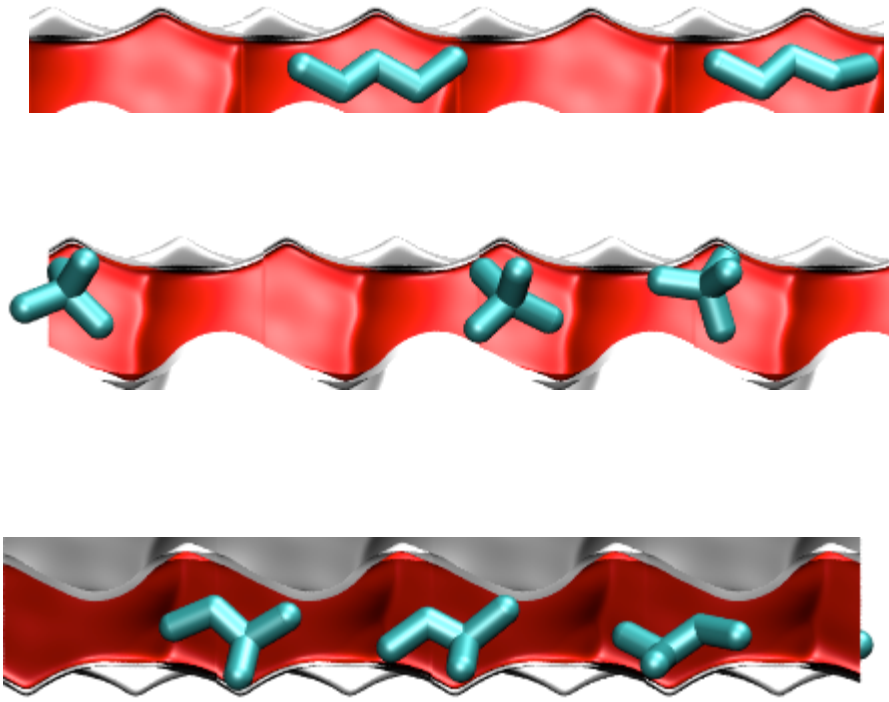

Figure S25. Snapshots, obtained from molecular simulations, showing the location and conformations of *n*-pentane (top), 2,2-dimethylpropane (middle), and 2-methylbutane (bottom) adsorbed within the triangular channels of $Fe_2(BDP)_3$.

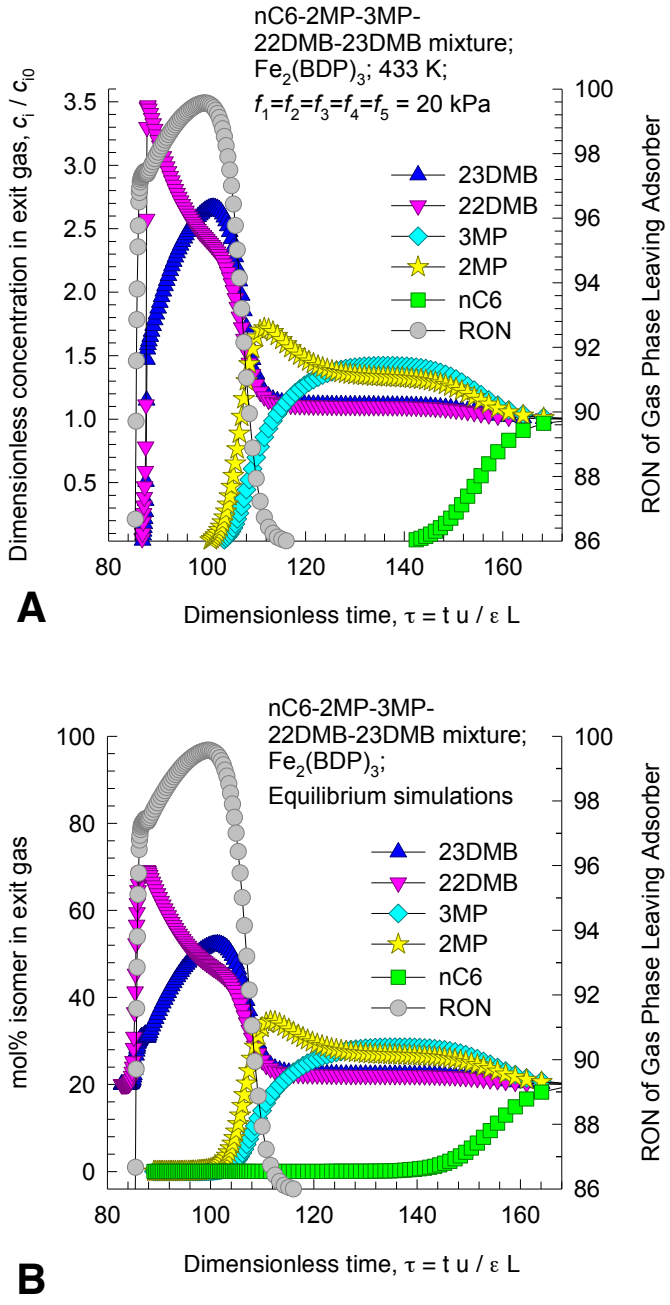

Figure S26. Simulations of breakthrough characteristics of a fixed bed adsorber packed with $Fe_2(BDP)_3$ operating at a total pressure of 100 kPa and 433 K. The partial pressures of the components in the bulk gas phase at the inlet are $p_1 = p_2 = p_3 = p_4 = p_5 = 20$ kPa. In these calculations, thermodynamic equilibrium prevails and diffusional influences are ignored. The two graphs present identical simulation data but the gas phase concentrations are plotted differently.

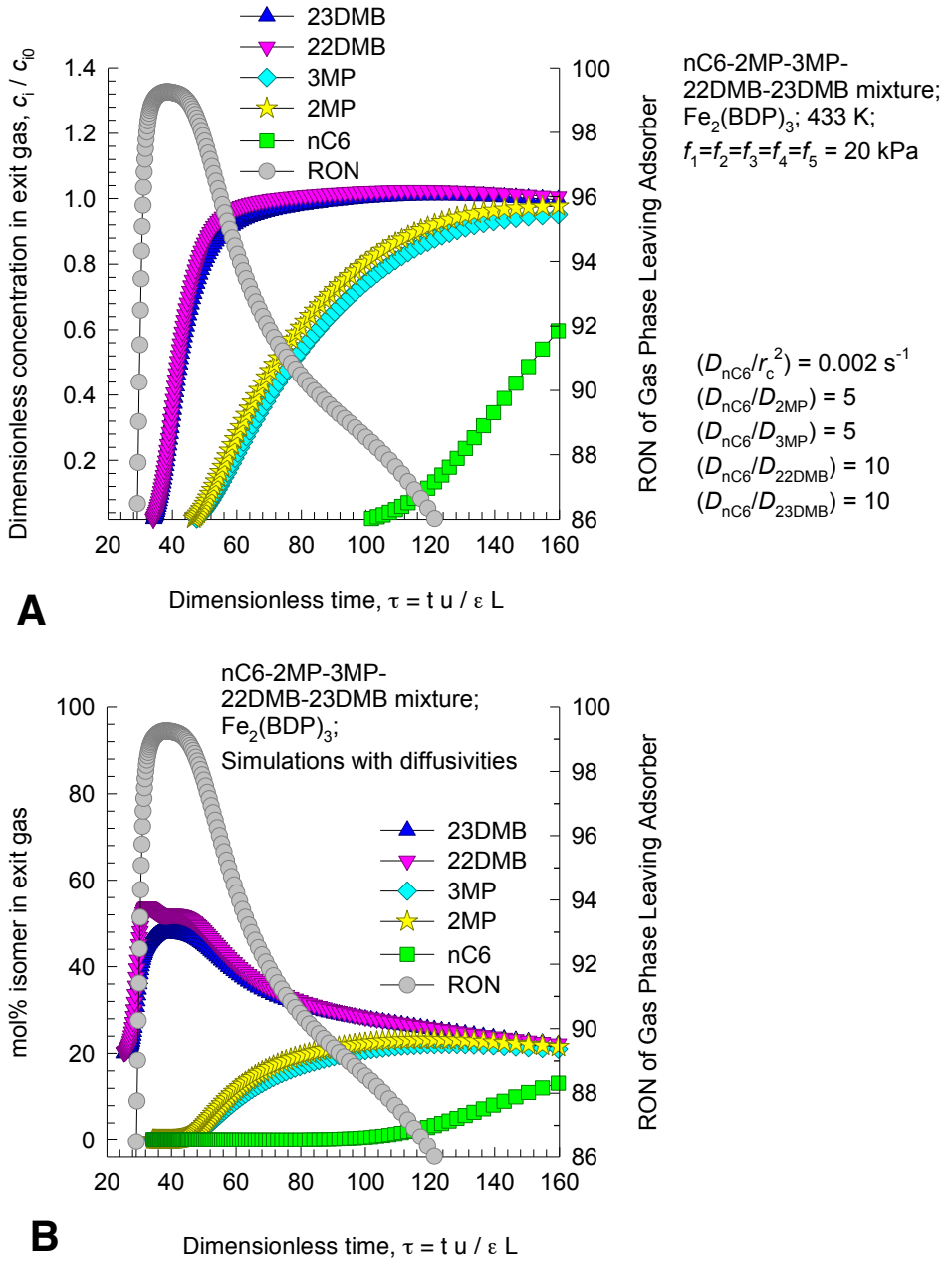

Figure S27. Simulations of breakthrough characteristics of a fixed bed adsorber packed with $Fe_2(BDP)_3$ operating at a total pressure of 100 kPa and 433 K. The partial pressures of the components in the bulk gas phase at the inlet are $p_1 = p_2 = p_3 = p_4 = p_5 = 20$ kPa. These simulations include diffusional effects with $D_{nC6}/r_c^2 = 0.002$ s^{-1}; D_{nC6}/D_{2MP} =5; D_{nC6}/D_{3MP} =5; D_{nC6}/D_{22DMB} =10; D_{nC6}/D_{23DMB} =10. The two graphs present identical simulation data but the gas phase concentrations are plotted differently.

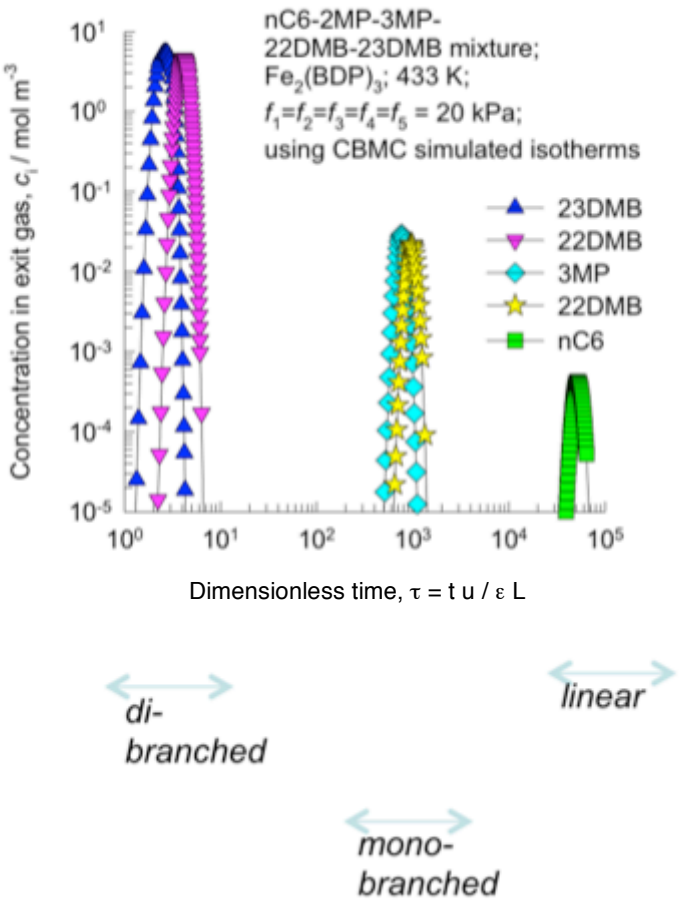

Figure S28. Pulse chromatographic simulations for separation of 5-component hexanes: nC6/2MP/3MP/22DMB/23DMB using $Fe_2(BDP)_3$. These simulations are carried out using pure component isotherm fits of CBMC simulations. No diffusional influences are accounted for in this case.

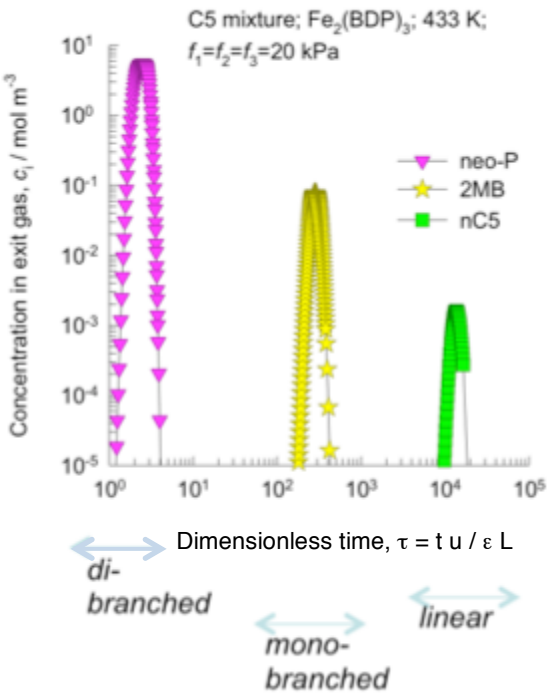

Figure S29. Pulse chromatographic simulations for separation of 3-component pentanes: nC5/2MB/neoP using $Fe_2(BDP)_3$. These simulations are carried out using pure component isotherm fits CBMC simulations of component isotherms. No diffusional influences are accounted for in this case.

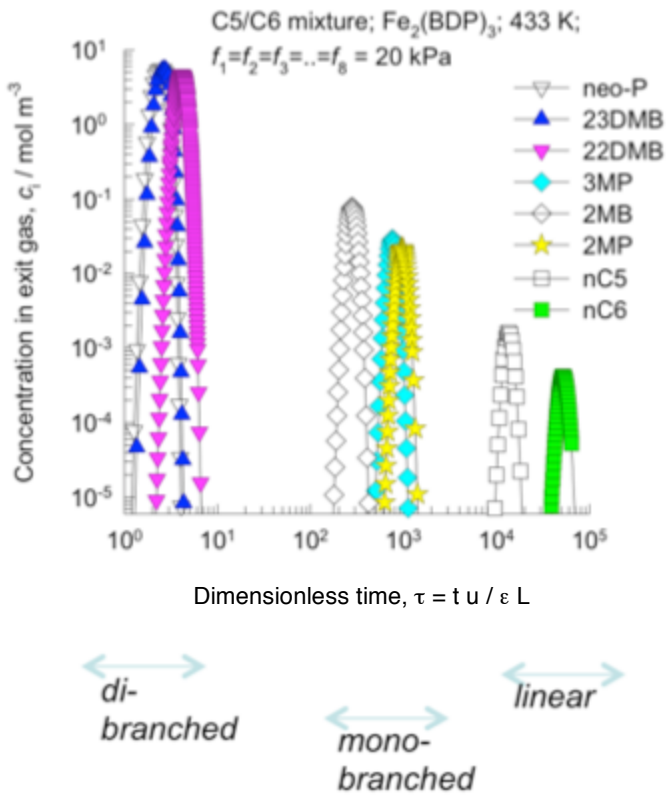

Figure S30. Pulse chromatographic simulations for separation of 8-component pentanes/hexanes: nC5/2MB/neoP/nC6/2MP/3MP/22DMB/23DMB using $Fe_2(BDP)_3$. These simulations are carried out using pure component isotherm fits of CBMC simulations. No diffusional influences are accounted for in this case.

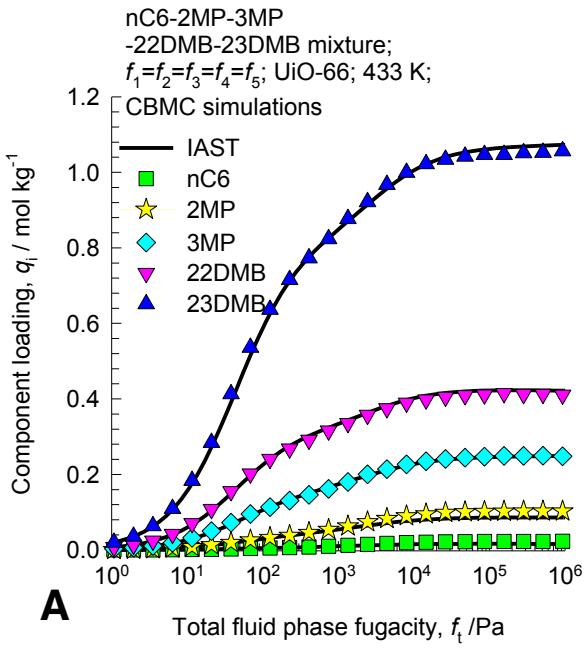

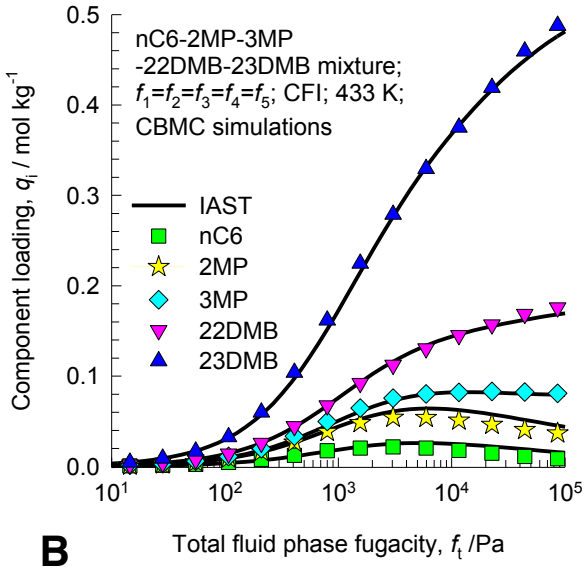

Figure S31. CBMC simulations of 5-component hexanes: nC6/2MP/3MP/22DMB/23DMB, at 433 K in (**A**) UiO-66, and (**B**) CFI.

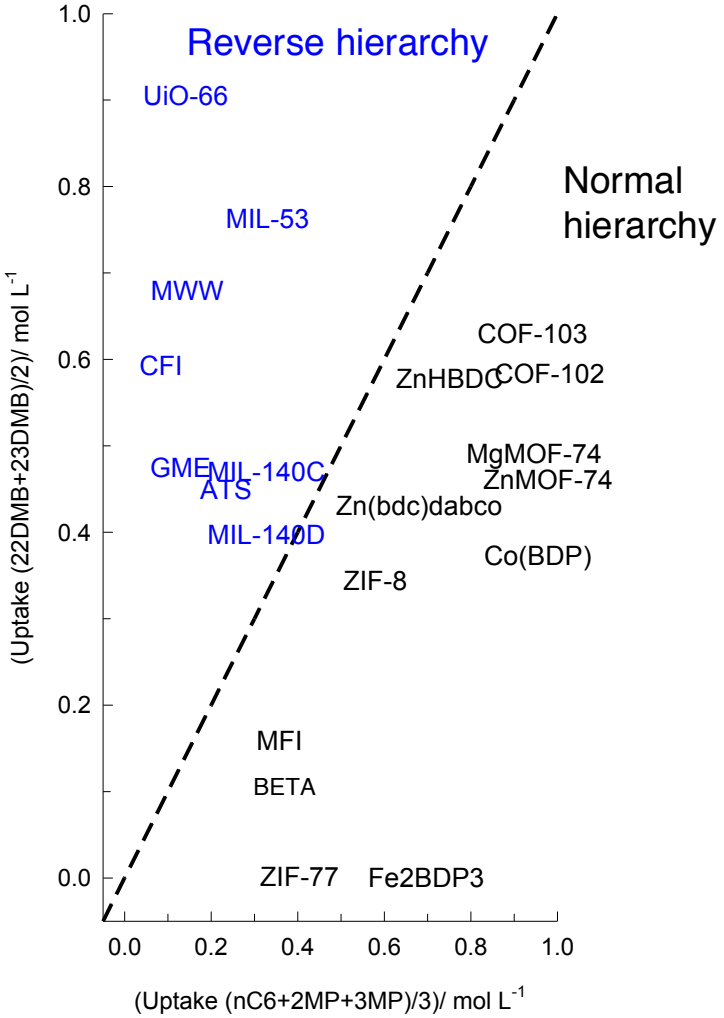

Figure S32. Plot of the two capacity metrics (nC6+2MP+3MP)/3 vs (22DMB+23DMB)/2 for different hosts. The materials with reverse or mixed hierarchies are indicated in blue.

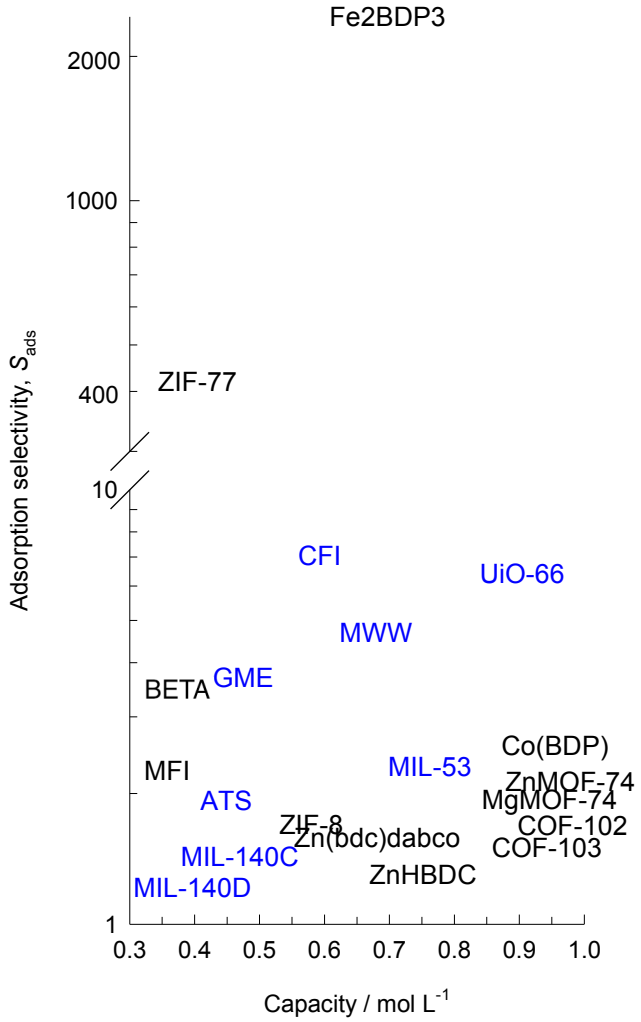

Figure S33. Comparison of adsorption selectivity versus capacity for separation of 5-component nC6/2MP/3MP/22DMB/23DMB mixtures at 433 K, with $f_1 = f_2 = f_3 = f_4 = f_5 = 20$ kPa, using a variety of materials. With the exception of $Fe_2(BDP)_3$, all the data plotted here are based on CBMC simulations. For a consistent comparison, we plot the CBMC simulation results for $Fe_2(BDP)_3$. For BETA, CBMC simulations are not in accord with experiments; in this case experimental isotherms are used.

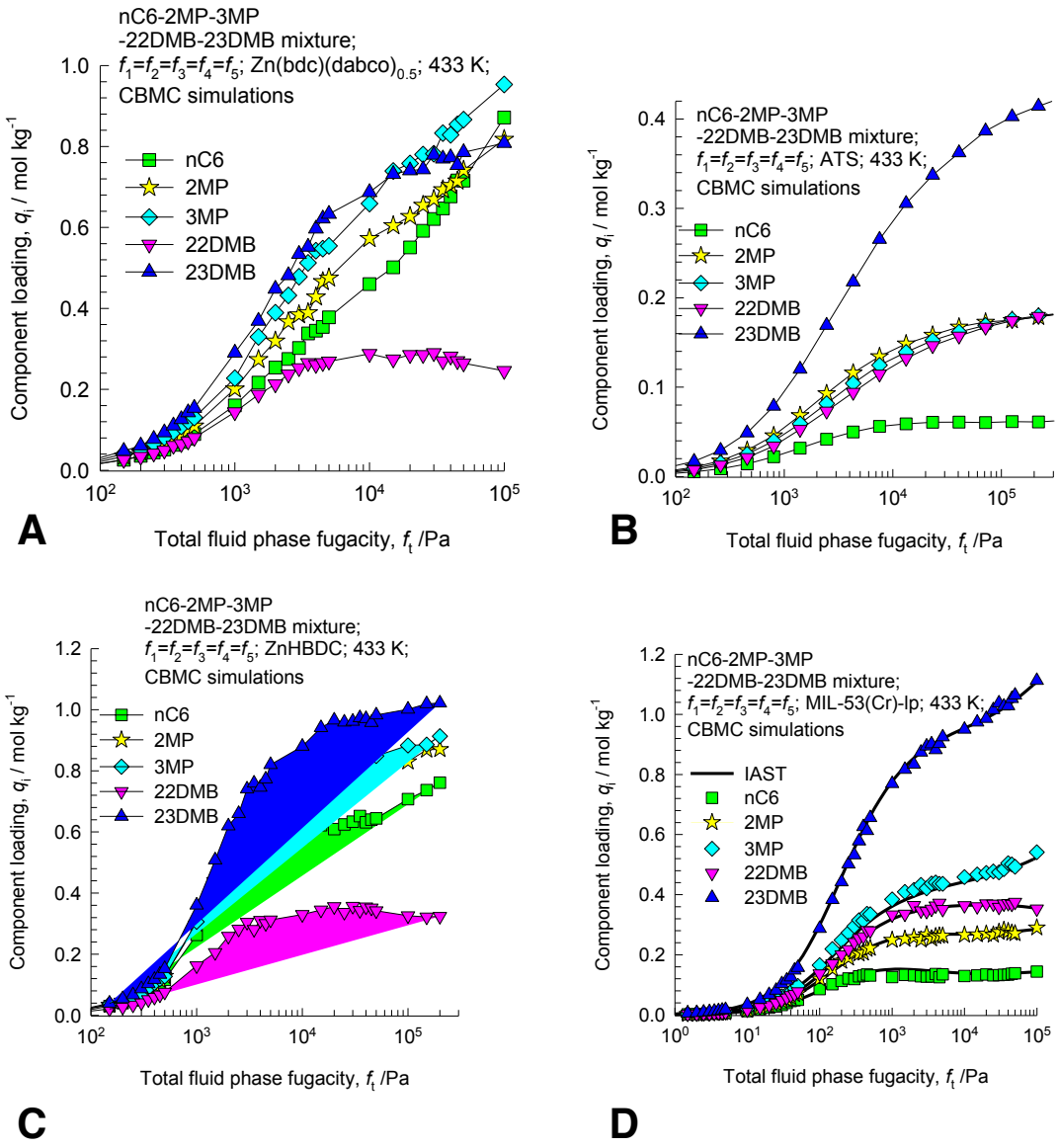

Figure S34. CBMC simulations of 5-component hexanes: nC6/2MP/3MP/22DMB/23DMB, at 433 K in (**A**) Zn(bdc)dabco, (**B**) ATS, (**C**) ZnHBDC, and (**D**) MIL-53(Cr)-lp.

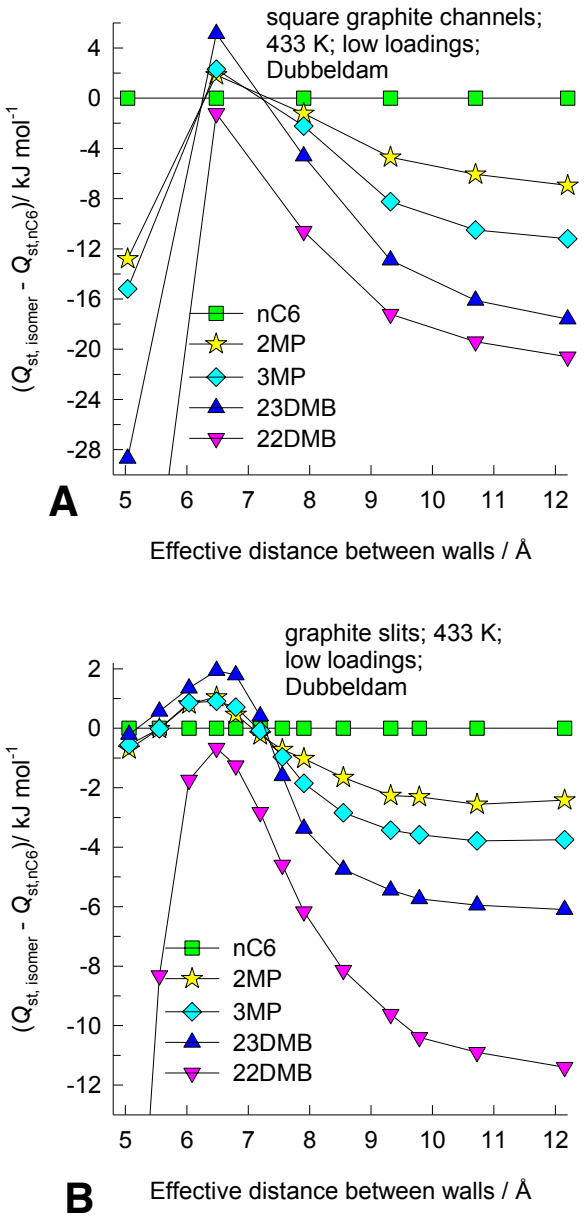

Figure S35. Isosteric heats of adsorption of hexane isomers, relative to that of nC6, in (**A**) square graphite channels, and (**B**) graphite slits of different effective channel spacings. The Q_{st} values are for at low loadings at 433 K.

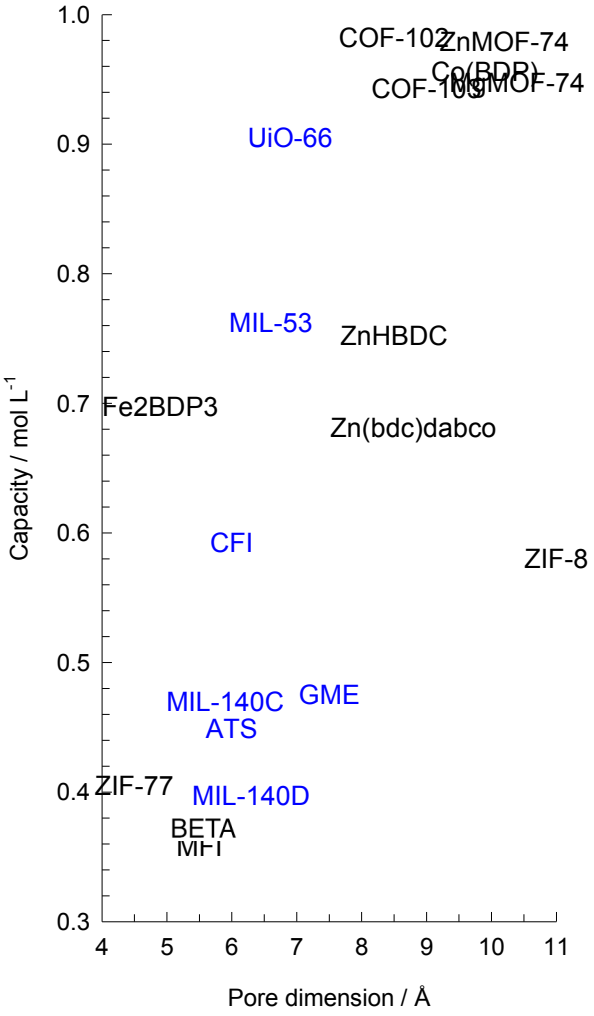

Figure S36. Capacity as a function of pore dimensions for different host materials. Materials with reverse and mixed hierarchies are indicated in blue.

Figure S37. Snapshots, obtained from molecular simulations, demonstrating that di-branched isomers have a shorter footprint within 1D channels of AFI

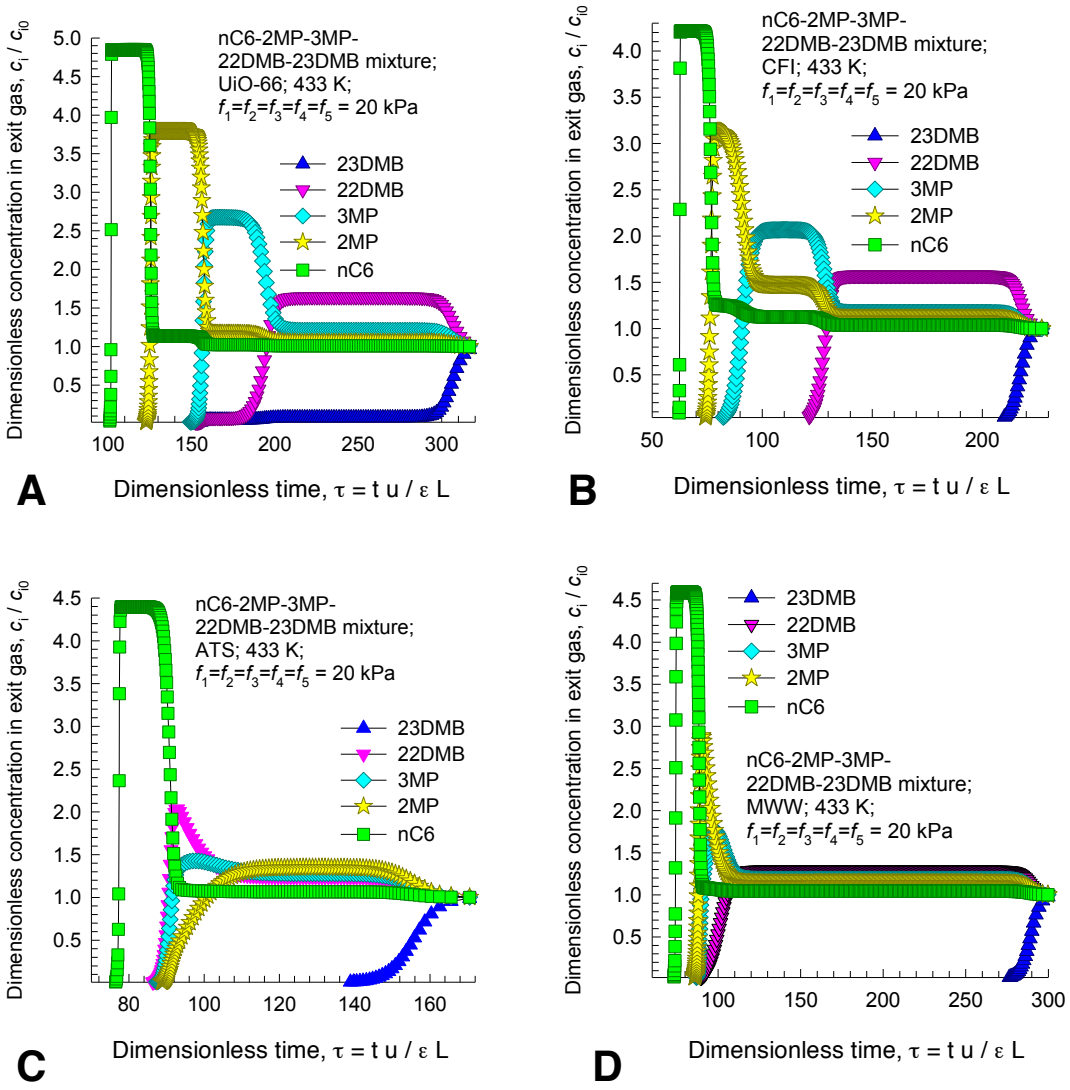

Figure S38. Simulations of breakthrough characteristics of a fixed bed adsorber packed with (a) UiO-66, (b) CFI, (c) ATS and (d) MWW, operating at a total pressure of 100 kPa and 433 K. The partial pressures of the components in the bulk gas phase at the inlet are $p_1 = p_2 = p_3 = p_4 = p_5 = 20$ kPa. In these calculations, thermodynamic equilibrium prevails and diffusional influences are ignored.

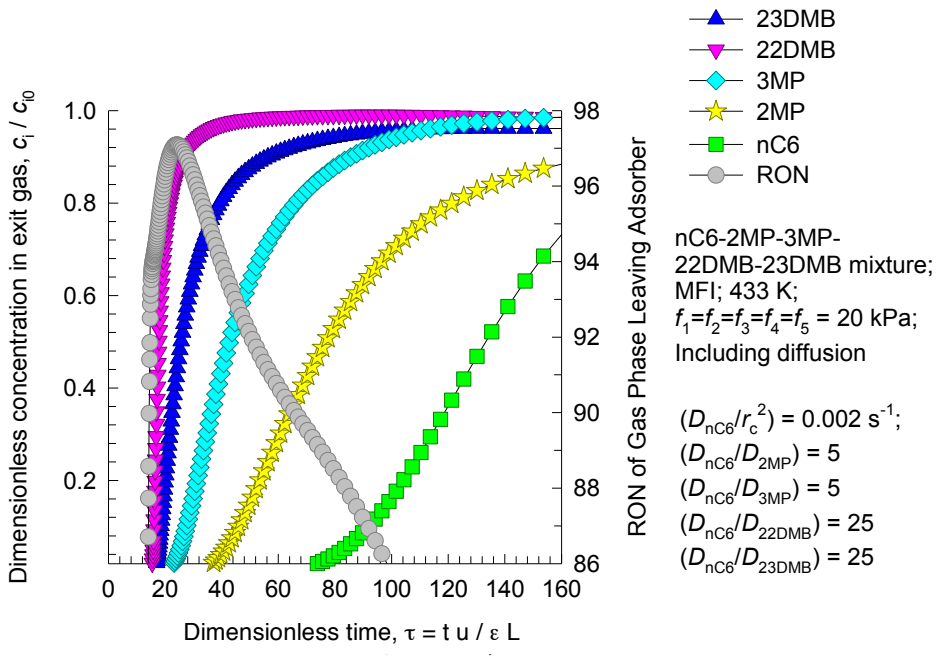

Figure S39. Simulations of breakthrough characteristics of a fixed bed adsorber packed with MFI operating at a total pressure of 100 kPa and 433 K. The partial pressures of the components in the bulk gas phase at the inlet are $p_1 = p_2 = p_3 = p_4 = p_5 = 20$ kPa. These simulations include diffusional effects with $D_{nC6}/r_c^2 = 0.002$ s^{-1}; D_{nC6}/D_{2MP} =5; D_{nC6}/D_{3MP} =5; D_{nC6}/D_{22DMB} =25; D_{nC6}/D_{23DMB} =25. The values of the diffusivities are chosen to be higher than those in $Fe_2(BDP)_3$, reflecting the larger channel dimensions of 5.5 Å.

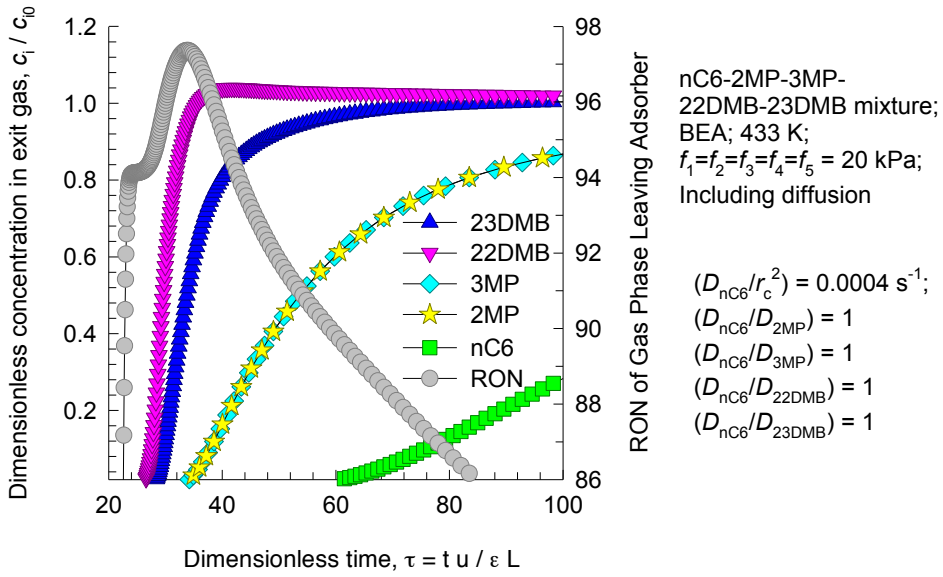

Figure S40. Simulations of breakthrough characteristics of a fixed bed adsorber packed with BETA operating at a total pressure of 100 kPa and 453 K. The partial pressures of the components in the bulk gas phase at the inlet are $p_1 = p_2 = p_3 = p_4 = p_5 = 20$ kPa. These simulations include diffusional effects with $D_{nC6}/r_c^2 = 0.0004$ s^{-1}; D_{nC6}/D_{2MP} =1; D_{nC6}/D_{3MP} =1; D_{nC6}/D_{22DMB} =1; D_{nC6}/D_{23DMB} =1. The isotherm data used in the IAST calculations are obtained by re-fitting the reported experimental isotherm data. The data is not available for 2MP, so the 5-component simulations were performed assuming that the isotherms for 2MP and 3MP are identical. In view of this assumption the breakthrough characteristics of 2MP and 3MP are identical.

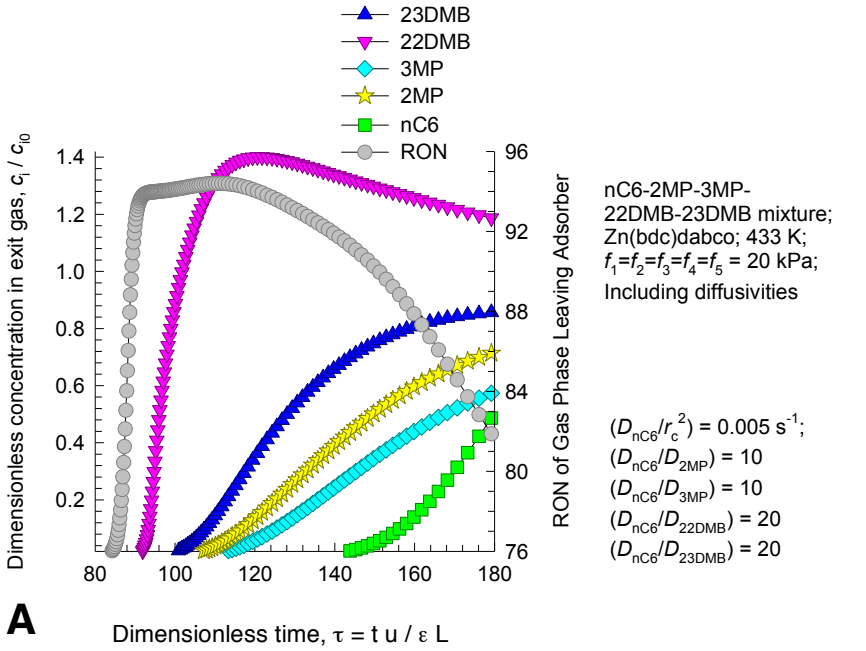

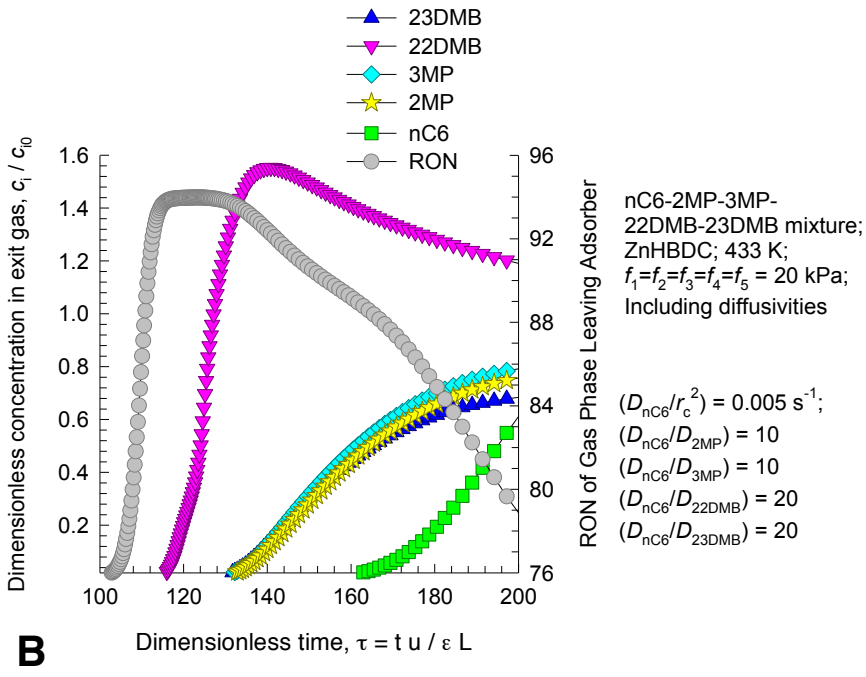

Figure S41. Simulations of breakthrough characteristics of a fixed bed adsorber packed with (**A**) Zn(bdc)dabco, and (**B**) ZnHBDC operating at a total pressure of 100 kPa and 433 K. The partial pressures of the components in the bulk gas phase at the inlet are $p_1 = p_2 = p_3 = p_4 = p_5 = 20$ kPa. These simulations include diffusional effects with $D_{nC6}/r_c^2 = 0.005$ s^{-1}; $D_{nC6}/D_{2MP} = 10$; $D_{nC6}/D_{3MP} = 10$; $D_{nC6}/D_{22DMB} = 20$; $D_{nC6}/D_{23DMB} = 20$.

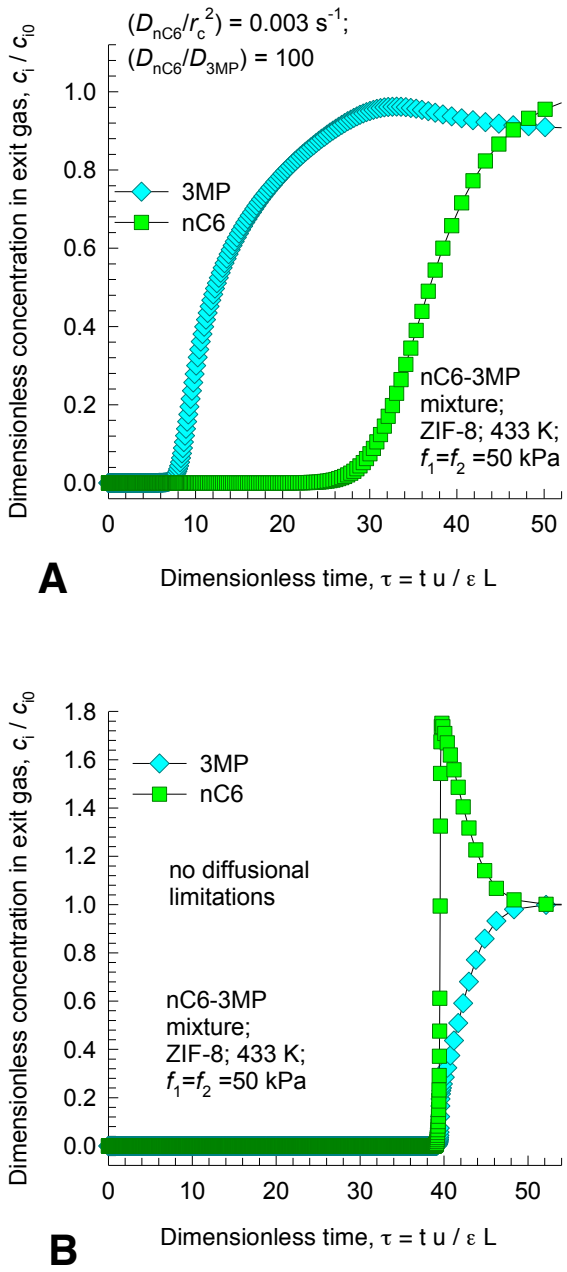

Figure S42. Breakthrough simulations for nC6/3MP mixture using ZIF-8 adsorbent (**A**) with inclusion of diffusional influences and (**B**) assuming thermodynamic equilibrium.

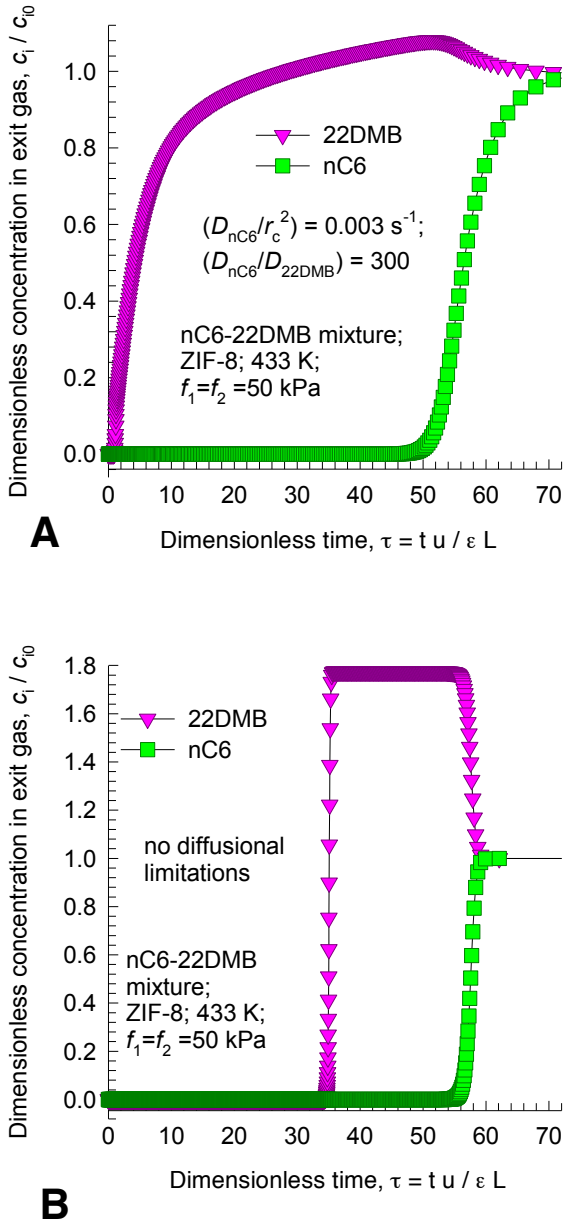

Figure S43. Breakthrough simulations for nC6/22DMB mixture using ZIF-8 adsorbent (**A**) with inclusion of diffusional influences and (**B**) assuming thermodynamic equilibrium.

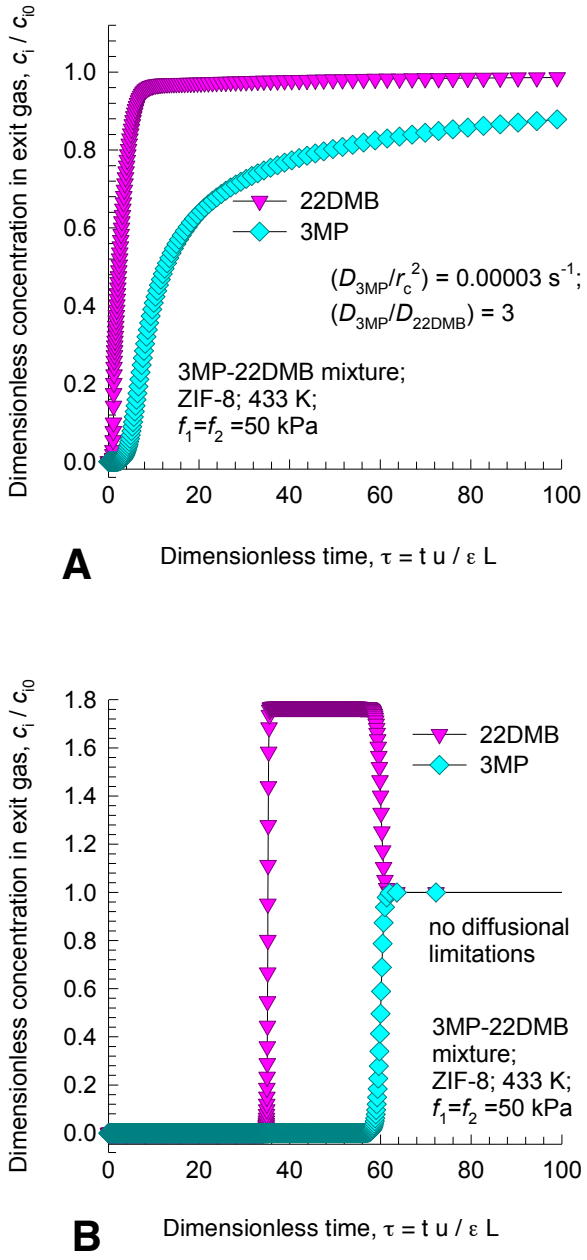

Figure S44. Breakthrough simulations for 3MP/22DMB mixture using ZIF-8 adsorbent (**A**) with inclusion of diffusional influences and (**B**) assuming thermodynamic equilibrium.

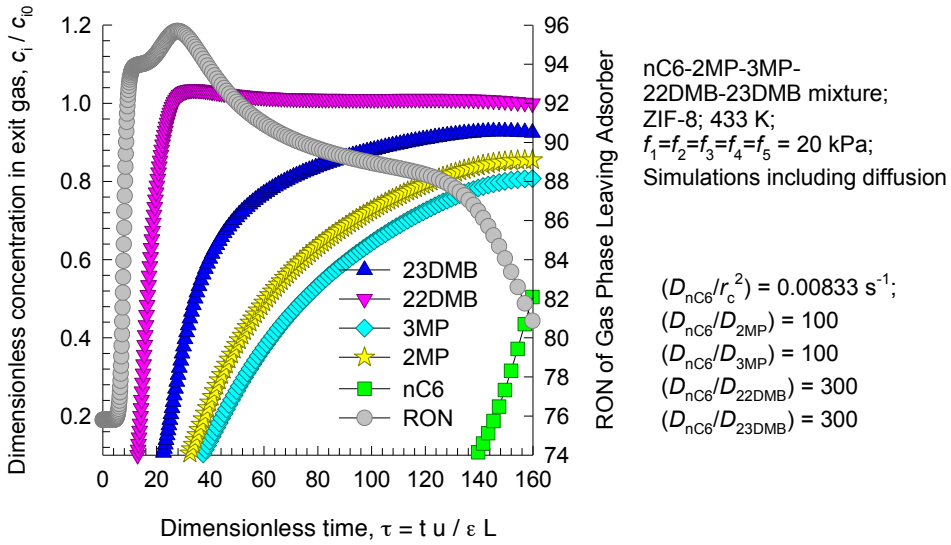

Figure S45. Simulations of breakthrough characteristics of a fixed bed adsorber packed with ZIF-8 operating at a total pressure of 100 kPa and 433 K. The partial pressures of the components in the bulk gas phase at the inlet are $p_1 = p_2 = p_3 = p_4 = p_5 = 20$ kPa. In these calculations, diffusional influences are included. The pure component isotherms, along with fit parameters, are from CBMC simulations.

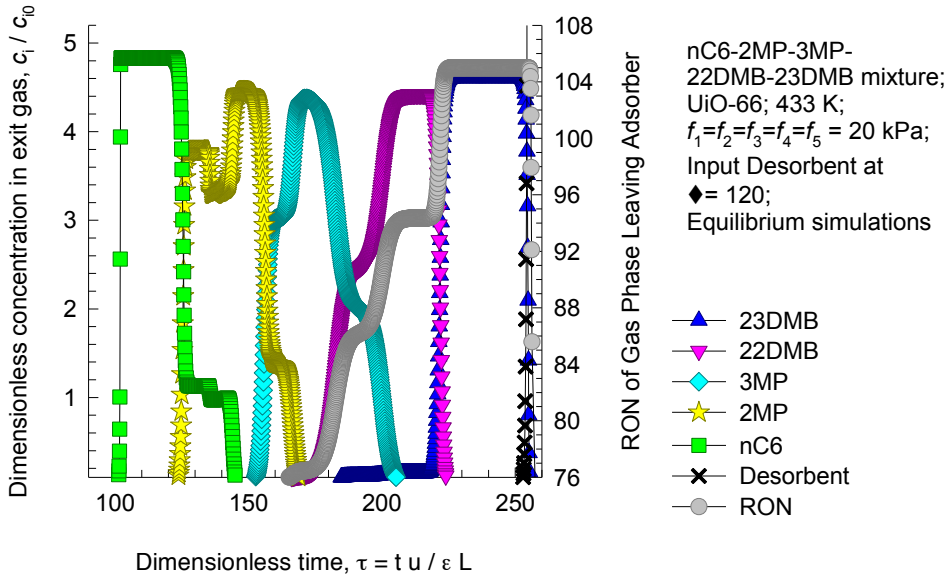

Figure S46. Adsorption/desorption cycles for UiO-66, operating at a total pressure of 100 kPa and 433 K. The partial pressures of the components in the bulk gas phase at the inlet are $p_1 = p_2 = p_3 = p_4 = p_5 = 20$ kPa. At $\tau = 120$, the desorbent is introduced, and the hexanes feed is stopped. These calculations are based on thermodynamic equilibrium. The pure component isotherms, along with fit parameters, are from CBMC simulations.

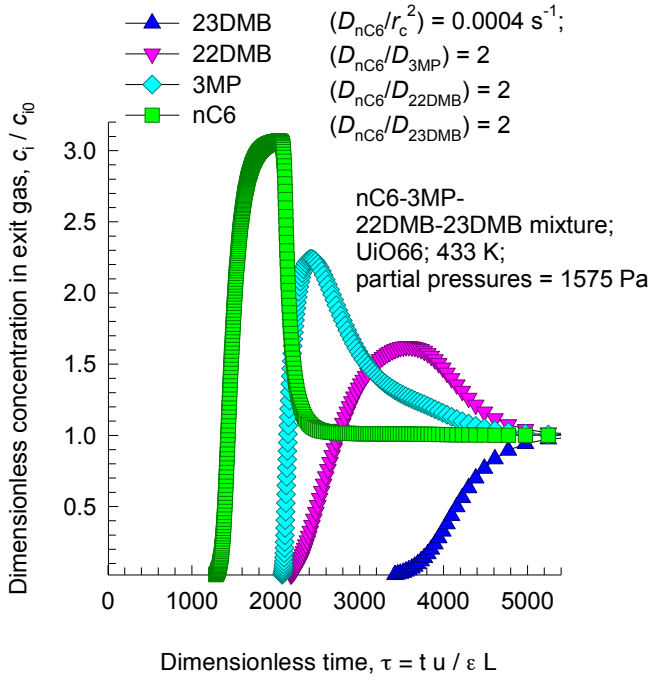

Figure S47. Breakthrough simulations of UiO-66 at 433 K using the pure component isotherms, along with fit parameters, from CBMC. These simulations include diffusional effects with $D_{nC6}/r_c^2 = 0.0004$ s^{-1}; $D_{nC6}/D_{3MP} = 2$; $D_{nC6}/D_{22DMB} = 2$; $D_{nC6}/D_{23DMB} = 2$.

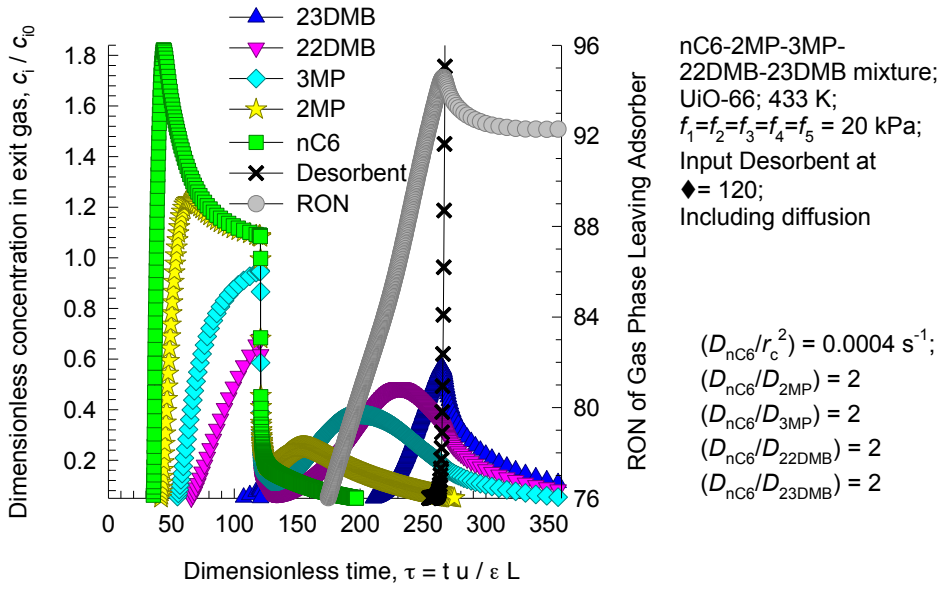

Figure S48. Adsorption/desorption cycles for UiO-66, operating at a total pressure of 100 kPa and 433 K. The pure component isotherms, along with fit parameters, are from CBMC simulations. These simulations include diffusional effects with D_{nC6}/r_c^2 = 0.0004 s^{-1}; D_{nC6}/D_{2MP} =2; D_{nC6}/D_{3MP} =2; D_{nC6}/D_{22DMB} =2; D_{nC6}/D_{23DMB} =2.

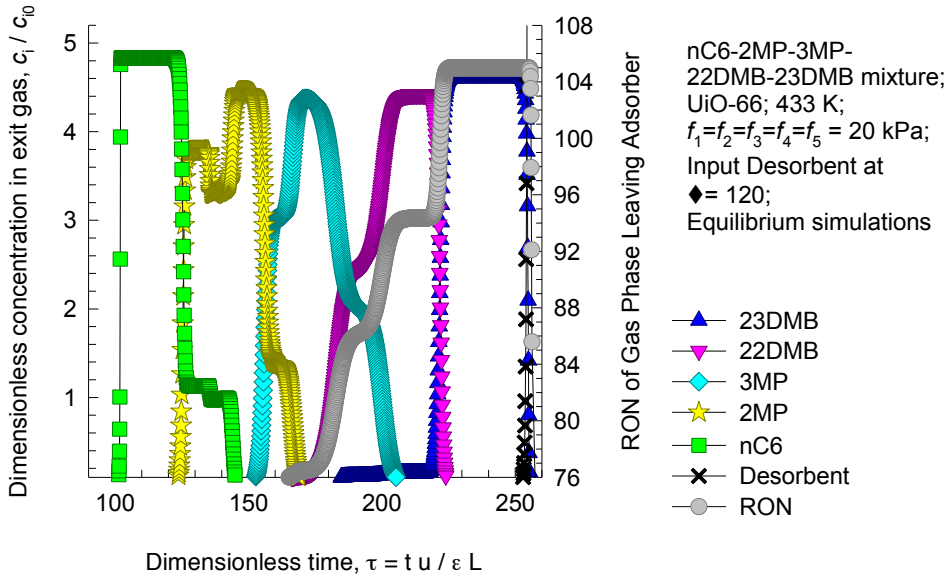

Figure S49. Adsorption/desorption cycles for MWW, operating at a total pressure of 100 kPa and 433 K. The partial pressures of the components in the bulk gas phase at the inlet are $p_1 = p_2 = p_3 = p_4 = p_5 = 20$ kPa. At $\tau = 120$, the desorbent is introduced, and the hexanes feed is stopped. These calculations are based on thermodynamic equilibrium. The pure component isotherms, along with fit parameters, are from CBMC simulations.

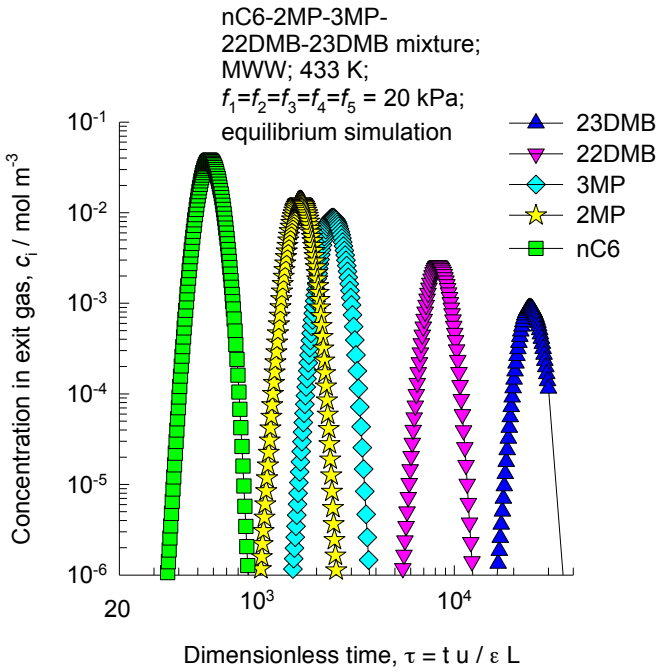

Figure S50. Pulse chromatographic simulations for separation of hexane isomers with MWW at 433 K.

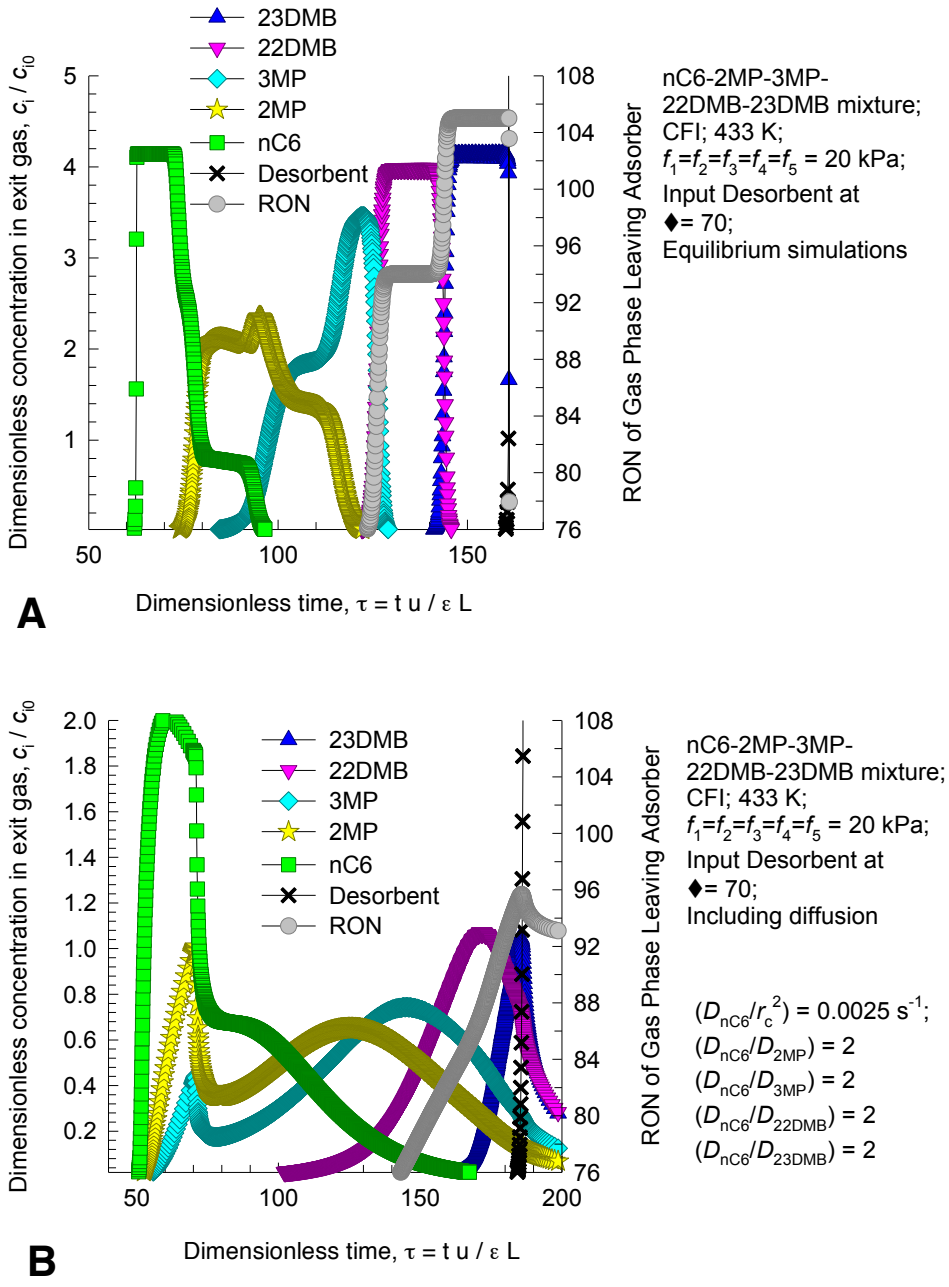

Figure S51. Adsorption/desorption cycles for CFI zeolite, operating at a total pressure of 100 kPa and 433 K. The partial pressures of the components in the bulk gas phase at the inlet are $p_1 = p_2 = p_3 = p_4 = p_5 = 20$ kPa. At $\tau = 70$, the desorbent is introduced, and the hexanes feed is stopped. In (**A**) thermodynamic equilibrium is assumed. In (**B**) the simulations include diffusional effects with $D_{nC6}/r_c^2 = 0.0025\ s^{-1}$; D_{nC6}/D_{2MP} =2; D_{nC6}/D_{3MP} =2; D_{nC6}/D_{22DMB} =2; D_{nC6}/D_{23DMB} =2. The pure component isotherms, along with fit parameters, are from CBMC simulations.

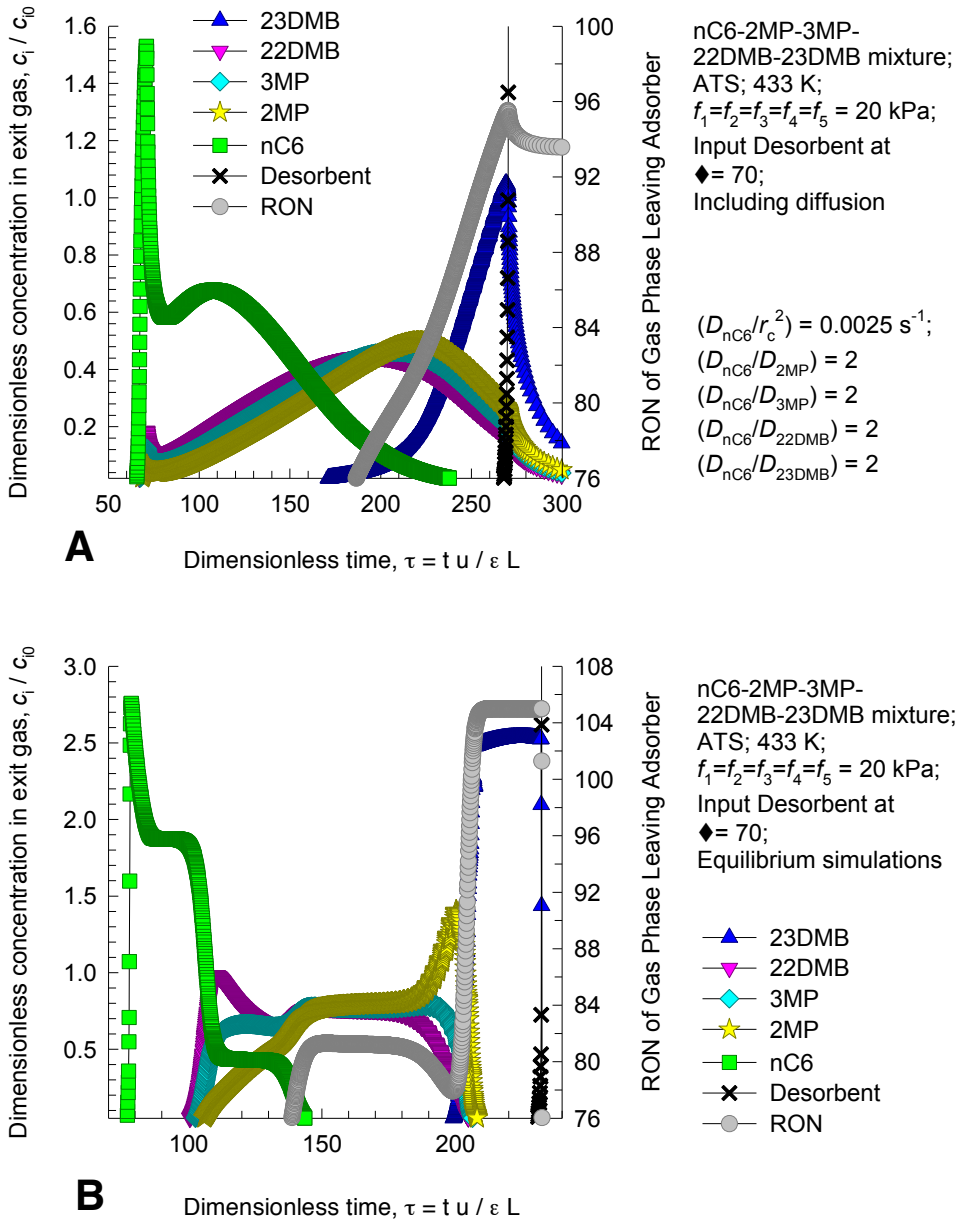

Figure S52. Adsorption/desorption cycles for ATS zeolite, operating at a total pressure of 100 kPa and 433 K. The partial pressures of the components in the bulk gas phase at the inlet are $p_1 = p_2 = p_3 = p_4 = p_5 = 20$ kPa. At $\tau = 70$, the desorbent is introduced, and the hexanes feed is stopped. In (**A**) the simulations include diffusional effects with $D_{nC6}/r_c^2 = 0.0025$ s^{-1}; D_{nC6}/D_{2MP} =2; D_{nC6}/D_{3MP} =2; D_{nC6}/D_{22DMB} =2; D_{nC6}/D_{23DMB} =2. In (**B**) thermodynamic equilibrium is assumed.

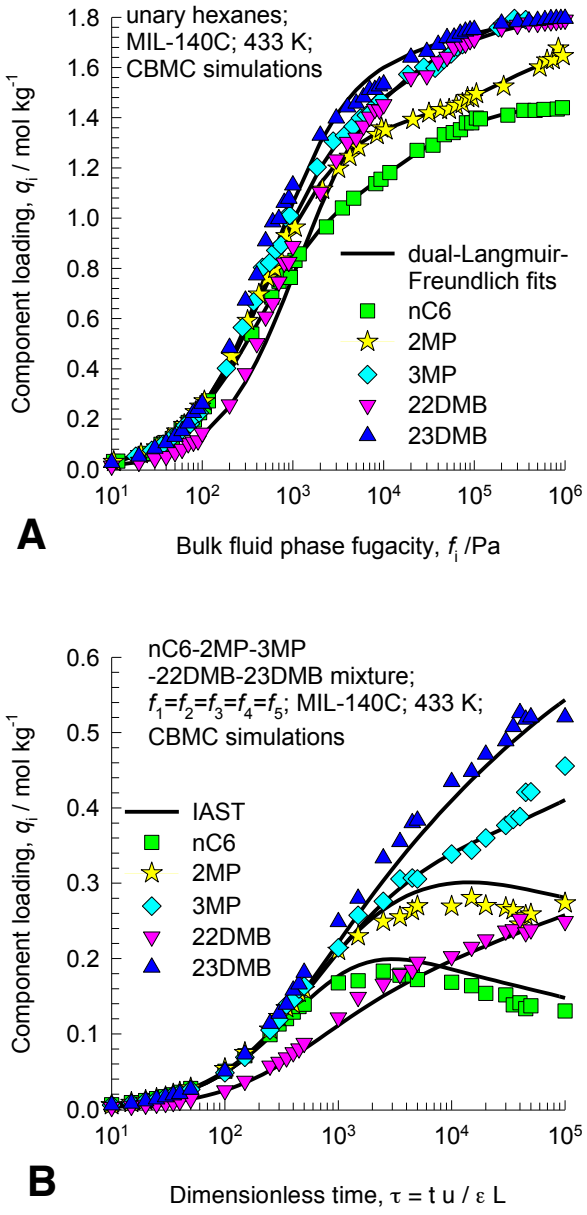

Figure S53. CBMC simulations of (**A**) pure component isotherms of nC6, 2MP, 3MP, 22DMB, 23DMB, and (**B**) equimolar mixtures in MIL-140C at 433 K. The continuous solid lines in (**A**) are the dual-Langmuir-Freundlich fits of the isotherms.The continuous solid lines in (**B**) are the calculations of component loadings using the Ideal Adsorbed Solution Theory.

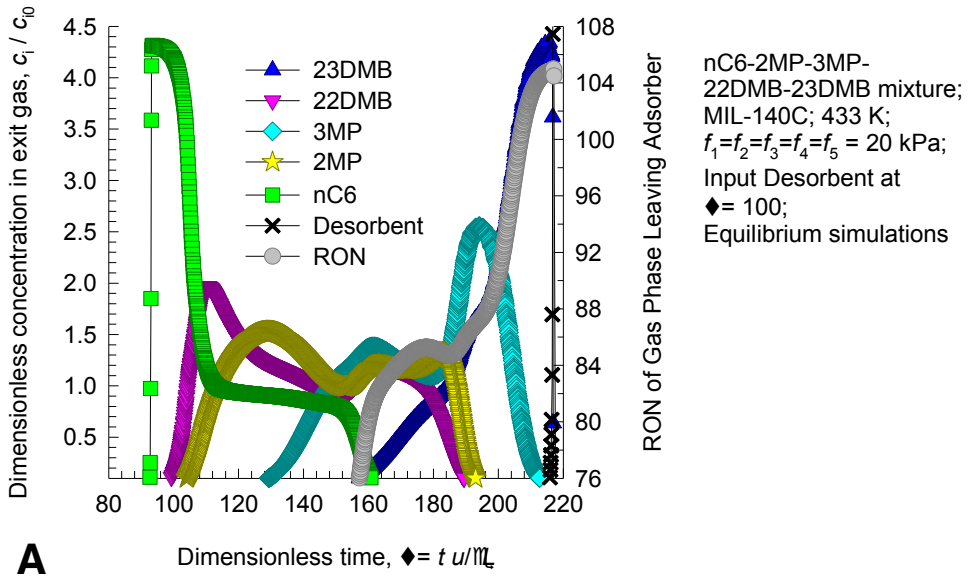

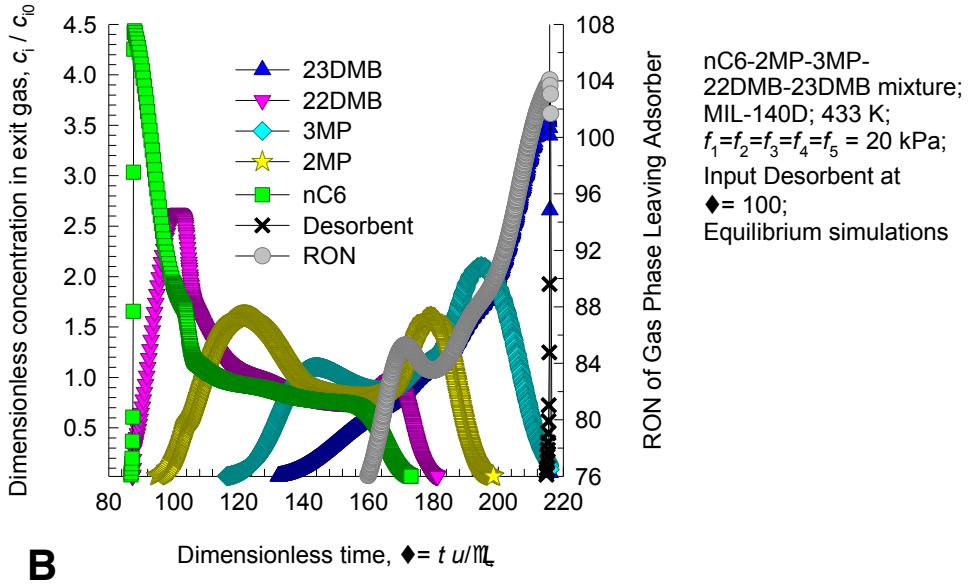

Figure S54. Adsorption/desorption cycles for (**A**) MIL-140C, and (**B**) MIL-140D, operating at a total pressure of 100 kPa and 433 K. The partial pressures of the components in the bulk gas phase at the inlet are $p_1 = p_2 = p_3 = p_4 = p_5 = 20$ kPa. At $\tau = 100$, the desorbent is introduced, and the hexanes feed is stopped. These calculations are based on thermodynamic equilibrium.

Table S1. The alkane-alkane interactions were determined using a previously reported force field. The metal-organic framework structure was considered to be rigid in the simulations. For the atoms in the $Fe_2(BDP)_3$, the generic UFF and DREIDING force fields were used to determine the Lennard-Jones parameters given below. The Lorentz-Berthelot mixing rules were applied for calculating for guest-host interactions.

(pseudo-) atom	σ / Å	εk_B / K
Fe	4.04	27.68
C	3.47	47.86
N	3.26	38.95
H	2.85	7.65

Table S2. Dual-Langmuir-Freundlich parameter fits for $Fe_2(BDP)_3$, as determined from experimental isotherm data obtained at three different temperatures.

	Site A				Site B			
	$q_{A,sat}$ mol kg^{-1}	b_{A0} Pa$^{-\nu_i}$	E_A kJ mol^{-1}	n_A	$q_{B,sat}$ mol kg^{-1}	b_{B0} Pa$^{-\nu_i}$	E_B kJ mol^{-1}	n_B
nC6	0.28	2.74×10^{-26}	111	3	1.17	8.86×10^{-13}	73	1.02
2MP	0.78	2.13×10^{-13}	76	1.1	0.63	5.61×10^{-17}	89	1.36
3MP	0.36	4.62×10^{-13}	76	1.1	1.07	1.34×10^{-16}	89	1.36
22DMB	0.53	1.33×10^{-32}	167	2.9	0.94	1.42×10^{-12}	67	1
23DMB	0.61	9.74×10^{-33}	167	2.9	0.92	1.49×10^{-12}	67	1

Table S3. CBMC pure component isotherms for nC6, 2MP, 3MP, 22DMB, and 23DMB in $Fe_2(BDP)_3$ at 433 K, with pressure in bar and uptake in mmol/g.

nC6		2MP		3MP		23DMB		22DMB	
Pressure	Uptake	Pressure	Uptake	Pressure	mmol/g	Pressure	mmol/g	Pressure	mmol/g
1.17E-06	1.46E-03	1.06E-06	1.96E-05	9.25E-07	1.27E-05	1.00E-05	8.50E-08	3.00E-06	8.50E-08
2.34E-06	2.67E-03	2.11E-06	3.36E-05	1.85E-06	2.68E-05	2.00E-05	1.70E-07	4.00E-06	1.28E-07
3.51E-06	4.03E-03	3.17E-06	5.55E-05	2.77E-06	3.67E-05	3.00E-05	4.68E-07	5.00E-06	2.98E-07
4.68E-06	5.31E-03	4.22E-06	7.64E-05	3.70E-06	5.14E-05	4.00E-05	3.83E-07	6.00E-06	5.10E-07
5.85E-06	6.92E-03	5.28E-06	8.75E-05	4.62E-06	5.99E-05	5.00E-05	1.19E-06	7.00E-06	8.50E-08
7.02E-06	8.97E-03	6.34E-06	1.02E-04	5.55E-06	7.78E-05	6.00E-05	1.36E-06	8.00E-06	2.13E-07
8.19E-06	1.01E-02	7.39E-06	1.28E-04	6.47E-06	9.81E-05	7.00E-05	1.32E-06	9.00E-06	3.83E-07
9.36E-06	1.02E-02	8.45E-06	1.38E-04	7.40E-06	9.86E-05	8.00E-05	1.15E-06	1.00E-05	2.98E-07
1.05E-05	1.14E-02	9.50E-06	1.61E-04	8.32E-06	1.17E-04	9.00E-05	1.87E-06	2.00E-05	6.38E-07
1.17E-05	1.30E-02	1.06E-05	1.77E-04	9.25E-06	1.25E-04	1.00E-04	1.91E-06	3.00E-05	1.11E-06
2.34E-05	2.70E-02	2.11E-05	3.38E-04	1.85E-05	2.58E-04	2.00E-04	3.83E-06	4.00E-05	1.53E-06
3.51E-05	4.20E-02	3.17E-05	4.61E-04	2.77E-05	3.81E-04	3.00E-04	5.10E-06	5.00E-05	1.74E-06
4.68E-05	4.94E-02	4.22E-05	6.16E-04	3.70E-05	5.43E-04	4.00E-04	6.76E-06	6.00E-05	2.25E-06
5.85E-05	7.03E-02	5.28E-05	8.58E-04	4.62E-05	7.25E-04	5.00E-04	8.67E-06	7.00E-05	2.72E-06
7.02E-05	7.51E-02	6.34E-05	1.15E-03	5.55E-05	6.96E-04	6.00E-04	9.56E-06	8.00E-05	2.68E-06
8.19E-05	9.53E-02	7.39E-05	1.21E-03	6.47E-05	8.24E-04	7.00E-04	1.25E-05	9.00E-05	3.70E-06
9.36E-05	1.03E-01	8.45E-05	1.46E-03	7.40E-05	1.01E-03	8.00E-04	1.41E-05	1.00E-04	3.53E-06
1.05E-04	1.17E-01	9.50E-05	1.63E-03	8.32E-05	1.08E-03	9.00E-04	1.69E-05	2.00E-04	7.78E-06
1.17E-04	1.32E-01	1.06E-04	1.80E-03	9.25E-05	1.23E-03	1.00E-03	1.76E-05	3.00E-04	1.11E-05
2.34E-04	2.38E-01	2.11E-04	3.24E-03	1.85E-04	2.59E-03	2.00E-03	3.64E-05	4.00E-04	1.62E-05
3.51E-04	3.38E-01	3.17E-04	4.86E-03	2.77E-04	3.55E-03	3.00E-03	4.74E-05	5.00E-04	1.79E-05
4.68E-04	4.57E-01	4.22E-04	6.52E-03	3.70E-04	5.17E-03	4.00E-03	7.95E-05	6.00E-04	2.40E-05
5.85E-04	5.02E-01	5.28E-04	7.95E-03	4.62E-04	6.61E-03	5.00E-03	7.97E-05	7.00E-04	2.83E-05
7.02E-04	5.82E-01	6.34E-04	1.02E-02	5.55E-04	8.01E-03	6.00E-03	8.69E-05	8.00E-04	2.71E-05
8.19E-04	6.62E-01	7.39E-04	1.29E-02	6.47E-04	9.80E-03	7.00E-03	1.17E-04	9.00E-04	2.99E-05
9.36E-04	7.31E-01	8.45E-04	1.43E-02	7.40E-04	9.37E-03	8.00E-03	1.26E-04	1.00E-03	3.80E-05
1.05E-03	7.23E-01	9.50E-04	1.66E-02	8.32E-04	1.18E-02	9.00E-03	1.53E-04	2.00E-03	7.27E-05
1.17E-03	7.86E-01	1.06E-03	1.80E-02	9.25E-04	1.35E-02	1.00E-02	1.67E-04	3.00E-03	1.12E-04
2.34E-03	1.02E+00	2.11E-03	3.62E-02	1.85E-03	2.59E-02	2.00E-02	3.50E-04	4.00E-03	1.61E-04
3.51E-03	1.13E+00	3.17E-03	4.76E-02	2.77E-03	3.88E-02	3.00E-02	4.73E-04	5.00E-03	1.79E-04
4.68E-03	1.23E+00	4.22E-03	6.48E-02	3.70E-03	5.22E-02	4.00E-02	6.19E-04	6.00E-03	2.04E-04
5.85E-03	1.25E+00	5.28E-03	1.02E-01	4.62E-03	5.96E-02	5.00E-02	8.38E-04	7.00E-03	2.53E-04
7.02E-03	1.28E+00	6.34E-03	9.93E-02	5.55E-03	6.35E-02	6.00E-02	9.07E-04	8.00E-03	2.82E-04
8.19E-03	1.30E+00	7.39E-03	1.24E-01	6.47E-03	9.75E-02	7.00E-02	1.14E-03	9.00E-03	3.49E-04
9.36E-03	1.32E+00	8.45E-03	1.52E-01	7.40E-03	1.14E-01	8.00E-02	1.26E-03	1.00E-02	4.09E-04
1.05E-02	1.35E+00	9.50E-03	1.62E-01	8.32E-03	1.23E-01	9.00E-02	1.42E-03	2.00E-02	7.13E-04
1.17E-02	1.35E+00	1.06E-02	1.67E-01	9.25E-03	1.21E-01	1.00E-01	1.54E-03	3.00E-02	1.08E-03
2.34E-02	1.45E+00	2.11E-02	3.12E-01	1.85E-02	2.22E-01	2.00E-01	3.54E-03	4.00E-02	1.47E-03
3.51E-02	1.53E+00	3.17E-02	4.86E-01	2.77E-02	3.55E-01	3.00E-01	5.13E-03	5.00E-02	1.93E-03
4.68E-02	1.63E+00	4.22E-02	6.41E-01	3.70E-02	4.23E-01	4.00E-01	6.24E-03	6.00E-02	2.15E-03
5.85E-02	1.68E+00	5.28E-02	7.46E-01	4.62E-02	5.33E-01	5.00E-01	9.16E-03	7.00E-02	2.47E-03
7.02E-02	1.68E+00	6.34E-02	8.62E-01	5.55E-02	6.31E-01	6.00E-01	1.05E-02	8.00E-02	2.61E-03
8.19E-02	1.69E+00	7.39E-02	9.38E-01	6.47E-02	7.01E-01	7.00E-01	1.04E-02	9.00E-02	3.62E-03
9.36E-02	1.74E+00	8.45E-02	9.47E-01	7.40E-02	6.55E-01	8.00E-01	1.29E-02	1.00E-01	3.58E-03

1.05E-01	1.74E+00	9.50E-02	1.04E+00	8.32E-02	7.83E-01	9.00E-01	1.59E-02	2.00E-01	7.53E-03
1.17E-01	1.77E+00	1.06E-01	1.08E+00	9.25E-02	8.09E-01	1.00E+00	1.58E-02	3.00E-01	1.24E-02
2.34E-01	1.86E+00	2.11E-01	1.46E+00	1.85E-01	1.11E+00	2.00E+00	3.67E-02	4.00E-01	1.54E-02
3.51E-01	1.91E+00	3.17E-01	1.65E+00	2.77E-01	1.28E+00	3.00E+00	5.88E-02	5.00E-01	1.76E-02
4.68E-01	1.97E+00	4.22E-01	1.75E+00	3.70E-01	1.39E+00	4.00E+00	6.62E-02	6.00E-01	2.31E-02
5.85E-01	1.98E+00	5.28E-01	1.75E+00	4.62E-01	1.42E+00	5.00E+00	1.09E-01	7.00E-01	2.51E-02
7.02E-01	1.99E+00	6.34E-01	1.80E+00	5.55E-01	1.52E+00	6.00E+00	1.24E-01	8.00E-01	3.10E-02
8.19E-01	1.99E+00	7.39E-01	1.85E+00	6.47E-01	1.54E+00	7.00E+00	1.32E-01	9.00E-01	3.50E-02
9.36E-01	1.99E+00	8.45E-01	1.88E+00	7.40E-01	1.64E+00	8.00E+00	1.44E-01	1.00E+00	3.90E-02
1.05E+00	2.00E+00	9.50E-01	1.87E+00	8.32E-01	1.68E+00	9.00E+00	1.71E-01	2.00E+00	7.86E-02
1.17E+00	2.00E+00	1.06E+00	1.90E+00	9.25E-01	1.68E+00	1.00E+01	1.83E-01	3.00E+00	1.24E-01
2.34E+00	2.02E+00	2.11E+00	1.97E+00	1.85E+00	1.83E+00			4.00E+00	1.73E-01
3.51E+00	2.03E+00	3.17E+00	1.99E+00	2.77E+00	1.91E+00			5.00E+00	1.99E-01
4.68E+00	2.03E+00	4.22E+00	2.00E+00	3.70E+00	1.97E+00			6.00E+00	2.18E-01
5.85E+00	2.03E+00	5.28E+00	2.01E+00	4.62E+00	1.98E+00			7.00E+00	3.07E-01
7.02E+00	2.03E+00	6.34E+00	2.01E+00	5.55E+00	2.01E+00			8.00E+00	3.15E-01
8.19E+00	2.03E+00	7.39E+00	2.01E+00	6.47E+00	2.02E+00			9.00E+00	3.95E-01
9.36E+00	2.03E+00	8.45E+00	2.02E+00	7.40E+00	2.03E+00			1.00E+01	3.54E-01
1.05E+01	2.03E+00	9.50E+00	2.02E+00	8.32E+00	2.04E+00				
1.17E+01	2.03E+00	1.06E+01	2.02E+00	9.25E+00	2.02E+00				

Table S4. Dual-Langmuir parameter fits of CBMC simulations of pure component alkane isotherms in $Fe_2(BDP)_3$ (values provided in Table S3); these parameter values are valid for 433 K. Note that the Freundlich exponents n_A, and n_B are unity for all alkanes.

	Site A		Site B	
	$q_{i,A,sat}$ mol/kg	$b_{i,A}$ Pa^{-1}	$q_{i,B,sat}$ mol/kg	$b_{i,B}$ Pa^{-1}
nC5	2.0	1.23×10^{-3}	0.7	6.08×10^{-7}
2MB	2.9	1.75×10^{-5}		
neoP	2.8	6.28×10^{-8}		
nC6	1.6	5.9×10^{-3}	0.4	6.26×10^{-5}
2MP	2.1	8.35×10^{-5}		
3MP	2	6.96×10^{-5}		
22DMB	2.75	1.72×10^{-7}		
23DMB	2.75	7.5×10^{-8}		
nC7	1.38	3.93×10^{-2}		
2MH	1.8	5.77×10^{-4}		
3MH	1.85	1.44×10^{-4}		
22DMP	2	4.94×10^{-7}		
23DMP	2	3.24×10^{-7}		

Table S5. Research Octane Numbers (RON) of C5, C6, and C7 alkanes used for calculations throughout this study.

Alkane		Research Octane Number (RON)
Symbol	Chemical Name	
nC4	n-butane	94
iC4	iso-butane = 2-methyl propane	102
nC5	*n*-pentane	61.7
2MB	2-methyl butane	93.5
neoP	2,2 dimethyl propane	98
nC6	*n*-hexane	30
2MP	2-methyl pentane	74.5
3MP	3-methyl pentane	75.5
22DMB	2,2 dimethyl butane	94
23DMB	2,3 dimethyl butane	105
nC7	*n*-heptane	0
2MH	2-methyl hexane	42.4
3MH	3-methyl hexane	52
22DMP	2,2 dimethyl pentane	92.8
23DMP	2,3 dimethyl pentane	91.1

Table S6. Parameters used throughout the supplementary materials to describe adsorbents that are compared to $Fe_2(BDP)_3$, including pore dimension, uptake capacity (defined in equations 7 and 8) for the six hexane isomers, and the adsorption selectivity (defined in equations 5 and 6).

		d/Å	Uptake (nC6+2MP+3MP)	Uptake (22DMB+23DMB)	Adsorption selectivity, Sads
Normal Hierarchy	Co(BDP)	9.9	0.9555	0.3726	2.5645
	ZIF-77	4.5	0.4046	9.65E-04	419.1038
	MFI	5.5	0.3576	0.1586	2.2543
	MgMOF-74	10.4	0.9469	0.4908	1.9291
	Fe2BDP3	4.9	0.6975	2.88E-04	2418.2638
	ZIF-8	11	0.5797	0.3433	1.6889
	COF-102	8.5	0.982	0.5835	1.683
	COF-103	9	0.9427	0.6295	1.4975
	ZnMOF-74	10.2	0.9787	0.4606	2.1249
	BETA	5.6	0.3699	0.1074	3.4453
	ZnHBDC	8.5	0.7519	0.5777	1.3016
	Zn(bdc)dabco	8.8	0.6813	0.4309	1.581
Reverse or Mixed Hierarchy	UiO-66	6.9	0.1413	0.9048	6.4024
	CFI	6	0.0841	0.5926	7.0448
	ATS	6	0.2341	0.449	1.9182
	MWW		0.1448	0.6791	4.6906
	GME	7.5	0.129	0.4746	3.6781
	MIL-53	6.6	0.3305	0.7621	2.306
	MIL-140C	5.9	0.3282	0.4699	1.4319
	MIL-140D	6.3	0.3283	0.397	1.2093

Table S7. Summary of the 92 RON productivities of the adsorbents discussed in this study, along with the notable limitations of those materials that approach the 92 RON productivity of $Fe_2(BDP)_3$.

Adsorbent	92 RON Productivity Calculated with Diffusion Effects (mol/L)	Notable limitations
$Fe_2(BDP)_3$	0.54	
MWW Zeolite	< 0.52	Severe diffusional limitations
MFI Zeolite	0.51	Can't separate C5/C6/C7 mixtures
Zn(bdc)(dabco)	0.48	Mixed hierarchy
ZIF-8	0.46	ZIF-8 relies on differences in diffusivities of isomers, not on adsorption
Zeolite BETA	0.36	
UiO-66	0.36	
MIL-140C	0.25	
ZnHBDC	0.2	
MIL-140D	0.2	
CFI Zeolite	0.175	
ATS Zeolite	0.17	

Movie S1. Video of the effluent composition of a pulse chromatographic simulation for separation of 5-component hexanes: nC6/2MP/3MP/22DMB/23DMB using $Fe_2(BDP)_3$. These simulations are carried out using pure component isotherm fits of experimentally determined isotherms. Diffusional effects are included with $D_{nC6}/r_c^2 = 0.002$ s^{-1}; $D_{nC6}/D_{2MP} = 5$; $D_{nC6}/D_{3MP} = 5$; $D_{nC6}/D_{22DMB} = 10$; $D_{nC6}/D_{23DMB} = 10$.

References and Notes

1. M. Eddaoudi *et al*., Systematic design of pore size and functionality in isoreticular MOFs and their application in methane storage. *Science* **295**, 469 (2002). doi:10.1126/science.1067208 Medline

2. S. Kitagawa, R. Kitaura, S.-i. Noro, Functional porous coordination polymers. *Angew. Chem. Int. Ed.* **43**, 2334 (2004). doi:10.1002/anie.200300610

3. G. Férey, Hybrid porous solids: Past, present, future. *Chem. Soc. Rev.* **37**, 191 (2008). doi:10.1039/b618320b Medline

4. X. Lin, N. R. Champness, M. Schröder, Hydrogen, methane and carbon dioxide adsorption in metal-organic framework materials. *Top. Curr. Chem.* **293**, 35 (2010). doi:10.1007/128_2009_21 Medline

5. M. P. Suh, H. J. Park, T. K. Prasad, D.-W. Lim, Hydrogen storage in metal-organic frameworks. *Chem. Rev.* **112**, 782 (2012). doi:10.1021/cr200274s Medline

6. D. Liu *et al*., A high connectivity metal–organic framework with exceptional hydrogen and methane uptake capacities. *Chem. Sci.* **3**, 3032 (2012). doi:10.1039/c2sc20601c

7. T. A. Makal, J.-R. Li, W. Lu, H.-C. Zhou, Methane storage in advanced porous materials. *Chem. Soc. Rev.* **41**, 7761 (2012). doi:10.1039/c2cs35251f Medline

8. Z. Bao *et al*., Adsorption of ethane, ethylene, propane, and propylene on a magnesium-based metal-organic framework. *Langmuir* **27**, 13554 (2011). doi:10.1021/la2030473 Medline

9. Y.-S. Bae *et al*., High propene/propane selectivity in isostructural metal-organic frameworks with high densities of open metal sites. *Angew. Chem. Int. Ed.* **51**, 1857 (2012). doi:10.1002/anie.201107534

10. E. D. Bloch *et al*., Hydrocarbon separations in a metal-organic framework with open iron(II) coordination sites. *Science* **335**, 1606 (2012). doi:10.1126/science.1217544 Medline

11. K. Sumida *et al*., Carbon dioxide capture in metal-organic frameworks. *Chem. Rev.* **112**, 724 (2012). doi:10.1021/cr2003272 Medline

12. J.-R. Li, J. Sculley, H.-C. Zhou, Metal-organic frameworks for separations. *Chem. Rev.* **112**, 869 (2012). doi:10.1021/cr200190s Medline

13. A. U. Czaja, N. Trukhan, U. Müller, Industrial applications of metal-organic frameworks. *Chem. Soc. Rev.* **38**, 1284 (2009). doi:10.1039/b804680h Medline

14. D. H. Desty, W. T. Swanton, Gas-liquid chromatography—some selective stationary phases for hydrocarbon separations. *J. Phys. Chem.* **65**, 766 (1961). doi:10.1021/j100823a015

15. R. A. Myers, Ed., *Handbook of Petroleum Refining Processes* (McGraw-Hill, New York, 2004).

16. R. Clavier, Ed., *Wiley Critical Content: Petroleum Technology* (Wiley-Interscience, Hoboken, NJ, 2007).

17. R. V. Jasra, S. G. T. Bhat, Adsorptive bulk separations by zeolite molecular sieves. *Sep. Sci. Technol.* **23**, 945 (1988). doi:10.1080/01496398808058436

18. D. Peralta, G. Chaplais, A. Simon-Masseron, K. Barthelet, G. D. Pirngruber, Separation of C_6 paraffins using zeolitic imidazolate frameworks: Comparison with zeolite 5A. *Ind. Eng. Chem. Res.* **51**, 4692 (2012). doi:10.1021/ie202995g

19. F. Nadim, P. Zack, G. E. Hoag, S. Liu, United States experience with gasoline additives. *Energy Policy* **29**, 1 (2001). doi:10.1016/S0301-4215(00)00099-9

20. R. Krishna, B. Smit, S. Calero, Entropy effects during sorption of alkanes in zeolites. *Chem. Soc. Rev.* **31**, 185 (2002). doi:10.1039/b101267n Medline

21. P. S. Bárcia, J. A. C. Silva, A. E. Rodrigues, Multicomponent sorption of hexane isomers in zeolite BETA. *Am. Inst. Chem. Eng. J.* **53**, 1970 (2007). doi:10.1002/aic.11233

22. A. Silvestre-Albero *et al.*, Is there any microporosity in ordered mesoporous silicas? *Langmuir* **25**, 939 (2009). doi:10.1021/la802692z Medline

23. V. Finsy *et al.*, Low-coverage adsorption properties of the metal-organic framework MIL-47 studied by pulse chromatography and Monte Carlo simulations. *Phys. Chem. Chem. Phys.* **11**, 3515 (2009). doi:10.1039/b822247a Medline

24. P. S. Bárcia *et al.*, Reverse shape selectivity in the adsorption of hexane and xylene isomers in MOF UiO-66. *Microporous Mesoporous Mater.* **139**, 67 (2011). doi:10.1016/j.micromeso.2010.10.019

25. R. F. Lobo, in *Handbook of Zeolite Science and Technology*, S. M. Auerbach, K. A. Carrado, P. K. Dutta, Eds. (Marcel Dekker, New York, 2003), chap. 3.

26. Information on materials and methods is available as supplementary materials on *Science* Online.

27. S. R. Miller *et al.*, A microporous scandium terephthalate, Sc2(O2CC6H4CO2)3, with high thermal stability. *Chem. Commun.* **2005**, 3850 (2005). doi:10.1039/b506677h Medline

28. H. J. Choi, M. Dincă, J. R. Long, Broadly hysteretic H2 adsorption in the microporous metal-organic framework Co(1,4-benzenedipyrazolate). *J. Am. Chem. Soc.* **130**, 7848 (2008). doi:10.1021/ja8024092 Medline

29. J. A. C. Silva, A. E. Rodrigues, Multisite Langmuir model applied to the interpretation of sorption of *n* -paraffins in 5A zeolite. *Ind. Eng. Chem. Res.* **38**, 2434 (1999). doi:10.1021/ie980696t

30. K. Li *et al.*, Unique gas and hydrocarbon adsorption in a highly porous metal-organic framework made of extended aliphatic ligands. *Chem. Commun.* **2008**, 6123 (2008). doi:10.1039/b814498b Medline

31. B. Smit, T. L. M. Maesen, *Nature* **374**, 42 (1995).

32. A. F. P. Ferreira, M. C. Mittelmeijer-Hazeleger, A. Bliek, J. A. Moulijn, Influence of Si/Al ratio on hexane isomers adsorption equilibria. *Microporous Mesoporous Mater.* **111**, 171 (2008). doi:10.1016/j.micromeso.2007.07.043

33. P. S. Bárcia, J. A. C. Silva, A. E. Rodrigues, Separation by fixed-bed adsorption of hexane isomers in zeolite BETA pellets. *Ind. Eng. Chem. Res.* **45**, 4316 (2006). doi:10.1021/ie0513954

34. N. Chang, Z.-Y. Gu, X.-P. Yan, Zeolitic imidazolate framework-8 nanocrystal coated capillary for molecular sieving of branched alkanes from linear alkanes along with high-resolution chromatographic separation of linear alkanes. *J. Am. Chem. Soc.* **132**, 13645 (2010). doi:10.1021/ja1058229 Medline

35. P. S. Bárcia, J. A. C. Silva, A. E. Rodrigues, Adsorption equilibrium and kinetics of branched hexane isomers in pellets of BETA zeolite. *Microporous Mesoporous Mater.* **79**, 145 (2005). doi:10.1016/j.micromeso.2004.10.037

36. T. J. H. Vlugt, R. Krishna, B. Smit, Molecular simulations of adsorption isotherms for linear and branched alkanes and their mixtures in silicalite. *J. Phys. Chem. B* **103**, 1102 (1999). doi:10.1021/jp982736c

37. D. Dubbeldam, R. Krishna, S. Calero, A. Ö. Yazaydin, Computer-assisted screening of ordered crystalline nanoporous adsorbents for separation of alkane isomers. *Angew. Chem. Int. Ed.* **51**, 11867 (2012). doi:10.1002/anie.201205040

38. S. Y. Bhide, S. Yashonath, Anomalous diffusion of linear and branched pentanes within zeolite NaY. *Mol. Phys.* **102**, 1057 (2004). doi:10.1080/00268970410001734305

39. V. Guillerm *et al.*, A series of isoreticular, highly stable, porous zirconium oxide based metal-organic frameworks. *Angew. Chem. Int. Ed.* **51**, 9267 (2012). doi:10.1002/anie.201204806

40. A. A. Coelho, Indexing of powder diffraction patterns by iterative use of singular value decomposition. *J. Appl. Crystallogr.* **36**, 86 (2003). doi:10.1107/S0021889802019878

41. A. A. Coelho, *TOPAS-Academic*, version 4.1 (Coelho Software, Brisbane, Australia, 2007).

42. R. W. Cheary, A. A. Coelho, Axial divergence in a conventional x-ray powder diffractometer. I. Theoretical foundations. *J. Appl. Crystallogr.* **31**, 851 (1998). doi:10.1107/S0021889898006876

43. A. L. Spek, *Acta Crystallogr.* **D65**, 148 (2009).

44. A. I. Kitajgorodskij, *Molecular Crystals and Molecules* (Academic Press, New York, 1973).

45. A. L. Myers, J. M. Prausnitz, Thermodynamics of mixed-gas adsorption. *Am. Inst. Chem. Eng. J.* **11**, 121 (1965). doi:10.1002/aic.690110125

46. Y. He, R. Krishna, B. Chen, Metal–organic frameworks with potential for energy-efficient adsorptive separation of light hydrocarbons. *Energy Environ. Sci.* **5**, 9107 (2012). doi:10.1039/c2ee22858k

47. J. J. Mortensen, L. B. Hansen, K. W. Jacobsen, Real-space grid implementation of the projector augmented wave method. *Phys. Rev. B* **71**, 035109 (2005). doi:10.1103/PhysRevB.71.035109

48. M. Dion, H. Rydberg, E. Schröder, D. C. Langreth, B. I. Lundqvist, van der Waals density functional for general geometries. *Phys. Rev. Lett.* **92**, 246401 (2004). doi:10.1103/PhysRevLett.92.246401 Medline

49. K. Momma, F. Izumi, *VESTA 3* for three-dimensional visualization of crystal, volumetric and morphology data. *J. Appl. Crystallogr.* **44**, 1272 (2011). doi:10.1107/S0021889811038970

50. R. T. Azuah *et al*., DAVE: A comprehensive software suite for the reduction, visualization, and analysis of low energy neutron spectroscopic data. *J. Res. Natl. Inst. Stand. Technol.* **114**, 341 (2009). doi:10.6028/jres.114.025

51. D. Dubbeldam *et al*., United atom force field for alkanes in nanoporous materials. *J. Phys. Chem. B* **108**, 12301 (2004). doi:10.1021/jp0376727

52. H. Wu *et al*., Cu-TDPAT, an *rht* -type dual-functional metal–organic framework offering significant potential for use in H_2 and natural gas purification processes operating at high pressures. *J. Phys. Chem. C* **116**, 16609 (2012). doi:10.1021/jp3046356

53. R. Krishna, J. M. van Baten, Diffusion of hydrocarbon mixtures in MFI zeolite: Influence of intersection blocking. *Chem. Eng. J.* **140**, 614 (2008). doi:10.1016/j.cej.2007.11.026

54. R. Krishna, S. Calero, B. Smit, Investigation of entropy effects during sorption of mixtures of alkanes in MFI zeolite. *Chem. Eng. J.* **88**, 81 (2002). doi:10.1016/S1385-8947(01)00253-4

55. T. Maesen, T. Harris, U.S. Patent 70374222 B2 (2006).

56. T. Maesen, T. Harris, U.S. Patent 7029572 B2 (2006).

57. J. F. M. Denayer *et al*., Rotational entropy driven separation of alkane/isoalkane mixtures in zeolite cages. *Angew. Chem. Int. Ed.* **44**, 400 (2005). doi:10.1002/anie.200454058

58. P. S. Bárcia, F. Zapata, J. A. C. Silva, A. E. Rodrigues, B. Chen, Kinetic separation of hexane isomers by fixed-bed adsorption with a microporous metal-organic framework. *J. Phys. Chem. B* **111**, 6101 (2007). doi:10.1021/jp0721898 Medline

59. Y. Ling *et al*., A zinc(II) metal-organic framework based on triazole and dicarboxylate ligands for selective adsorption of hexane isomers. *Chem. Commun.* **47**, 7197 (2011). doi:10.1039/c1cc12253c Medline

60. R. Krishna, J. M. van Baten, In silico screening of metal-organic frameworks in separation applications. *Phys. Chem. Chem. Phys.* **13**, 10593 (2011). doi:10.1039/c1cp20282k Medline

61. H. W. Dandekar *et al*., U.S. Patent US 5763730 (1998).

62. H. W. Dandekar, G. A. Funk, H. A. Zinnen, U.S. Patent US 6069289 (2000).

63. J. M. van Baten, R. Krishna, Entropy effects in adsorption and diffusion of alkane isomers in mordenite: An investigation using CBMC and MD simulations. *Microporous Mesoporous Mater.* **84**, 179 (2005). doi:10.1016/j.micromeso.2005.05.025

64. R. Krishna, R. Baur, Modelling issues in zeolite based separation processes. *Separ. Purif. Tech.* **33**, 213 (2003). doi:10.1016/S1383-5866(03)00008-X

65. R. Krishna, J. M. van Baten, Screening of zeolite adsorbents for separation of hexane isomers: A molecular simulation study. *Separ. Purif. Tech.* **55**, 246 (2007). doi:10.1016/j.seppur.2006.12.011

66. S. Calero, B. Smit, R. Krishna, Separation of linear, mono-methyl and di-methyl alkanes in the 5–7 carbon atom range by exploiting configurational entropy effects during sorption on silicalite-1. *Phys. Chem. Chem. Phys.* **3**, 4390 (2001). doi:10.1039/b103118j

67. S. Calero, B. Smit, R. Krishna, Configurational entropy effects during sorption of hexane isomers in silicalite. *J. Catal.* **202**, 395 (2001). doi:10.1006/jcat.2001.3293

68. R. Krishna, R. Baur, On the Langmuir–Hinshelwood formulation for zeolite catalysed reactions. *Chem. Eng. Sci.* **60**, 1155 (2005). doi:10.1016/j.ces.2004.09.077

69. R. Baur, R. Krishna, A moving bed reactor concept for alkane isomerization. *Chem. Eng. J.* **109**, 107 (2005). doi:10.1016/j.cej.2005.03.016

70. R. Krishna, Describing the diffusion of guest molecules inside porous structures. *J. Phys. Chem. C* **113**, 19756 (2009). doi:10.1021/jp906879d